



**ADAPTIVE POSITIVE POSITION FEEDBACK CONTROL OF FLEXIBLE
AIRCRAFT STRUCTURES USING PIEZOELECTRIC ACTUATORS**

THESIS

Jared M. Rupp, Captain, USAF

AFIT-ENY-14-M-42

**DEPARTMENT OF THE AIR FORCE
AIR UNIVERSITY**

AIR FORCE INSTITUTE OF TECHNOLOGY

Wright-Patterson Air Force Base, Ohio

DISTRIBUTION STATEMENT A:
APPROVED FOR PUBLIC RELEASE; DISTRIBUTION UNLIMITED

The views expressed in this thesis are those of the author and do not reflect the official policy or position of the United States Air Force, the Department of Defense, or the United States Government.

This material is declared a work of the U.S. Government and is not subject to copyright protection in the United States.

AFIT-ENY-14-M-42

ADAPTIVE POSITIVE POSITION FEEDBACK CONTROL OF FLEXIBLE
AIRCRAFT STRUCTURES USING PIEZOELECTRIC ACTUATORS

THESIS

Presented to the Faculty
Department of Aeronautics and Astronautics
Graduate School of Engineering and Management
Air Force Institute of Technology
Air University
Air Education and Training Command
in Partial Fulfillment of the Requirements for the
Degree of Master of Science in Aeronautical Engineering

Jared M. Rupp, B.S., M.S.

Captain, USAF

March 2014

DISTRIBUTION STATEMENT A:
APPROVED FOR PUBLIC RELEASE; DISTRIBUTION UNLIMITED

ADAPTIVE POSITIVE POSITION FEEDBACK CONTROL OF FLEXIBLE
AIRCRAFT STRUCTURES USING PIEZOELECTRIC ACTUATORS

Jared M. Rupp, B.S., M.S.
Captain, USAF

Approved:

/signed/
Richard G. Cobb, PhD (Chairman)

27 Feb 2014
Date

/signed/
Bradley S. Liebst, PhD (Member)

27 Feb 2014
Date

/signed/
Donald L. Kunz, PhD (Member)

27 Feb 2014
Date

Abstract

Aerodynamic buffet is unsteady airflow imparting forces onto a surface. If a structure is only moderately damped, buffet induced vibrations (BIVs) may cause fatigue of the material, leading to structural failure over time. F-16 ventral fins had the tendency to fail in flight for a number of years, and provided a unique opportunity to conduct control research.

This research, known as Buffet Adaptively Managed Fin (BAMF), sought to improve previous research hardware combined with new adaptive software and test in a realistic environment. BAMF modified a ventral fin by applying electro insulating material to isolate and protect existing macro-fiber composite (MFC) patches and wiring from high speed airflow. An existing custom amplifier and transformer were partially rebuilt, rewired, and restructured into a system that could safely and reliably run continuously. Finally, adaptive software was created to address the issues of system plant changes seen during previous flight tests when airspeed, altitude, and external stores were varied. This adaptive software started with a power spectral density (PSD) generated from MFC sensors on the fin. The highest peaks were assumed to represent the low damped vibration modes of the fin, from which the plant was approximated as a series of second-order systems. A positive position feedback (PPF) controller for each mode was designed, and control signals were sent to the MFC actuators on the fin.

Limited data were collected when the system was run in a wind tunnel behind a custom suspension system with different sized pods to vary the vortex strength and shedding frequencies. While minimal testing was accomplished to optimize gains, the system showed significant PSD peak reductions for the first three modes of the fin up to -14.9, -15.3, and -16.4 decibels (dB), respectively. Additionally, the system proved to be very robust, as it maintained stability and effective control even when both the sensor input and controller output were saturated.

Acknowledgements

This thesis required the dedication of many people beyond myself. AFRL's Experimental Fluid Dynamics Branch provided expert engineering analysis for the test build, fought to get electrical power to run the wind tunnel, and conducted the hot wire anemometry in my absence. I have great appreciation for the efforts of Lawrence Leny, Dr. Robery Guyton, Dr. Tina Reynolds, Jim Hayes, Rick Gillium, Servane Altman, Ray Raber, Rodney Gough, and Captain Tim Cleaver. Additionally, Sean Miller's electrical prowess designed and built the custom amplifier and Jorge Urena Arita spent countless hours with me as we tested and fixed the amplifier through its numerous rebuilds and problems (through no fault of Sean's design). I thank Dr. Donald Kunz for all his work in coordinating the efforts of two schools, AFIT and USAF TPS, to create effective research projects. Finally, I would like to thank Dr. Richard Cobb for his considerable knowledge guiding me through this research and for putting up with my endless questions.

Jared M. Rupp

Table of Contents

| | Page |
|-------------------------------------|------|
| Abstract | iv |
| Acknowledgements | v |
| Table of Contents | vi |
| List of Figures | viii |
| List of Tables | xiii |
| List of Symbols | xiv |
| List of Abbreviations | xv |
| List of Acronyms | xvi |
| I. INTRODUCTION | 1 |
| 1.1 Structural Vibrations | 1 |
| 1.2 Problem | 7 |
| 1.3 Scope | 7 |
| 1.4 Approach/Methodology | 8 |
| 1.5 Limitations | 9 |
| 1.6 Preview | 9 |
| II. LITERATURE REVIEW | 10 |
| 2.1 HAVE PUFF | 10 |
| 2.2 FEM Analysis | 11 |
| 2.3 Active Fin | 12 |
| 2.4 Hyper-Active Fin | 15 |
| 2.5 PPF control | 16 |
| 2.6 Adaptive Control | 18 |
| 2.7 Summary | 18 |
| III. METHODOLOGY | 19 |
| 3.1 System Overview | 19 |

| | Page |
|---|------|
| 3.2 System Design | 19 |
| 3.3 Amplifier and Transformer Box Modifications | 22 |
| 3.4 Ventral Fin Identification | 24 |
| 3.5 Adaptive Control Development | 26 |
| 3.6 Software Development | 32 |
| 3.7 SARL Testing | 36 |
| 3.7.1 Vortex Shedding Strength | 38 |
| 3.7.2 Vortex Shedding Frequency | 39 |
| 3.8 Summary | 41 |
| IV. Results and Analysis | 43 |
| 4.1 Lab Testing | 43 |
| 4.2 SARL Testing | 46 |
| 4.2.1 HW Flow Field Analysis | 46 |
| 4.2.2 Test Conditions | 50 |
| 4.2.3 Vibration Characteristics | 52 |
| 4.2.4 Peak Identification | 58 |
| 4.2.5 Control Selection | 66 |
| 4.2.6 Damping Determination | 68 |
| 4.3 Summary | 76 |
| V. Conclusions | 77 |
| 5.1 Summary | 77 |
| 5.1.1 Hardware | 77 |
| 5.1.2 Software | 78 |
| 5.1.3 Wind Tunnel | 78 |
| 5.2 Recommendations | 78 |
| VI. Appendix A | 80 |
| Bibliography | 102 |
| Vita | 105 |

List of Figures

| Figure | Page |
|--|------|
| 1.1 F-16 LEX vortex formations [25] | 2 |
| 1.2 F/A-18 LEX vortex formations [3] | 2 |
| 1.3 NASA F/A-18 investigating high AOA vortex generation [1] | 3 |
| 1.4 F-15 with vortex formations in front of the tails [29] | 4 |
| 1.5 F-15 tail failure due to fatigue from BIVs [28] | 5 |
| 1.6 F-16 ventral fin failure due to fatigue from BIVs [14] | 5 |
| 1.7 F-16 with LANTIRN system [4] | 6 |
| 2.1 HAVE PUFF DBSJ project [18] | 10 |
| 2.2 Ventral fin damage and FEM strain analysis [17] | 11 |
| 2.3 Active Fin patch placement [4] | 12 |
| 2.4 Active Fin flight test configuration [4] | 13 |
| 2.5 Hyper-Active Fin lab configuration with aft composite strip [22] | 15 |
| 2.6 Block diagram of a system plant and PPF controller | 17 |
| 3.1 BAMF adaptive software overview | 20 |
| 3.2 BAMF system design | 21 |
| 3.3 BAMF fin with accelerometer and MFC built-in sensors | 21 |
| 3.4 Prototype transformer | 23 |
| 3.5 BAMF modified transformer | 23 |
| 3.6 Prototype amplifier | 23 |
| 3.7 BAMF modified amplifier | 23 |
| 3.8 BAMF reconfigured amplifier | 24 |
| 3.9 BAMF fin installed in the SARL wind tunnel | 26 |
| 3.10 Second-order system with various damping ratios (0.2 highlighted) | 27 |

| Figure | Page |
|---|------|
| 3.11 Raw time signal $y(t)$ | 28 |
| 3.12 PSD of signal $y(t)$ | 28 |
| 3.13 BAMF lab impact test FRF | 30 |
| 3.14 Simplified plant of BAMF for PPF control | 30 |
| 3.15 Block diagram for a discrete-time system with state space (SS) representation . | 32 |
| 3.16 Flowchart for the software PSD generation | 33 |
| 3.17 Flowchart for the software discrete PPF generation | 34 |
| 3.18 ControlDesk interface built for BAMF wind tunnel testing | 35 |
| 3.19 SARL wind tunnel diagram [24] | 36 |
| 3.20 LANTIRN pod distance from ventral fin [9] | 37 |
| 3.21 Wide angle view of a pod and BAMF fin installed in the SARL | 38 |
| 3.22 Strouhal number as a function of Reynolds number for various $s=l/d$ ratios [31] | 39 |
| 3.23 SARL test configuration with 12 in pod | 41 |
| 4.1 Comparing the accuracy of BAMF adaptive control to Simulink SS controllers . | 44 |
| 4.2 Testing accuracy and limits of PSD snapshots by varying signal generators . . . | 45 |
| 4.3 HW setup in SARL with pod installed | 47 |
| 4.4 HW VSF at 70 Hz and BPF at 130 Hz | 49 |
| 4.5 Fin sensor VSF at 74 Hz and BPF at 131 Hz | 49 |
| 4.6 Strouhal number as a function of M for each pod | 50 |
| 4.7 BAMF test setup at the SARL | 52 |
| 4.8 Open-loop PSDs of the baseline, 12 in, and 6 in pods at $0.3M$ | 53 |
| 4.9 Fin sensor 1 signal magnitude as a function of M | 54 |
| 4.10 Comparison of accelerometer and fin sensor signal saturated PSDs | 55 |
| 4.11 Mode 1 (~69 Hz) fin sensor PSD peak as a function of M | 56 |
| 4.12 Mode 2 (~88 Hz) fin sensor PSD peak as a function of M | 57 |

| Figure | Page |
|--|------|
| 4.13 Mode 3 (~155 Hz) fin sensor PSD peak as a function of M | 57 |
| 4.14 Mode 4 (~222 Hz) fin sensor PSD peak as a function of M | 58 |
| 4.15 Mode 1 (~69 Hz) fin sensor PSD frequency shift as a function of M | 59 |
| 4.16 Mode 2 (~88 Hz) fin sensor PSD frequency shift as a function of M | 60 |
| 4.17 Mode 3 (~155 Hz) fin sensor PSD frequency shift as a function of M | 60 |
| 4.18 Mode 4 (~222 Hz) fin sensor PSD frequency shift as a function of M | 61 |
| 4.19 Mode 1 (~69 Hz) fin sensor PSD frequency shift as a function of time | 62 |
| 4.20 Open-loop mode 1 PSD snapshot | 63 |
| 4.21 Closed-loop mode 1 PSD snapshot | 63 |
| 4.22 Mode 2 (~88 Hz) fin sensor PSD frequency shift as a function of time | 63 |
| 4.23 Open-loop mode 2 PSD snapshot | 64 |
| 4.24 Closed-loop mode 2 PSD snapshot | 64 |
| 4.25 Mode 3 (~155 Hz) fin sensor PSD frequency shift as a function of time | 64 |
| 4.26 Open-loop mode 3 PSD snapshot | 65 |
| 4.27 Closed-loop mode 3 PSD snapshot | 65 |
| 4.28 Mode 4 (~222 Hz) fin sensor PSD frequency shift as a function of time | 65 |
| 4.29 Open-loop mode 4 PSD snapshot | 66 |
| 4.30 Closed-loop mode 4 PSD snapshot | 66 |
| 4.31 Control signal saturation | 67 |
| 4.32 Comparison of PSDs with control signal saturation | 68 |
| 4.33 Comparison of open and closed-loop PSDs for 12 in pod at $0.3M$ | 69 |
| 4.34 Comparison of open and closed-loop PSDs for 12 in pod at $0.3M$ | 70 |
| 4.35 Comparison of open and closed-loop FRFs for 6 in pod at $0.3M$ | 71 |
| 4.36 Comparison of open and closed-loop PSDs for 6 in pod at $0.3M$ | 72 |
| 4.37 Comparison of open and closed-loop PSDs for 6 in pod at $0.35M$ | 72 |

| Figure | Page |
|--|------|
| 4.38 Mode 1 (~69 Hz) fin sensor PSD peak reduction as a function of M | 74 |
| 4.39 Mode 2 (~88 Hz) fin sensor PSD peak reduction as a function of M | 74 |
| 4.40 Mode 3 (~155 Hz) fin sensor PSD peak reduction as a function of M | 75 |
| 4.41 Mode 4 (~222 Hz) fin sensor PSD peak reduction as a function of M | 76 |
| 6.1 HW PSD with the 12 in pod | 80 |
| 6.2 HW PSD with the 12 in pod | 81 |
| 6.3 HW PSD with the 12 in pod | 81 |
| 6.4 HW PSD with the 12 in pod | 82 |
| 6.5 HW PSD with the 12 in pod | 82 |
| 6.6 HW PSD with the 12 in pod | 83 |
| 6.7 HW PSD with the 12 in pod | 83 |
| 6.8 HW PSD with the 12 in pod | 84 |
| 6.9 HW PSD with the 12 in pod | 84 |
| 6.10 HW PSD with the 6 in pod | 85 |
| 6.11 HW PSD with the 6 in pod | 85 |
| 6.12 HW PSD with the 6 in pod | 86 |
| 6.13 HW PSD with the 6 in pod | 86 |
| 6.14 HW PSD with the 6 in pod | 87 |
| 6.15 HW PSD with the 6 in pod | 87 |
| 6.16 HW PSD with the 6 in pod | 88 |
| 6.17 HW PSD with the 6 in pod | 88 |
| 6.18 HW PSD with the 6 in pod | 89 |
| 6.19 Baseline, 12 in pod, and 6 in pod uncontrolled PSD comparisons at $0.1M$. . . | 90 |
| 6.20 Baseline, 12 in pod, and 6 in pod uncontrolled PSD comparisons at $0.15M$. . . | 90 |
| 6.21 Baseline, 12 in pod, and 6 in pod uncontrolled PSD comparisons at $0.2M$. . . | 91 |

| Figure | Page |
|--|------|
| 6.22 Baseline, 12 in pod, and 6 in pod uncontrolled PSD comparisons at $0.25M$. . . | 91 |
| 6.23 Baseline, 12 in pod, and 6 in pod uncontrolled PSD comparisons at $0.3M$. . . | 92 |
| 6.24 Baseline, 12 in pod, and 6 in pod uncontrolled PSD comparisons at $0.35M$. . . | 92 |
| 6.25 Baseline, 12 in pod, and 6 in pod uncontrolled PSD comparisons at $0.4M$. . . | 93 |
| 6.26 Baseline, 12 in pod, and 6 in pod uncontrolled PSD comparisons at $0.45M$. . . | 93 |
| 6.27 Baseline, 12 in pod, and 6 in pod uncontrolled PSD comparisons at $0.5M$. . . | 94 |
| 6.28 Comparison of uncontrolled and controlled PSDs with the 12 in pod at $0.15M$. | 95 |
| 6.29 Comparison of uncontrolled and controlled PSDs with the 12 in pod at $0.2M$. . | 95 |
| 6.30 Comparison of uncontrolled and controlled PSDs with the 12 in pod at $0.25M$. | 96 |
| 6.31 Comparison of uncontrolled and controlled PSDs with the 12 in pod at $0.3M$. . | 96 |
| 6.32 Comparison of uncontrolled and controlled PSDs with the 12 in pod at $0.35M$. | 97 |
| 6.33 Comparison of uncontrolled and controlled PSDs with the 6 in pod at $0.1M$. . | 97 |
| 6.34 Comparison of uncontrolled and controlled PSDs with the 6 in pod at $0.15M$. . | 98 |
| 6.35 Comparison of uncontrolled and controlled PSDs with the 6 in pod at $0.25M$. . | 98 |
| 6.36 Comparison of uncontrolled and controlled PSDs with the 6 in pod at $0.3M$. . | 99 |
| 6.37 Comparison of uncontrolled and controlled PSDs with the 6 in pod at $0.35M$. . | 99 |
| 6.38 Comparison of uncontrolled and controlled PSDs with the 6 in pod at $0.4M$. . | 100 |
| 6.39 Comparison of uncontrolled and controlled PSDs with the 6 in pod at $0.45M$. . | 100 |
| 6.40 Comparison of uncontrolled and controlled PSDs with the 6 in pod at $0.5M$. . | 101 |

List of Tables

| Table | Page |
|---|------|
| 2.1 Active Fin average modal frequencies (Hz) [4] | 14 |
| 2.2 Active Fin modal frequency shifts [4] | 14 |
| 2.3 Active Fin test points of interest [4] | 14 |
| 3.1 Ventral fin modal frequencies (Hz) | 25 |
| 3.2 Predicted VSF as a function of Mach (Hz) | 40 |
| 4.1 BAMF modified amplifier output | 46 |
| 4.2 SARL BPF (Hz) | 48 |
| 4.3 Strouhal number averages for each pod | 50 |
| 4.4 Predicted verses actual VSF (Hz) | 51 |
| 4.5 Modal frequency shifts during SARL testing (Hz) | 58 |
| 4.6 PSD peak reduction for 12 in pod at $0.3M$ | 70 |
| 4.7 PSD peak reduction for 6 in pod at $0.3M$ | 71 |
| 4.8 PSD peak reduction for 6 in pod at $0.35M$ | 73 |

List of Symbols

| Symbol | Definition |
|--------------|---------------------------|
| l/d | length/diameter |
| f | vortex shedding frequency |
| V_{∞} | velocity |
| d | diameter |
| a | speed of sound |
| T | temperature |
| M | Mach number |
| γ | ratio of specific heats |
| ω_n | natural frequency |
| z | damping ratio |
| g | gain |
| V | Volts |
| t | time (sec) |
| Re | Reynolds number |
| St | Strouhal number |
| F | Fahrenheit |
| A | ampere |
| T_s | discrete sample time |

List of Abbreviations

| Symbol | Definition |
|------------|------------------|
| <i>in</i> | inches |
| <i>ft</i> | feet |
| <i>sec</i> | second |
| <i>rad</i> | radian |
| <i>Hz</i> | Hertz |
| <i>lb</i> | pound |
| <i>sq</i> | square |
| <i>G</i> | force of gravity |

List of Acronyms

| Acronym | Definition |
|---------|--|
| AFRL | Air Force Research Laboratory |
| AFIT | Air Force Institute of Technology |
| WPAFB | Wright-Patterson Air Force Base |
| USAF | United States Air Force |
| TPS | Test Pilot School |
| TMP | Test Management Project |
| TGP | targeting pod |
| PSD | power spectral density |
| PPF | positive position feedback |
| FRF | frequency response function |
| MFC | macro-fiber composite |
| FFT | fast Fourier transform |
| SS | state space |
| RTI | Real-Time Interface |
| SNR | signal to noise ratio |
| BIVs | buffet induced vibrations |
| DOM | drawn over mandrel |
| PA | pressure altitude |
| AOA | angle of attack |
| HW | hot wire |
| NASA | National Aeronautics and Space Administration |
| LANTIRN | Low Altitude Navigation and Targeting Infrared for Night |
| BAMF | Buffet Adaptively Managed Fin |

| Acronym | Definition |
|---------|--|
| MABXII | MicroAutoBox II |
| SARL | Subsonic Aerodynamic Research Laboratory |
| ENI | Test Instrumentation Division |
| AFB | Air Force Base |
| DBSJ | dual bimorph synthetic jet |
| FEM | finite element model |
| LQG | linear quadratic Gaussian |
| SISO | single-input single-output |
| dB | decibels |
| VSF | vortex shedding frequency |
| AC | alternating current |
| MIMO | multi-input multi-output |
| RFP | Request for Proposal |
| DC | direct current |
| HP | horse power |
| RPM | revolutions per minute |
| LCO | limit cycle oscillation |
| BPF | blade pass frequency |
| LEX | leading edge extensions |
| ZOH | zero-order hold |

ADAPTIVE POSITIVE POSITION FEEDBACK CONTROL OF FLEXIBLE AIRCRAFT STRUCTURES USING PIEZOELECTRIC ACTUATORS

I. INTRODUCTION

1.1 Structural Vibrations

The effort to reduce vibrations in structures has been a crucial element of system design and sustainment. This effort lends itself to a wide range of applications, from buildings and bridges to aircraft and spacecraft structures. In aircraft, vibrations can come from a variety of sources, such as the engine, internal systems, or flight control actuations. This research focuses on reducing vibrations due to the interaction of aerodynamic forces with the aircraft structure.

Webster's dictionary defines buffet as "to drive, force, move, or attack by or as if by repeated blows." Aerodynamic buffet is unsteady airflow imparting forces onto a surface, such as a series of vortices caused by a disturbance upstream flowing over a protrusion. When an aircraft structure is subject to buffet, buffet induced vibrations (BIVs) can occur. For structures with low damping, BIVs can cause immediate failure of the structure. If a structure is moderately damped, BIVs may cause fatigue of the material, leading to structural failure over time.

The issue of BIVs has become more important in recent years as aircraft designs seek to combine high top speed with slow speed/high angle of attack (AOA) maneuverability. In general, directional stability decreases as M (Mach) number increases, so large vertical control surfaces are necessary at supersonic speeds. Twin-tail designs are attractive because the stability provided by the tails is double that of a single-tailed aircraft with the same height. The emphasis on maneuverability began to emerge in fourth generation fighter

aircraft designs, influenced by the mostly visual air-to-air engagements of the Vietnam war [11]. The problem with high AOA maneuverability was that the airflow tended to separate at the leading edges of the aircraft, leading to fuselage blanking, where the tail (and specifically the rudder) was ineffective due to the separated flow around it. Loss of directional control is not desirable. The design concept to maintain airflow over the tails at high AOA was to put devices on the leading edges of the aircraft that generated vortices, commonly referred to as strakes or leading edge extensions (LEX) [7]. These would energize the airflow, prevent separation, and allow control to be maintained. The F-16 (Figure 1.1) and F/A-18 (Figure 1.2) clearly show this design, with the vortices starting just below the canopies and extending the length of the fuselage.



Figure 1.1: F-16 LEX vortex formations [3]
[25]



Figure 1.2: F/A-18 LEX vortex formations

Of the fourth generation of fighters, two twin-tailed aircraft known for their maneuverability were the F-15 and the F/A-18. Currently, with the increased emphasis

of radar cross-section reduction, the canted twin-tail has been the only way forward, with the Lockheed F-117, F-22, F-35, Sukhoi T-50, and all fifth generation fighter prototypes sharing this design. However, the vertical stabilizers of twin-tailed aircraft have proven to be more prone to BIVs than those of single-tail aircraft, especially in maneuvering fighter aircraft. The vortices that enhance maneuverability also cause BIVs in the tails [19]. Figure 1.3 is from a National Aeronautics and Space Administration (NASA) investigation into the interaction of vortices generated at high AOA and aircraft structure response. It is worthwhile to view the video at <http://www.dfrc.nasa.gov/Gallery/Movie/F-18HARV/HTML/EM-0013-01.html> and observe the shaking of the tails.



Figure 1.3: NASA F/A-18 investigating high AOA vortex generation [1]

The F/A-18 has had numerous structural fatigue issues with its tails [19]. Lesser known are the problems that the F-15 also encountered. Figure 1.4 shows an F-15 performing a high-G maneuver, demonstrating the vortices that form in front of the tails.



Figure 1.4: F-15 with vortex formations in front of the tails [29]

Within six months of the first F-15A Eagle delivery, cracks were discovered on the tails. This led to four major design changes in 1976, 1980, 1986, and 1993. With each design change, the problematic structure was stiffened, but this led to the forces being transferred to adjoining unmodified structures, resulting in cracking that was not previously an issue in that part of the tail (Figure 1.5). Of the roughly 90-120 Eagles processed annually through the Warner Robbins Air Logistics Center, 80% had tail damage requiring repair or replacement. The repairs led to a cost of approximately \$6 million per year, in addition to reduced fleet readiness [12].



Figure 1.5: F-15 tail failure due to fatigue from BIVs [28]



Figure 1.6: F-16 ventral fin failure due to fatigue from BIVs [14]

The F-16 ventral fin also suffered from serious design flaws for a number of years. The ventral fins had the tendency to fail in flight due to fatigue. After research and

analysis, the cause was determined to be throttle chops in certain flight regimes, where the pilot would suddenly pull the throttle from a high power setting to engine idle, causing highly energetic turbulent air to spill out of the inlet and travel down the fuselage of the aircraft, causing significant vibrations of the fins [21]. Additionally, the Low Altitude Navigation and Targeting Infrared for Night (LANTIRN) system began flight tests in 1983. The LANTIRN system consisted of a navigation pod and targeting pod (TGP), that were mounted on aircraft stations 5R and 5L under the inlet, respectively.

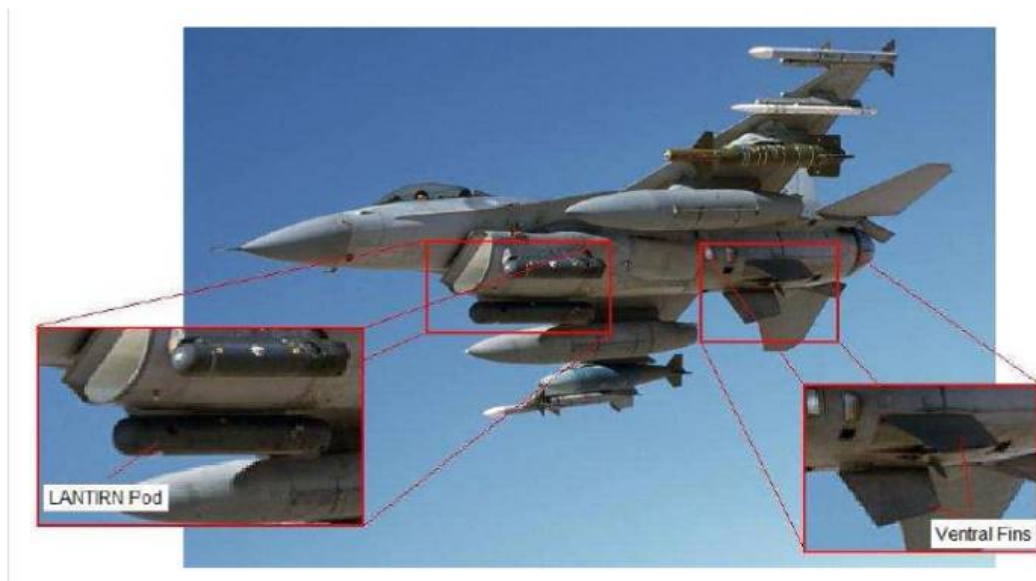


Figure 1.7: F-16 with LANTIRN system [4]

Even after several redesigns, the fin failures continued for a number of years. As fins were redesigned and stiffened, adjoining structures began to fatigue such as the engine access door adjacent to the fin-fuselage mount, which also required a modification. Even after several modifications to the fins, in 1990, 11% of the worldwide fleet of block 30s had fin failures. A 1992 United States Air Force (USAF) report revealed that block 30 fins had an average life of 450 flight hours before needing to be replaced, versus the specified design life of 8,000 flight hours[21]. For blocks 15, 25, and 30, there were 10 different

ventral fin designs that were fielded. One of the key aspects of the failures was the bolts that connected the fin to the fuselage. It was discovered in flight tests that the vibration of the fin would fatigue the bolts and holes in the fin, ultimately leading to increased bending in-flight to the point of failure. Another redesigned fin, with new structure, thicker cross section, and modified bolts and connectors, was introduced in bock 40 aircraft, and proved successful. All previous blocks were also modified with the new fin [21]. The ventral fin susceptibility to BIVs provided a unique opportunity to conduct research on control of BIVs. The fins were small, relatively inexpensive, and did not pose a flight safety risk if failure occurred as many F-16 operational pilots were not aware of the fin failures until wingman visual checks or landing. There were four previous research programs conducted on the F-16 ventral fin investigating BIVs: HAVE PUFF, FEM Analysis, Active Fin, and Hyper-Active Fin. These will be discussed in greater detail in Chapter II.

1.2 Problem

This research sought to investigate adaptive vibration control and damping on full scale aircraft structures. Because of changes in flight conditions and stores configurations, flight tests have shown that BIVs can significantly vary in frequency and magnitude. Adaptive control attempts to combat this by adjusting control parameters as the BIVs change.

1.3 Scope

This research focused on modifying existing hardware from the Hyper-Active Fin project and combining hardware with adaptive control methods to create a robust automatic vibration control system with an end goal of flight test. Buffet Adaptively Managed Fin (BAMF) consisted of the modified Hyper-Active F-16 ventral fin, dSPACE MicroAutoBox II (MABXII) control computer, new adaptive software, modified Hyper-Active signal processor/amplifier, and modified Hyper-Active transformer. After lab testing, the system

was to be put in the Subsonic Aerodynamic Research Laboratory (SARL) wind tunnel at the Air Force Research Laboratory (AFRL) for more realistic testing. After this, it was anticipated that the modified hardware and software would flight test at the USAF Test Pilot School (TPS) as the Test Management Project (TMP) HAVE BAMPF. However, shortly after receiving the Hyper-Active Fin electrical components to modify for flight test, Edwards Air Force Base (AFB) 412th Test Engineering Group, Test Instrumentation Division (ENI) determined that the timeline was too compressed to be able to modify the components to meet flight test safety standards. The system was returned to the Air Force Institute of Technology (AFIT) with some modification work completed and the system was installed in the SARL wind tunnel for data collection. Flight testing was not conducted as part of this effort.

1.4 Approach/Methodology

With standard control theory, controllers are built from a mathematical model of the system plant coupled with desired performance characteristics. It was shown from Active Fin that the plant could change significantly based on the flight conditions, with air density and velocity being the influential variables on the vortices shed from the LANTIRN TGP. This unsteady flow was difficult to model, and it was decided that a more universally valuable approach would be the use of adaptive control. From sensors on the fin, the power spectral density (PSD) would reveal the frequency content of the signal. The largest signals were assumed to represent the low damped vibration modes of the fin, from which a simplified mathematical model of the plant was derived. The plant was approximated as a series of second-order systems. A positive position feedback (PPF) controller for each mode was designed and implemented, with control signals sent to the macro-fiber composite (MFC) actuators on the fin.

1.5 Limitations

Due to the excessive time and expense to bring the BAMF hardware up to flight test safety standards, testing was limited to laboratory testing at AFIT and wind tunnel testing at AFRL. Additionally, a time constrained schedule coupled with numerous equipment anomalies limited laboratory testing and poor weather conditions and electric power limitations due to sequestration limited wind tunnel testing. Overall data collection and controller optimization was limited.

1.6 Preview

Having established the need for aircraft structural vibration control, this research sought to address it with adaptive software coupled with custom hardware. Chapter II contains a literature review of previous related work including flight test projects and control background. The system description, design, and test methodology is covered in Chapter III. Chapter IV contains the results and analysis of the laboratory and wind tunnel testing. The main body is concluded in Chapter V, with an Appendix including additional figures.

II. LITERATURE REVIEW

There were four previous research programs conducted on the F-16 ventral fin investigating BIVs: HAVE PUFF, FEM Analysis, Active Fin, and Hyper-Active Fin. These programs, listed by date of execution, contained a mix of theoretical, laboratory, and flight test data. As higher fidelity testing was accomplished, it proved the need for adaptive control to combat BIVs, as well as more robust and powerful control systems. Adaptive control has taken many forms, but most research has been confined to simulated results without implementation on full-scale aircraft structures.

2.1 HAVE PUFF

HAVE PUFF was a USAF TPS aeroelastic load control project flown on an F-16B to investigate airflow modification to reduce turbulence by using dual bimorph synthetic jet (DBSJ) actuators. The DBSJ actuators were mounted in the aft portion of a LANTIRN TGP replica. The block 15 ventral fin was modified with pressure sensors, accelerometers, and strain gauges to measure the flow and vibrations. The flow was not significantly altered, and no notable fin vibration reductions were noted. It was determined that the airflow around the pod overcame the ability of the DBSJ actuators to alter it [18].



Figure 2.1: HAVE PUFF DBSJ project [18]

2.2 FEM Analysis

Morgenstern conducted more in-depth analysis in conjunction with HAVE PUFF on the ventral fin problem as a basis for future vibration control. After securing a block 40 finite element model (FEM), he modified it to be representative of the known modal frequencies and shapes of a block 15 fin. He noted that his FEM modal predictions closely matched those shown by HAVE PUFF. Conducting a ZAERO analysis, he concluded that the fin was not subjected to flutter within the normal flight envelope of the F-16, but rather material fatigue due to vibrations was indeed the cause of fin failure. With a strain analysis, he recommended the locations and angles to place piezoelectric actuators for vibration control, as well as identifying modes one, two, and four as the principal modes to target [17]. Figure 2.2 shows the actual damage to a ventral fin and the FEM strain analysis results.

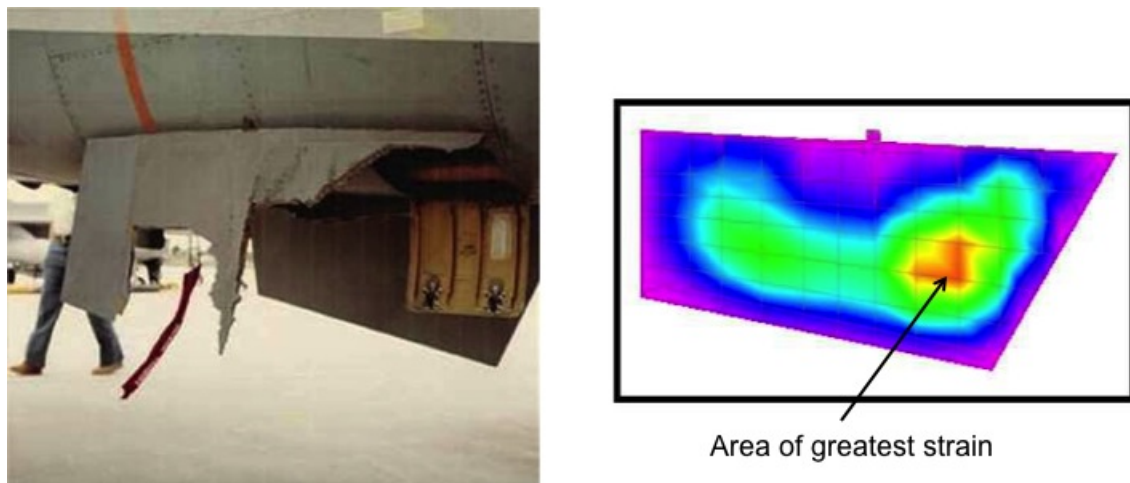


Figure 2.2: Ventral fin damage and FEM strain analysis [17]

Additionally, Morgenstern used the left ventral fin for his analysis; future projects all used the right side fin. The attachment points, especially the forward point, for the left fin are slightly different from the right, and this actually led to the left fin failing in flight more

frequently than the right [21]. The LANTIRN TGP could only be mounted on the 5R chin hard point, so the right fin was selected for future flight test projects.

2.3 Active Fin

Browning conducted lab and flight tests with a modified F-16 ventral fin. He used a scanning laser vibrometer to identify the modes and principal strain directions. He noted significant differences, both in modal frequencies and shapes, from Morgenstern's FEM analysis. After additional analysis, only modes one and two were targeted due to power and patch placement limitations. He attached one layer of MFC patches ($\pm 500V$ limit) on each side of the fin. The patches were arranged in four groups of three (Figure 2.3), with the center patch of each MFC grouping having a built in sensor that gave the advantages of collocated sensors and actuators [4].

Theoretically, collocated sensors and actuators lead to a minimum phase controller, meaning that there are no right half plane zeros of the plant. Therefore, no matter how high the gains, the system would never go unstable [4]. In reality, phase delays due to



Figure 2.3: Active Fin patch placement [4]

electrical components or time delays due to processing can undo the theory of collocated

sensors/controllers, but its properties are still desirable. Even though he developed PPF and linear quadratic Gaussian (LQG) control algorithms, limitations in the actual flight-approved control computer led to only single-input single-output (SISO) PPF control being flown. Figure 2.4 shows the flight test configuration [4]. While notable damping of -11



Figure 2.4: Active Fin flight test configuration [4]

to -12 dB of mode two was seen in the lab and on ground testing, the flight results were disappointing. A maximum of -4 dB of damping was noted, and only under certain limited flight conditions. Flight data were gathered from 5,000-17,000 ft pressure altitude (PA), 0.3-1.05M, and from 1-5Gs. The most vibration was seen in the transonic speeds around 0.95M, at low altitude with 1G. Under nearly all flight conditions, the controller output was discovered to be saturated at the $\pm 425V$ controller limit, meaning that there was insufficient power to control the vibrations seen by the sensor. Additionally, there were significant changes in modal frequency. Even though the Active Fin mount in the lab was built to closely mirror the boundary conditions of the actual aircraft, it was seen that the modal frequencies of the fin in the lab were different than when mounted on the aircraft as seen in Table 2.1 [4]. Table 2.2 reveals that as the aircraft changed altitude and airspeed, the

Table 2.1: Active Fin average modal frequencies (Hz) [4]

| | Mode 1 | Mode 2 | Mode 3 | Mode 4 |
|---------------------------|--------|--------|--------|--------|
| Lab | 78.1 | 100.6 | 168.1 | 231.3 |
| Aircraft Mounted (Ground) | 81 | 96 | 169 | – |
| Aircraft Mounted (Flight) | 80.4 | 94 | 162.5 | 236.4 |

modal frequencies varied even more. This, coupled with inadequate power to the actuators, led to minimal vibration damping [4].

Table 2.2: Active Fin modal frequency shifts [4]

| | Mode 1 | Mode 2 | Mode 3 | Mode 4 |
|-----------|--------|--------|---------|---------|
| Hz | 76-83 | 90-97 | 158-167 | 230-246 |
| Hz Change | 8 | 8 | 10 | 17 |

Dynamic pressure Q , Reynolds number Re , and vortex shedding frequency (VSF) were estimated from a couple of Active Fins flight test points (Table 2.3) to provide a baseline for the environment experienced by the fin. These points represent the lowest altitude and most vibration experienced in a clean (gear and flaps up) configuration [4].

Table 2.3: Active Fin test points of interest [4]

| Altitude | M | Q | Re | Estimated VSF |
|------------------|------|------|-------------------|---------------|
| 5700 ft PA | 0.77 | 738 | 5.5×10^6 | 178 |
| 7400 ft PA | 0.95 | 1031 | 6.5×10^6 | 217 |
| $slugs ft/sec^2$ | | | assumed $St=0.26$ | |

Browning's fin was assembly 16B701A-802. After contacting the USAF Sustainment Center for more information, it was discovered that this part number did not exist in the USAF inventory. It actually correlated to an F-16N used by the US Navy in the 1980s as an aggressor aircraft. The F-16N was a customized F-16, most closely resembling a USAF block 30 [23]. From the assembly numbering scheme, it appears the F-16N used early production ventral fins, possibly from blocks 5-10. Because of the difference in fins, Active Fin was not able to directly correlate to the previous research of HAVE PUFF or Morgenstern's FEM analysis.

2.4 Hyper-Active Fin

To combat the higher than expected vibrations encountered during Active Fin, Ono created Hyper-Active Fin. Because Active Fin's patches were limited to $\pm 500V$, it was decided to upgrade the next project with more powerful MFC patches ($+1500V$, $-500V$ limit). Active Fin's patches were applied with epoxy, so there was no way to remove the patches without damaging the fin. Therefore, a new fin was acquired. Upon acquisition, It was visually apparent that the two fins were different; Active Fin was all metal, whereas Hyper-Active Fin had a vertical composite section in the back (Figure 2.5) [22].

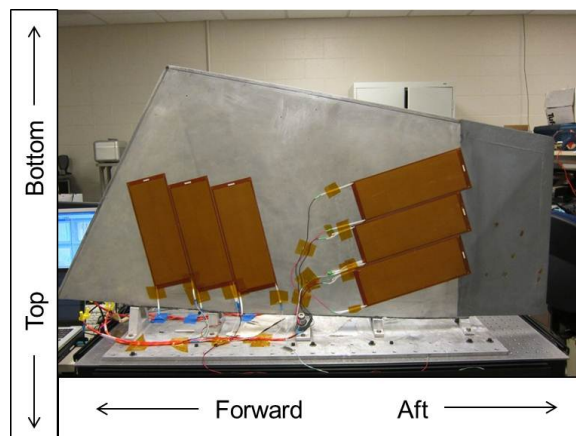


Figure 2.5: Hyper-Active Fin lab configuration with aft composite strip [22]

Ono conducted a modal analysis, and noted that his results closely match Morgenstern's, but differed from Browning's. Ono recomputed the modal strains of the fin, and applied the MFC patches principally aligned with modes two and three in agreement with the vibration data from HAVE PUFF. He applied two layers of MFC patches, effectively doubling the strain they could impart on the fin. He also worked to generate an AFIT custom built class-D switching amplifier, which would boost 115V alternating current (AC) aircraft power to $\pm 700V$, and process sensor and control signals. Using Simulink and running his flight data, Browning had estimated that his system was calling for 1900V maximum. Ono estimated Hyper-Active Fin would only require 690V maximum. Additionally, Ono selected a MABXII control computer. This more advanced computer allowed implementations of SISO and multi-input multi-output (MIMO) PPF, as well as LQG control algorithms. The custom amplifier took significantly more time to build than anticipated, and limited testing was completed on a prototype design. Most of the work was completed with a linear Trek amplifier. Effective vibration damping was achieved in laboratory conditions, with the PPF controllers achieving up to -14 dB reductions, primarily in modes two and three [22]. The fin used was assembly 16B701-804, which was the earliest and least modified ventral fin found on block 10, 15, and 25 aircraft [21].

2.5 PPF control

PPF control was designed in the 1980s as a more robust control method than other existing methods [5]. It is insensitive to spillover, which are effects from uncontrolled or unmodeled modes. Stability is independent of actuator dynamics, but it could become unstable if the stiffness matrix became singular due to high gains [8]. A PPF controller is essentially a special form of a second-order filter targeting a lightly damped mode occurring at a natural frequency (ω_n). The control variables consist of the gain (g), the desired damping ratio (z), and the controller frequency (ω_i) [10]. In a mathematical model form,

the PPF controller views each mode as a second-order system, and ignores the rest of the plant transfer function due to the assumption that only significant plant gains exist at ω_n .

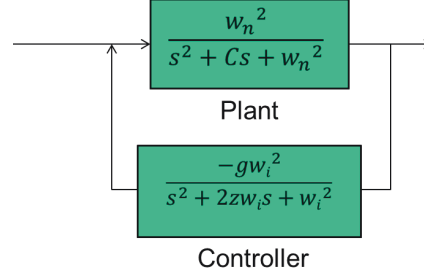


Figure 2.6: Block diagram of a system plant and PPF controller

Gain level plays a role in the stability of the system; like many controllers, too much gain will destabilize the system. Damping ratio is limited based on the amount of control power available, generally a physical limitation of the damping system. For optimal damping of modes, the controller frequency is key. “A little change in optimal parameters setup, especially the change in controller frequency, can strongly degrade the control effort” [10].

PPF control was selected because of desirable characteristics when coupled with MFC patches. Collocated sensors and actuators minimize instabilities. The sensors of the controller only need to measure the modal position/displacement of the structure. A complex system model is not required for design; only knowledge of the natural frequencies are necessary. Fenik et al. makes an important point about multimode PPF controllers. A PPF controller’s cut-off frequency is only slightly higher than the controller frequency, which minimizes the effect of the controller at frequencies higher than the controlled frequency. But the controller does impact all lower frequency modes to some extent [10]. Thus, it is desired to implement controllers from the highest frequency to the lowest.

2.6 Adaptive Control

Flight test data have shown the need for adaptive control of BIVs. Adaptive control methods have been used in aerospace applications of many years, from flight controls [20] to cabin noise attenuation [16]. There are many approaches to adaptive control, such as using gain scheduling via a look-up table, where it was used with a controller aiming to combat varying structural dynamics caused by temperature fluctuations [13]. The vibration control method of identifying the frequency content of the structure to be damped and building PPF controllers was not unique to this research. Mahmoodi et al. also had a similar approach, but their methods were proven on a cantilever beam [15]. BAMF brought together robust hardware and software to damp vibrations on a full-scale aircraft structure subjected to BIVs in a wind tunnel environment. Additionally, the BAMF software coupled with a MABXII control computer resulted in autonomous operation.

2.7 Summary

Investigation into BIVs, especially with the F-16 ventral fin, have revealed the complexity of the problem as the influences on the aircraft structure change with flight conditions. Browning's flight data led Ono to increase the voltage, control authority, and computing power of the general system design. Adaptive control for this research utilized PPF controllers because of the use of MFC patches and difficulty in obtaining complete plant information real-time. The next chapter addresses the methodology for system design, modifications to the hardware, software development, and wind tunnel experimental design.

III. METHODOLOGY

This chapter describes the overall BAMF system design with modifications to existing hardware. Modal analysis was conducted on the modified fin and compared to previous research. Adaptive software was developed and implemented with a control computer for wind tunnel testing. The research for and experimental design of the wind tunnel test is also described.

3.1 System Overview

This research sought to damp the first four modes of the fin. BAMF consisted of an F-16 ventral fin modified with MFC patches, powered by a combination of a custom-built amplifier and transformer designed to operate on AC and direct current (DC) F-16 aircraft power. A dSPACE MABXII control computer, capable of autonomous function, was loaded with adaptive software. The BAMF software took sensor signals from the fin, created a PSD and identified the peaks. The peaks were assumed to equal the low-damped modes of the fin, with the frequencies of the peaks equating to $\omega_n s$. From this characterization, PPF controllers were designed to damp each mode, for a total of four. The PSD was continuously and automatically updated and monitored by the software for any frequency shifts of the peaks. If frequency shifts were detected for any or all peaks, new PPF controllers were autonomously built and implemented. This system was designed to be turned on and operate without any user input.

3.2 System Design

The main characteristics are covered in this section; greater detail of the original hardware can be found in Ono's thesis [22]. The MFC sensor signals from the vibration of the ventral fin were sent to a AFIT custom built Class-D switching amplifier box, where they were conditioned using a Butterworth filter (anti-aliasing), a low pass filter to reduce

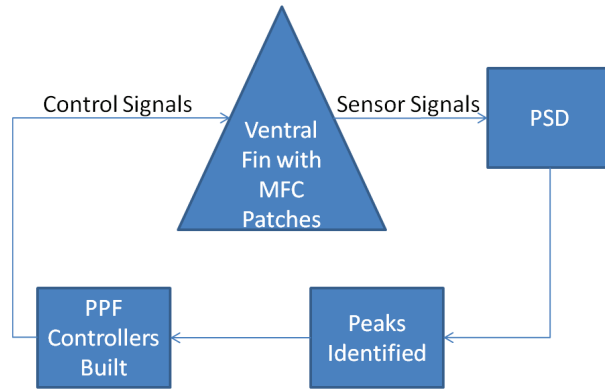


Figure 3.1: BAMF adaptive software overview

noise, and sent to a dSPACE MABXII control computer. The control software was built using Simulink with dSPACE Real-Time Interface (RTI) software, and then uploaded onto the MABXII. The PPF controllers were automatically modified in real time whenever the software detected a frequency shift of a mode. Multiple parameters were monitored on a laptop using dSPACE ControlDesk. ControlDesk also served to record data and to provide the ability to change parameters, such as gains and thresholds, in the Simulink model as it was running on the MABXII. ControlDesk was used for the purposes of testing, but the BAMF control software coupled with the MABXII was fully capable of running effective autonomous control with a simple on/off switch. The control signals were sent from the MABXII to the amplifier box, and combined with the boosted voltage provided by the transformer box. On the F-16, there were two power terminals, 115V 400 Hz AC, and 28V DC. The transformer box was powered by a simulated aircraft power supply to replicate the 115V AC. Most of the components in the amplifier box were powered by a 28V DC supply, except for the control signals boosted by the transformer. The high voltage control signals were sent to the MFC actuators.

The fin also had a PCB Piezotronics accelerometer speed taped to the side that was read independently by a laptop using Data Physics Corporation SignalCalc software to

generate real-time PSDs. Sensor one and two were recorded during testing. The PSD peak outputs of the sensors were nearly identical, so all the data contained in this document is from sensor one's measurement.

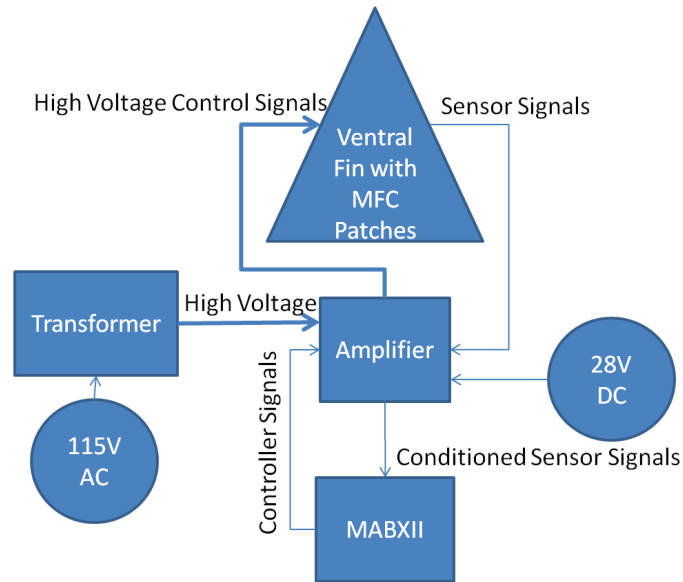


Figure 3.2: BAMF system design

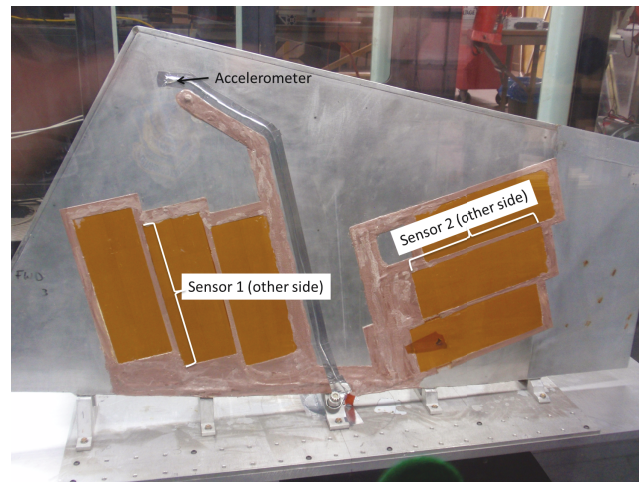


Figure 3.3: BAMF fin with accelerometer and MFC built-in sensors

3.3 Amplifier and Transformer Box Modifications

In the spring of 2012, the fin, amplifier, and transformer were sent to Edwards AFB 412th Test Engineering Group, ENI to be modified to meet flight test standards (generally IPC class III). The components used in the build and the complexity led to time delays due to analysis and Request for Proposal (RFP)s to contractors for electrical engineering work for the modification. After considerable discussion, it was decided that the rebuild to flight test standards and qualifying checkouts, both for safety and reliable function, would be too costly and time consuming for the fall of 2013 flight test timeframe. The fin was modified for wind tunnel test. ENI also partially rebuilt the transformer and amplifier into aluminum boxes both with upgraded wiring and components. In addition to new wiring, connections, component safety enhancements, and configuration, a reset relay was also added to the amplifier box. This would turn on and off the high voltage power from the transformer via control signals from the MABXII.

To facilitate lab work and troubleshooting, the amplifier was reconfigured. A box was constructed of an aluminum frame, with the amplifier components built on a plywood base. As opposed to Figure 3.7, there was minimal stacking of components to increase the distance between them. Clear polycarbonate sides were added to minimize weight while allowing observation and protecting the amplifier from foreign objects. Because of the increased space of the restructured amplifier, some wiring was replaced. After the amplifier was reconfigured (Figure 3.8), it was moved to the SARL.

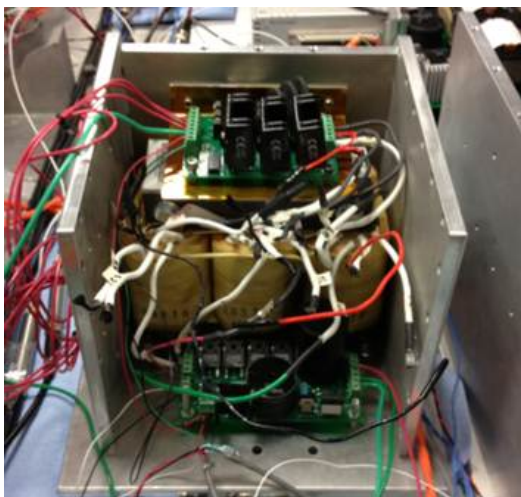


Figure 3.4: Prototype transformer

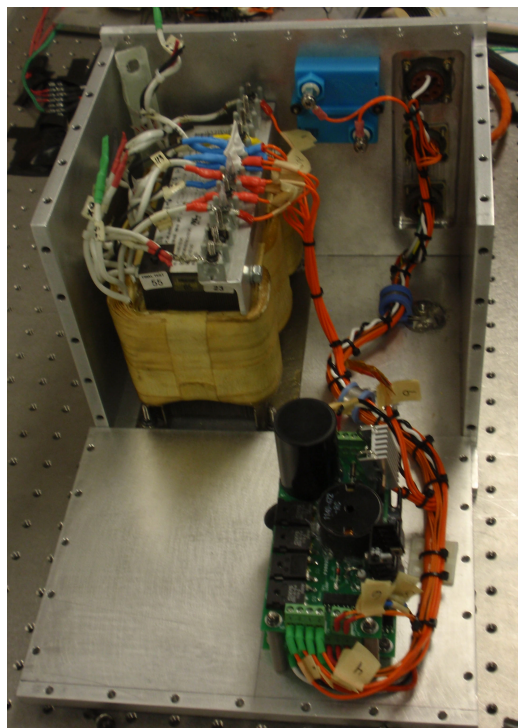


Figure 3.5: BAMF modified transformer

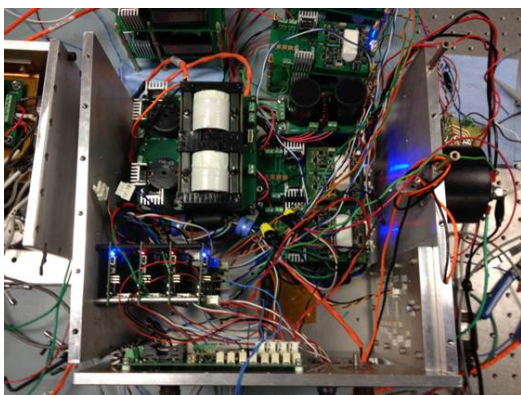


Figure 3.6: Prototype amplifier

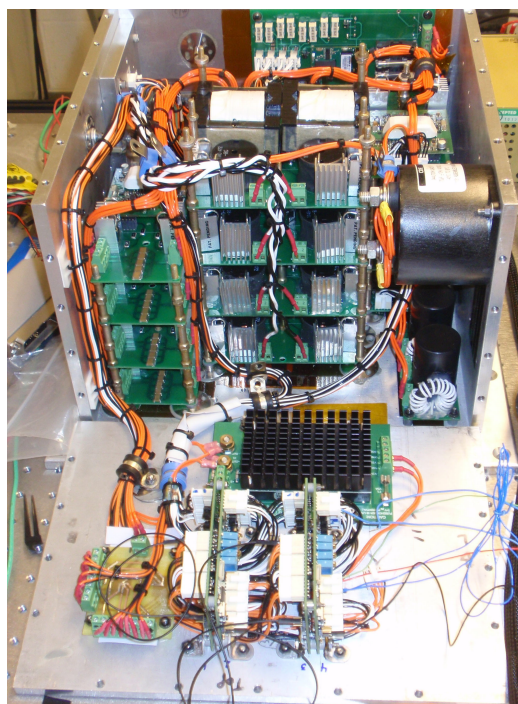


Figure 3.7: BAMF modified amplifier

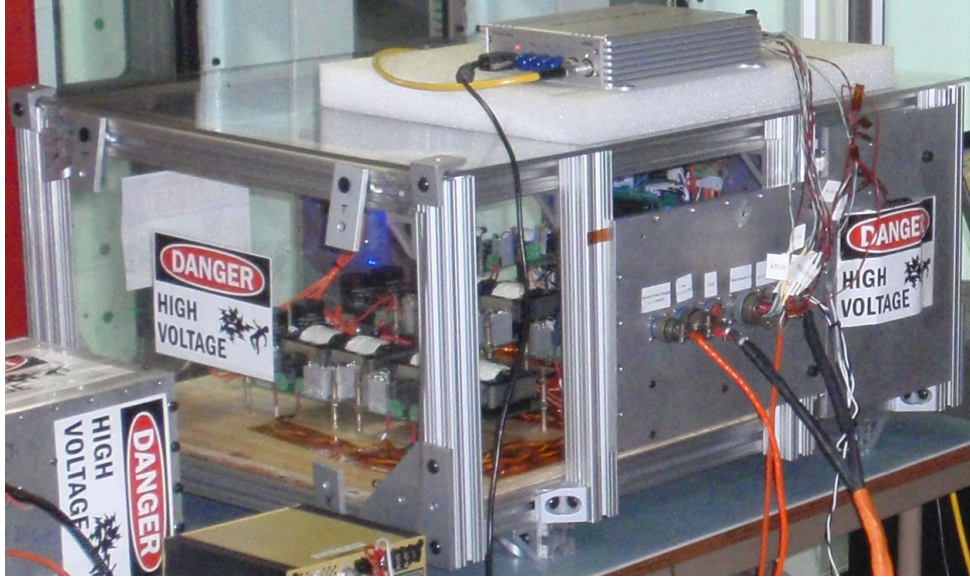


Figure 3.8: BAMF reconfigured amplifier

3.4 Ventral Fin Identification

Ono's original fin identification was on the unmodified ventral fin. He performed another modal analysis after the MFC patches were installed and noted significant shifts in modal frequencies. He attributed these to a possible increased stiffness due to the MFC patches being epoxied to the fin [22]. Under BAMF, the fin was modified further in preparation for wind tunnel and flight testing with the application of electro insulating material around the edges of the MFC patches. This material also protected the wires from high speed airflow and smoothed the contours of the fin modifications in preparation for painting. Modal analysis using an impact hammer was also performed on the latest modification of the fin, with the results in Table 3.1.

Under the Hyper-Active Fin project, the accelerometer was moved around the fin while the impact point for the impulse remained stationary. The BAMF impact hammer testing utilized Maxwell's Reciprocity Theorem, as the accelerometer was stationary and the impulse impact point was moved around the fin. Even with the MFC patches and electro

insulating material installed on the fin, the modal frequencies closely approximated the bare fin, with a maximum shift of about three Hz for mode two. This latest modal analysis result was also independently verified by attaching a signal generator and lab amplifier up to the MFC actuators. While the resonant response of the fin was easy to hear, it was difficult to pinpoint the exact frequency of a mode by ear any more than a few Hz. By placing one hand on the fin, it was easy to feel the modal frequencies to the resolution of the swept signal (one Hz) as the input frequency was changed. This touchy-feely method loosely confirmed the latest modal analysis results.

Table 3.1: Ventral fin modal frequencies (Hz)

| | Mode 1 | Mode 2 | Mode 3 | Mode 4 |
|-------------------------------|--------|--------|--------|--------|
| FEM Analysis | 69.1 | 87.1 | 155.3 | 210.5 |
| Active Fin | 80.4 | 94 | 162.5 | 236.4 |
| Hyper-Active Fin (unmodified) | 65.6 | 88.6 | 152.6 | 206.7 |
| Hyper-Active Fin (with MFC) | 68.4 | 94.2 | 159.1 | 212.59 |
| BAMF Fin | 65.9 | 85.6 | 153.8 | 206.3 |
| BAMF Fin (wind tunnel) | 69 | 88 | 155 | 222 |

Once the fin was installed in the wind tunnel, the modes were verified again. Because of the compressed time frame of the test and the physical separation distance of the fin from the test equipment, the fin was simply struck with an impact hammer while the PSD from the fin accelerometer was measured. Previous testing involved computing frequency response function (FRF)s from measurements of both the hammer and the sensor signals. Since the measured frequency shifts were higher for each mode, it was assumed that the stiffness of the fin was increased, probably by the tightening of bolts between the fin and

attachment points, as well as the points to the base plate, and the base plate to the sub-plate (Figure 3.9).

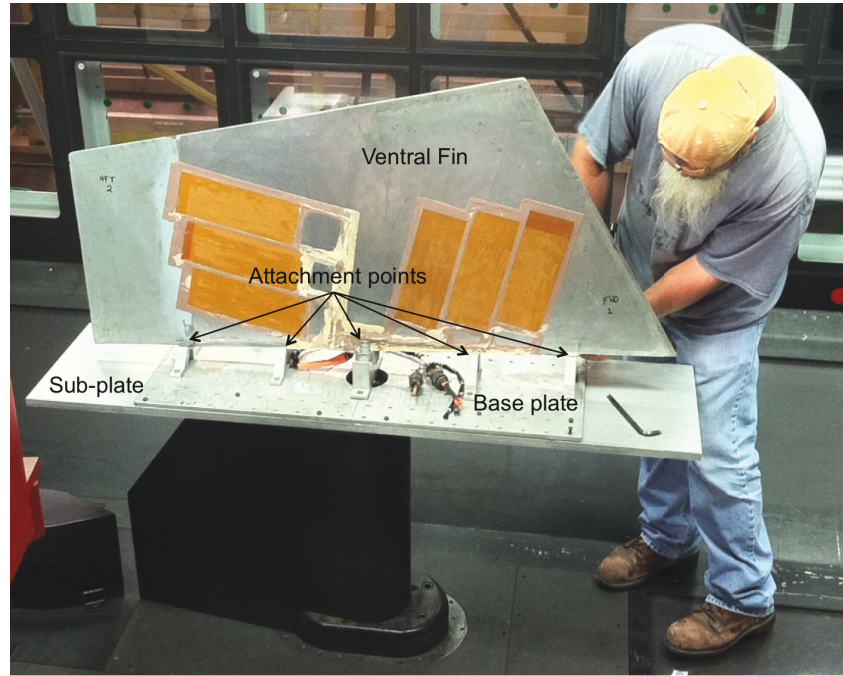


Figure 3.9: BAMF fin installed in the SARL wind tunnel

3.5 Adaptive Control Development

BAMF targeted the first four modes of vibration of the fin. The damping ratio across all four controllers was selected to be 0.2, balancing performance and stability while in line with previous research for comparison purposes [22]. Figure 3.10 plots the effects of damping ratios from a lightly damped second order system at 0.01 to a damped system from 0.1 to 0.5 , where the g_2 function represents a z of 0.2.

The gains for each controller were to be determined experimentally in the lab and constantly analyzed in the wind tunnel to investigate the impacts of them changing. The final parameter, the controller frequency, had to target the modal frequencies of the plant to

be effective. To gather proper modal frequencies, even as they changed, adaptive software was developed.

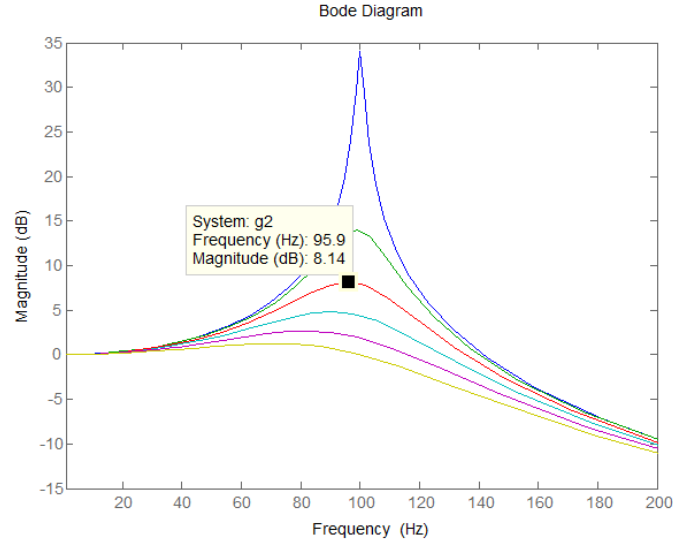


Figure 3.10: Second-order system with various damping ratios (0.2 highlighted)

A time domain signal, such as the signal given by Equation (3.1)

$$y(t) = \sin(\omega_1 t) + \cos(\omega_2 t) + \sin(\omega_3 t) \quad (3.1)$$

where $\omega_1 = 2$ Hz, $\omega_2 = 8$ Hz, and $\omega_3 = 13$ Hz is shown in Figure 3.11. The PSD, assuming the signal can be composed of a variety of sinusoidal signals, converts the time domain signal to the frequency domain, and returns Figure 3.12, revealing the frequencies and their relative strengths in the signal.

The magnitudes of the peaks in the PSD are equal for all three frequencies because their magnitudes in the signal Equation (3.1) are all equal. A structure undergoing resonant vibration has one or more of its modal frequencies excited. With a properly placed sensor, the raw signal from the vibrations converted to a PSD plot will reveal the dominant frequencies of the signal, and thus which modal frequencies were excited.

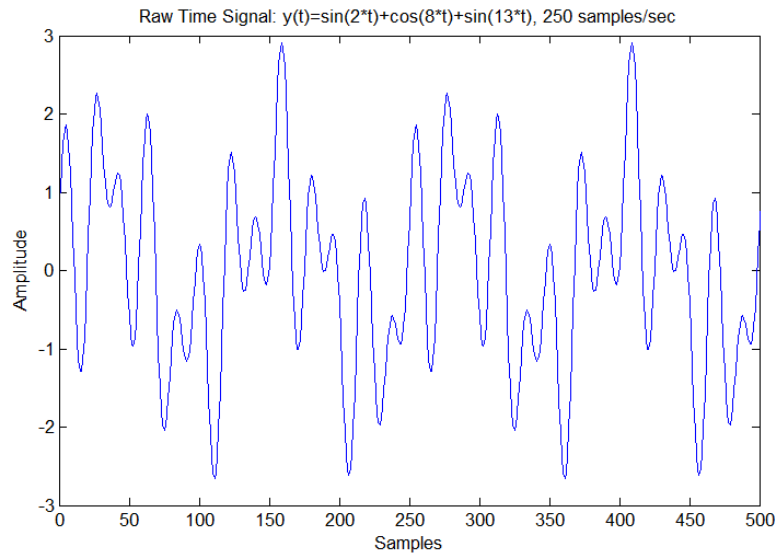


Figure 3.11: Raw time signal $y(t)$

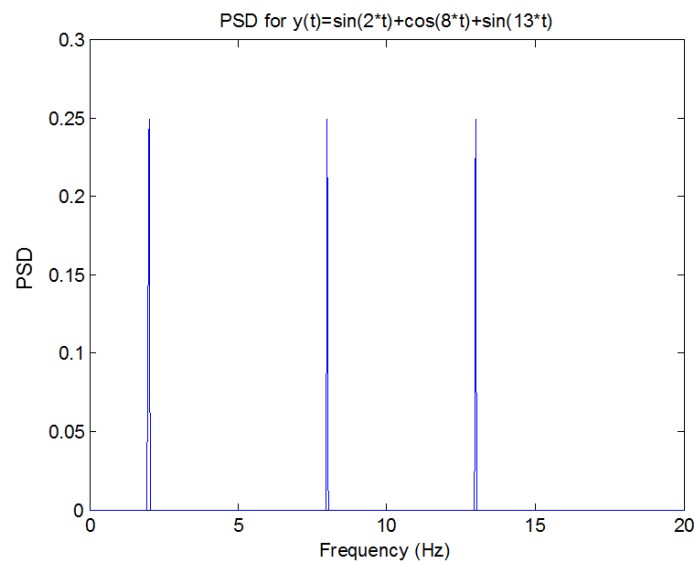


Figure 3.12: PSD of signal $y(t)$

A mathematical model of a system, known as the transfer function, is used to analyze the frequency response of a system to a known sinusoidal input. There is a mathematical

relationship between the frequency content of the passive nature (just listening to the response due to ambient excitations) of a PSD and the input-to-output relationship of a transfer function. Using MATLAB script, the PSD takes time domain data, performs a fast Fourier transform (FFT) into the frequency domain (Equation (3.2)), multiplies by the discrete sample time T_s (Equation (3.3)), then squares the FFT of the output signal, Y (Equation (3.4)).

$$S_y = \text{fft}(Y) \quad (3.2)$$

$$S_{y1} = S_y * T_s \quad (3.3)$$

$$S_{yy} = \text{conj}(S_{y1}) .* (S_{y1}) \quad (3.4)$$

where the S_{yy} vector contains peak magnitude in frequency increments [6].

Transfer functions require an FFT from the time domain (Equation (3.5), Equation (3.6)), square the FFT of the input signal X (Equation (3.7)), then cross multiply the FFT of the input and the output (Equation (3.8)). The cross multiplied FFT input and output is divided by the squared FFT input to create the transfer function (Equation (3.9)).

$$S_y = \text{fft}(Y) \quad (3.5)$$

$$S_x = \text{fft}(X) \quad (3.6)$$

$$S_{xx} = \text{conj}(S_x) .* (S_x) \quad (3.7)$$

$$S_{xy} = \text{conj}(S_x) .* (S_y) \quad (3.8)$$

$$H = S_{xy} ./ S_{xx} \quad (3.9)$$

H is the FRF of the system, which can be broken down into magnitude and phase as a function of frequency [6].

The resonant frequencies can be seen from both the FRFs and the PSDs. Magnitude trends between the PSD and FRF can be compared, as when the frequency response on a mode is damped, the amplitude of the vibration frequency is reduced, and the PSD will

see a lower peak at the damped frequency. However, the absolute magnitudes are not

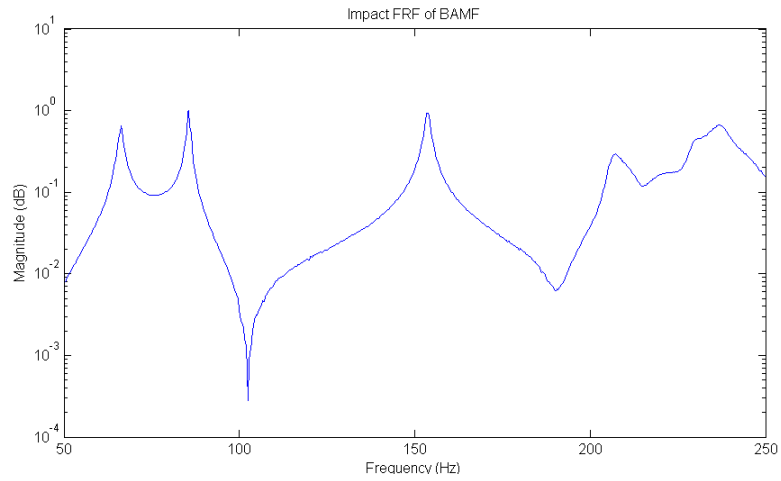


Figure 3.13: BAMF lab impact test FRF

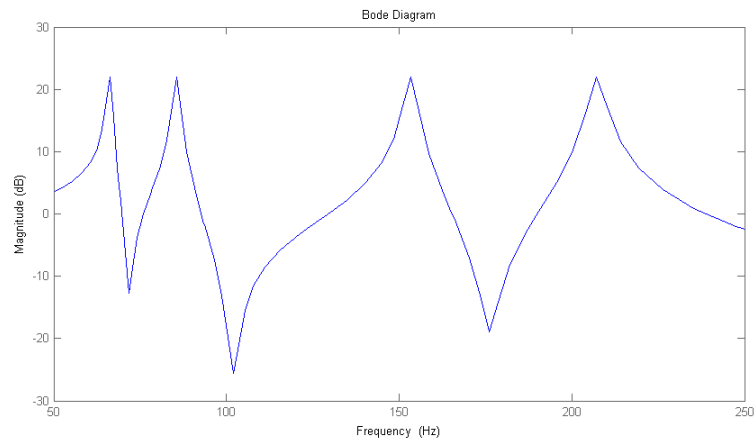


Figure 3.14: Simplified plant of BAMF for PPF control

reliable. An FRF will reveal if a system will resonate with or damp out an input (system response), whereas the PSD just shows frequency magnitudes of the vibrations relative to each other. An important advantage of PPF control was that a complete FRF of the plant

was not necessary for controller implementation. The key control variable that relates to the FRF was the frequency of the modes (ω_n) desired to damp, and this was provided by the PSD. Once the modes were identified, a PPF controller was automatically built to target each mode. The actual fin FRF may look like Figure 3.13, but by just looking at the peaks in the PSD that correspond to peaks/modes in the FRF, a simplified plant FRF can be generated (Figure 3.14) which the PPF controllers are designed to damp.

With this passively obtained knowledge, PPF controllers could be designed real time to control a plant system with shifting natural frequencies and no initial model. The PPF controllers were designed using a continuous SS representation and summed in the frequency domain, but the control signal had to be converted to the discrete time domain for operation. This conversion is well documented in many control theory books, so only the highlights are presented here. Each PPF controller is built into an A submatrix with the roots of the controller (Equation (3.10)). Multiple PPF controllers are combined into the A matrix by Equation (3.11). Starting with the continuous SS A matrix, the discrete SS A matrix (Az) is found by Equation (3.12).

$$A_{subi} = -\omega_i \begin{pmatrix} real & -imag \\ imag & real \end{pmatrix} \quad (3.10)$$

$$A = \begin{pmatrix} A_{sub1} & \cdots & 0 \\ \vdots & \ddots & \vdots \\ 0 & \cdots & A_{subn} \end{pmatrix} \quad (3.11)$$

$$Az = e^{ATs} \quad (3.12)$$

Ts is the time between each sample, or the inverse of the sample rate in samples per second. For the discrete B matrix, the input value at the beginning of the integration period is assumed to be held constant over the period of integration, commonly known as the zero-

order hold (ZOH). The discrete SS B matrix (B_z) is found by the integral

$$B_z = \int_0^{T_s} e^{A\Delta} \delta\Delta B \quad (3.13)$$

Performing the scalar integration yields

$$B_z = A^{-1}(e^{AT_s} - e^0)B \quad (3.14)$$

Converting to matrix math rules and substituting in A_z from Equation (3.12) results in

$$B_z = A^{-1}(A_z - I)B \quad (3.15)$$

The ZOH assumption becomes less and less valid on a dynamic system as the time between samples increases, so high sample rates are desired to minimize conversion errors [6]. The block diagram for a discrete-time system described by a SS representation is shown in Figure 3.15 [30]. The D matrix is grayed out because there were no feedforward terms in this system.

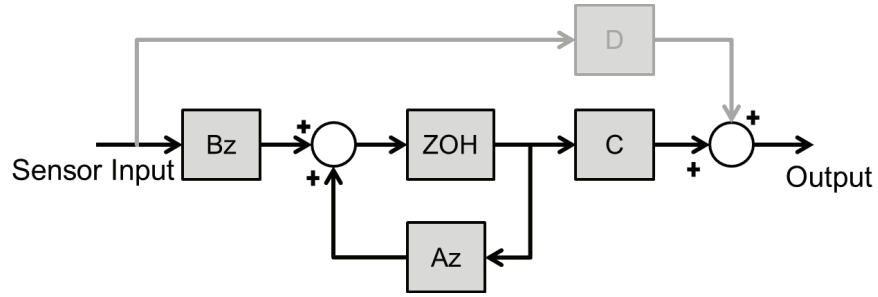


Figure 3.15: Block diagram for a discrete-time system with SS representation

3.6 Software Development

A dSPACE MABXII was used as the interface between the Simulink software and the BAMF hardware. The RTI software that adapted Simulink software to run real time was incompatible with many of the more complex blocks in Simulink; so functions had to

be broken down into many basic blocks. The software took unipolar (zero to one) signals from one front and one rear fin MFC sensor and subtracted 0.5 to convert to a bipolar signal. The sensor signal was sent through a Hanning window and three one-second sets of data were recorded (Figure 3.16). These data blocks were overlapped by 25% to reuse some of

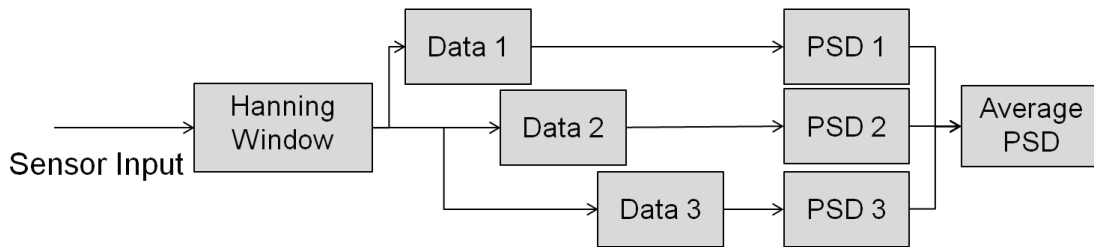


Figure 3.16: Flowchart for the software PSD generation

the incoming signal to shorten collection time while still providing relatively independent samples. Each data block was used to create three separate PSDs, which were then averaged together to increase the signal to noise ratio. If a frequency shift occurred, the first data block PSD would shift after one second, with the signal to noise ratio (SNR) increasing as the two other PSDs detected the shift and were averaged over the next 1.5 seconds. Fast sample rates were desired to collect accurate signal information and the MABXII could handle sample rates up to 40,000 Hz. FFTs used to generate PSDs need sample sizes in powers of two, so a sample rate of 32,768 samples per second was used. PSD frequency resolution is a balance between the number of samples taken and the sample rate. The one second of data collection was the minimum time to collect to achieve a PSD frequency resolution of one Hz. For the sample rate used, the best frequency resolution was one Hz due to the inability of the MABXII to conjugate multiply three-65,536 samples. The averaged PSD was passed on to the controller by a frame conversion, meaning it was sent at the rate it was updated at one Hz.

From the frame conversion averaged PSD, finite bands of frequency centered on the known modes (69, 88, 155, and 222 Hz), referred to as snapshots, were stripped out and the highest peak value was selected within each snapshot. Figure 3.17 shows the flow of the mode one PPF controller, but the other three controllers were built the same way and combined into the Az, Bz, and C matrices. Four snapshots were used to target the first four

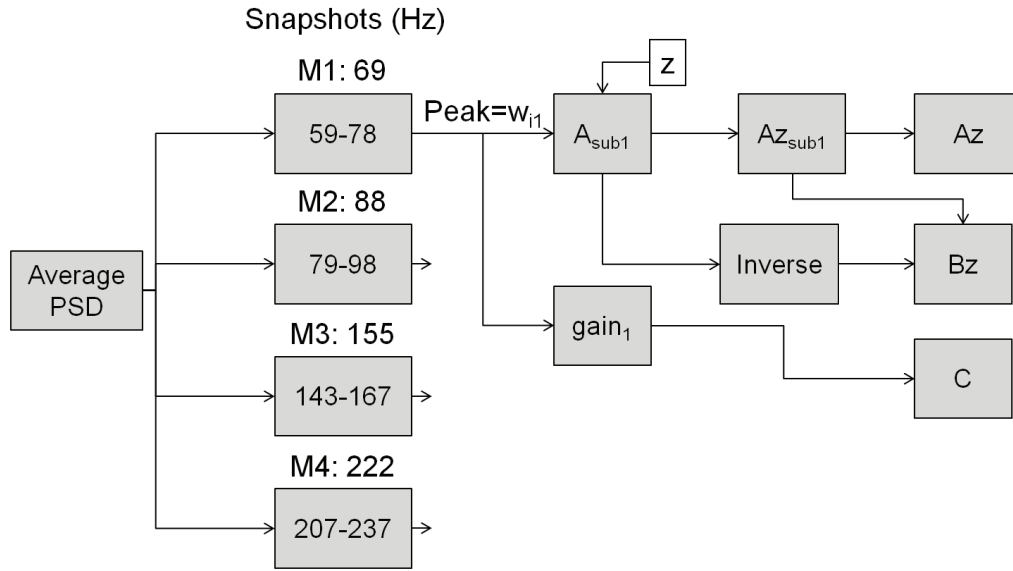


Figure 3.17: Flowchart for the software discrete PPF generation

modes of the fin, with 69 ± 10 , 88 ± 10 , 155 ± 12 , and 222 ± 15 Hz. The first two modes were close together, so the limitations on the snapshots prevented frequency overlaps and ensured that each controller was independent. The maximum peak value within each snapshot was selected, and compared to a threshold value to determine if the signal was strong enough to control. The threshold was an arbitrary number that could be pre-programmed by the user or set real time using ControlDesk. If the peak value was not greater than the threshold, the appropriate C matrix value was set to zero so the controller output was inactivated. If the peak value was greater than the threshold, the controller was implemented. The desired

damping ratio was preprogrammed at 0.2. The gains could be preprogrammed, but these were also adjustable with ControlDesk (Figure 3.18).



Figure 3.18: ControlDesk interface built for BAMF wind tunnel testing

Once the modes were identified from the PSD, PPF controllers were built and SS A, B, and C matrices were built and then incorporated into a discrete SS controller. The control signal was reduced by 0.75, then offset to unipolar by adding 0.625. This resulted in a control signal that was centered between the maximum positive output and maximum negative safe output. Additionally, saturation blocks were used to protect the MFC patches from larger than acceptable control signals.

3.7 SARL Testing

The SARL, operated by the AFRL Air Vehicles Directorate, was the only wind tunnel at Wright-Patterson Air Force Base (WPAFB) with a test section large enough to fit the ventral fin. It was an open circuit wind tunnel, with a test section of 10 feet high and seven

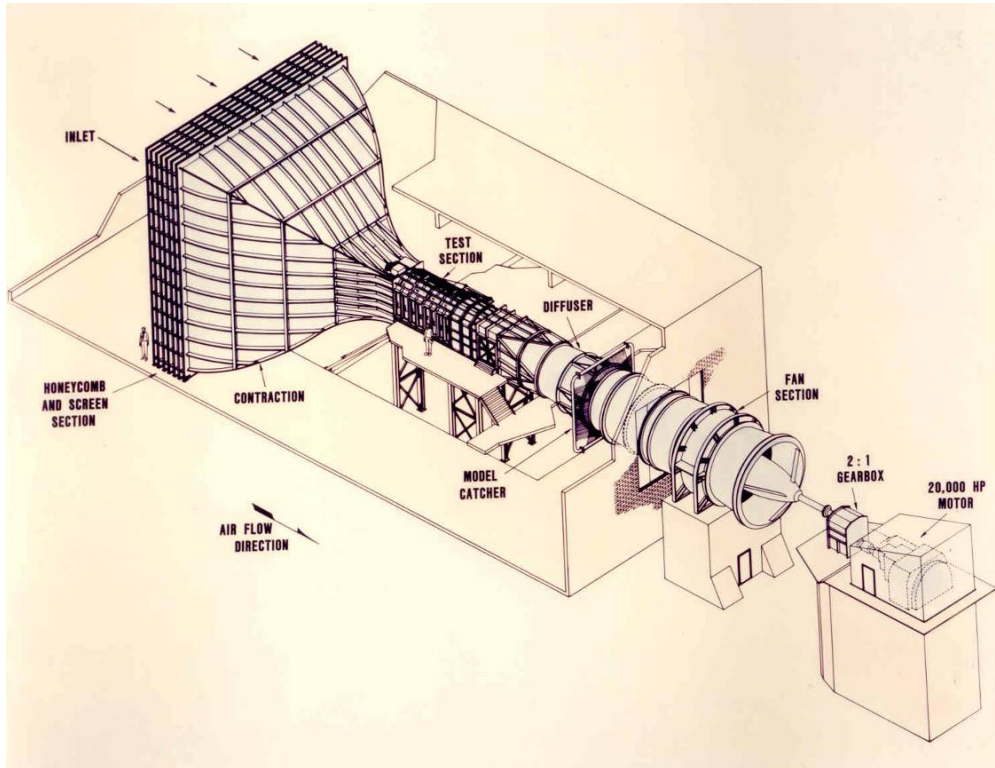


Figure 3.19: SARL wind tunnel diagram [24]

feet wide. The 18 blade fan was powered by a 20,000 horse power (HP) electric motor with a 2:1 gearbox, giving a maximum velocity of $0.5M$ [24]. There was almost no overlap between the maximum velocity that the wind tunnel could produce and the flight conditions experienced by Active Fin, most of which were at $0.7M$ and above. Even at the lower PA of the wind tunnel, the highest dynamic pressure attainable was about half that of the slowest flight test point. The primary goal of wind tunnel testing became to create conditions that would excite the first four modes of the fin similarly to the way the LANTIRN pod would in

flight, rather than try to directly compare data to a flight test environment. The LANTIRN TGP was cylindrical in shape with a rounded nose and flat back. It had a diameter of 15 in and was 98.5 in long [9]. The back of the pod was 130.75 in from the leading edge of the ventral fin, as measured by ENI.

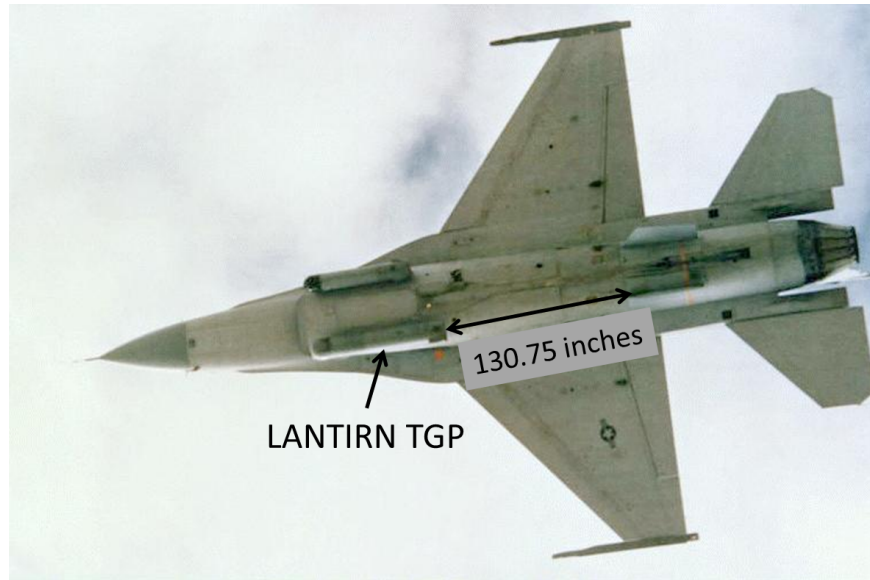


Figure 3.20: LANTIRN pod distance from ventral fin [9]

In the SARL, there was no existing provision to mount a pod in front of the fin. The only holes in the tunnel sidewall at the mouth of the test section were for the installation of a removable test section plug. It was decided that these holes could be tapped to allow for the construction of a pod suspension rig. The suspension rig was designed around aerostrut material, which was support steel tubing that was shaped like a symmetric airfoil to reduce drag and downstream interference. The final design had a center vertical strut that could be moved left or right and the pod moved up and down on it (Figure 3.21) for maximum mounting and research flexibility. The ventral fin was attached to its base plate by a series of mounts which replicated the aircraft attachment points. This base plate was then attached to a 3/4in thick aluminum sub-plate that had been modified to interface between the SARL

pedestal and the BAMF base plate (see Figure 3.9). The leading edge of the fin was only 80 in behind the pod structure, so a replica of a LANTIRN pod would be too large for the test. Additionally, 15 in diameter materials for the construction of the pod were not easily obtainable. Since the distance between the pod and fin had been reduced, it was decided to try to scale the diameter of the pod. The ratio of new distance to full scale distance of 80/130.75 was applied to the diameter, resulting in a desired scaled diameter of 9.2 in.



Figure 3.21: Wide angle view of a pod and BAMF fin installed in the SARL

3.7.1 Vortex Shedding Strength.

Since the test conditions would be at significantly less speed, though at lower density altitudes, than the previous flight test conditions, it was desired to create strong vortices. “The thickness of the boundary layer at the point of separation decreases as the length of the body decreases, and, correspondingly, the larger shear stress in the separated boundary layer causes larger values of the recirculating velocity, thus leading to a more unstable flow” [26]. In essence, as the boundary layer thickness decreases, the shedding vortices strength increases. To generate strong vortices, a shorter pod length was desired. For ease of manufacture, it was decided to use a short 2/1 length to diameter ratio (l/d) for the pods.

3.7.2 Vortex Shedding Frequency.

Larger flow displacements create larger wakes, so larger pod diameters would produce greater turbulence. But it was also desired to be able to target the modes of the fin with the VSFs. The Strouhal number (St) is a function of the VSF (f), pod diameter (d), and velocity (V_∞). Typically, the St is determined experimentally.

$$St = \frac{fd}{V_\infty} \quad (3.16)$$

At low Re , St varies with Re , typically increasing as Re increases [26]. However, high Re would be obtained due to airflow up to $0.5M$ and the full scale nature of the pods. Sevilla et al. [27] determined that St became constant for $Re > 6 \times 10^3$, although their data was limited to $Re = 11 \times 10^3$. Weickgenannt et al. [31] gathered experimental data with an

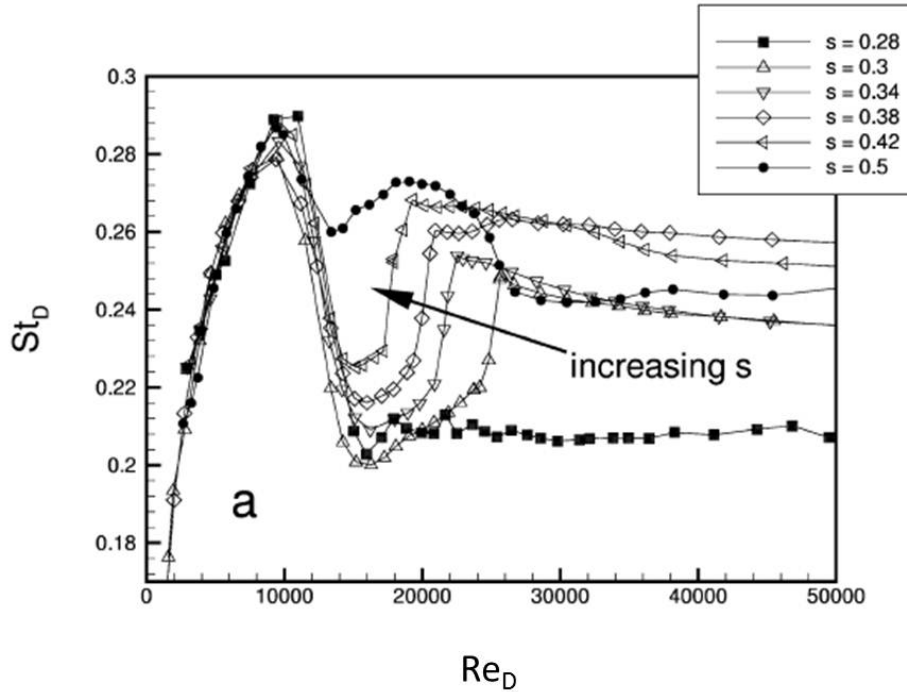


Figure 3.22: Strouhal number as a function of Reynolds number for various $s=l/d$ ratios [31]

axisymmetric round nosed body up to $Re = 5 \times 10^4$, which revealed two key characteristics. Their results showed that St remained constant at high $Re > 2.5 \times 10^4$, which was after the flow had transitioned from laminar to turbulent, and provided an estimated St for test predictions. Figure 3.22 from their article is shown, where s is the l/d .

Figure 3.22 shows that from l/d s of 0.3-0.5, the St was between 0.24 and 0.26 with no trend for increasing l/d . The wind tunnel pods had an l/d of 2, so a St of 0.25 was used for test predictions. With a constant St , the VSF depended solely on pod diameter and airflow velocity. After further material availability evaluations, it was then decided to make four pods of diameters 12, 10, 8, and 6 in to provide a variety of vortex shedding strengths and frequencies. The rounded noses of the pods were created by cutting hollow steel spheres in half and had a aerostrut clamp attached to the inside. The pod body was thin walled drawn over mandrel (DOM) tubing that was attached by screws to the nose. The back of the DOM tubing had a circular plate fitted. This configuration allowed pods to be moved or swapped out in about 15 minutes. Because the actual timeframe for the wind tunnel was unknown, standard atmospheric conditions were assumed at 1000 ft PA [2]. Table 3.2 shows the resulting pre-calculations. Velocity was calculated by Equation (3.17)

Table 3.2: Predicted VSF as a function of Mach (Hz)

| Mach | V_∞ (ft/sec) | 12 in pod VSF | 10 in pod VSF | 8 in pod VSF | 6 in pod VSF |
|------|---------------------|---------------|---------------|--------------|--------------|
| 0.1 | 111 | 28 | 33 | 42 | 56 |
| 0.2 | 223 | 56 | 67 | 83 | 111 |
| 0.3 | 334 | 83 | 100 | 125 | 167 |
| 0.4 | 445 | 111 | 134 | 167 | 223 |
| 0.5 | 556 | 139 | 167 | 209 | 278 |

and Equation (3.18)

$$V_{\infty} = Ma \quad (3.17)$$

$$a = \sqrt{\gamma RT} \quad (3.18)$$

where γ is the ratio of specific heats (1.4 for air) and R is the specific gas constant for air, and T is absolute temperature in degrees R . The four pod system would allow modes to be targeted at close to the maximum M number the tunnel could generate. The expected Re ranged from 3.45×10^5 ($0.1M$ for 6 in) to 3.45×10^6 ($0.5M$ for 12 in). Figure 3.23 shows the tunnel configuration of BAMF with the 12 in pod.

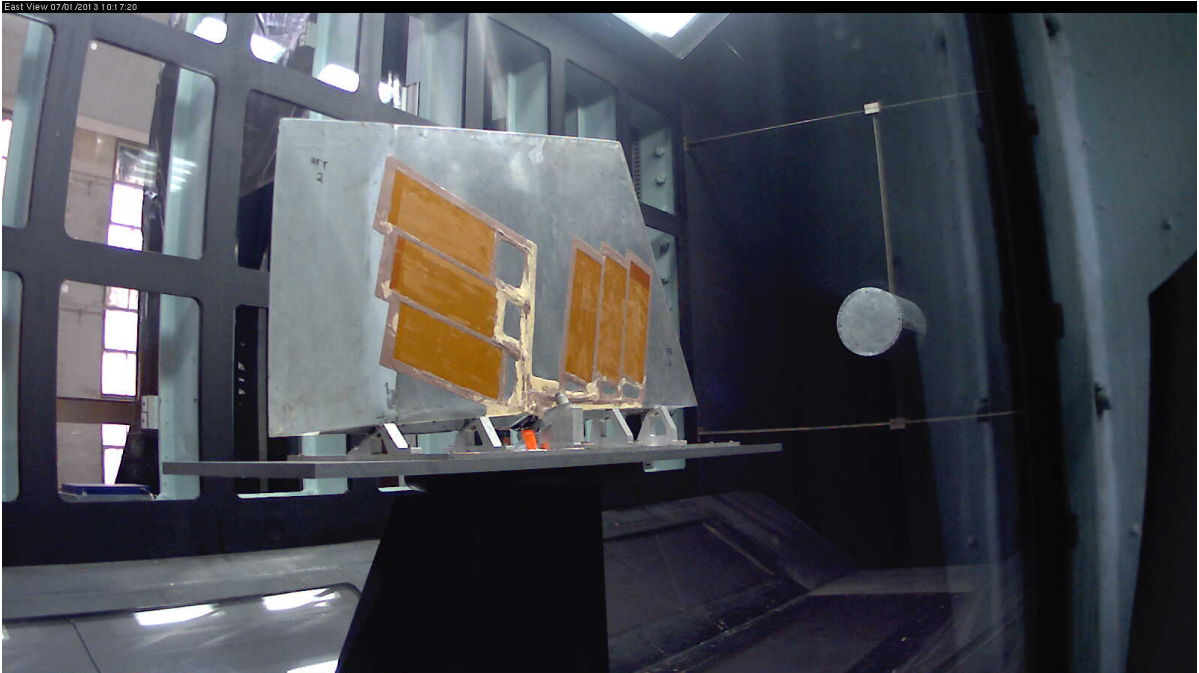


Figure 3.23: SARL test configuration with 12 in pod

3.8 Summary

Modal analysis showed how boundary conditions could significantly affect the modes of the fin, again revealing the need for adaptive control. New adaptive software was

developed and coupled with hardware that was modified into a reliable and mobile system. The pod system and suspension was designed and built in preparation for the wind tunnel test. The next chapter contains the results and analysis of both laboratory and wind tunnel testing.

IV. Results and Analysis

There was minimal laboratory testing completed on the complete system. Each component was tested individually, but the wind tunnel became available at the same time the system became fully operational, so the complete system checkout occurred in conjunction with the wind tunnel testing.

4.1 Lab Testing

Because the SS matrices, specifically the A_z , B_z and C matrices, were continuously being updated as the plant changed, the SS representation had to be constructed with matrix multiplication blocks with rate transitions so that the controller output was constant until the matrices were updated with new controllers. The initial test of the BAMF adaptive software was run in Simulink (Figure 4.1) comparing it with existing control blocks for an eight second simulation. Input signal 1 contained four software signal generators to simulate the first four modes of the fin. A Simulink SS multimode PPF controller was pre-programmed for this first input signal. A second input signal was designed similarly to the first, except that all four frequencies were shifted by five Hz. Another Simulink SS controller was pre-programmed for these new frequencies. A switch was placed to only allow the first signal to the first SS controller for four seconds, and then this signal was cut off and the second signal was let through to the second SS controller for the next four seconds. The control output from both controllers was recorded. At the same time, the BAMF adaptive software, not pre-programmed with any of these signals, was connected so that it would have a continuous signal from the inputs for the full eight second simulation time. Its output was also recorded and compared with the pre-programmed SS controller outputs. It was shown that the BAMF software identified the frequency shift, designed new PPF controllers, and successfully implemented the control signal after two seconds. One

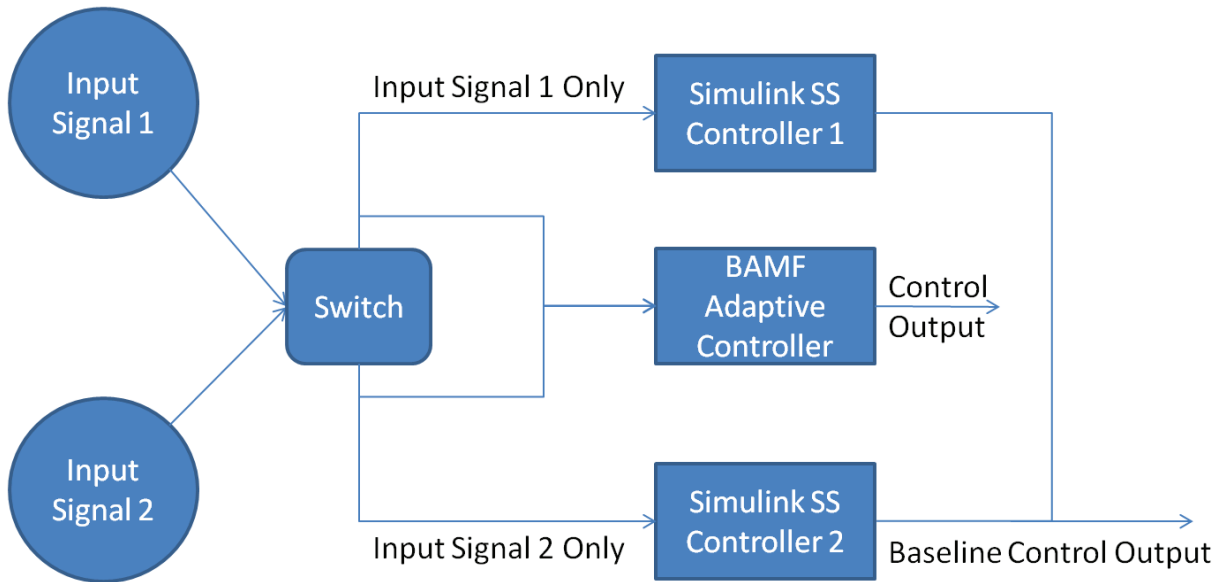


Figure 4.1: Comparing the accuracy of BAMF adaptive control to Simulink SS controllers

second of this was due to the PSD buffering raw data to generate frequency content. The additional second delay was caused by the controllers operating at the same rate as the PSD due to the frame conversion. It may be possible to move the rate transition blocks from after the controller design to just after the PSD, but the best speed is limited by the time the PSD takes to collect data. Once the BAMF controllers were implemented, the signal had 99.998% agreement with the Simulink SS blocks.

Additionally, four signal generators were input into the software through a dSPACE input/output board with the RTI software interface and frequency varied. The BAMF software followed frequency changes closely, proving the connections between the software and hardware, that the BAMF software would properly identify the frequencies of physical signals, and that the snapshots properly constrained the controller frequencies to prevent controller duplication. Figure 4.2 is a screenshot from a video showing the BAMF software adapting. The signal generators are on the right, and the three columns on the

screen with four snapshots rows are PSD peak magnitudes, PSD primary frequency (Hz), and control output targeted frequency (rad/sec).

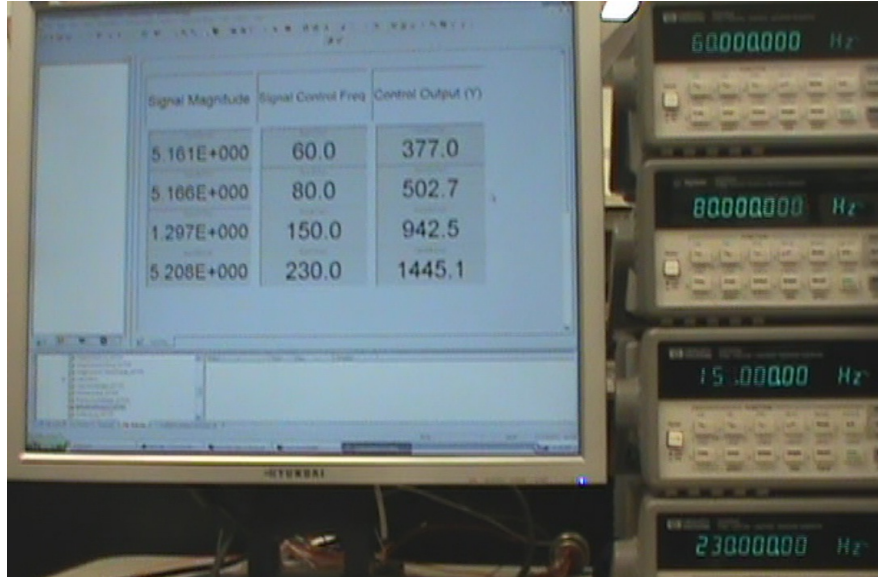


Figure 4.2: Testing accuracy and limits of PSD snapshots by varying signal generators

Due to multiple schedule conflictions and hardware delays, there was almost no lab testing done with the complete system operational. As part of functional checks, it was necessary to verify the amplifier output channels. There were four channels, one for each group of MFC patches. Each channel had a left and right side to provide negative and positive peak-to-peak voltage, respectively. The transformer was connected to the amplifier, and a signal generator provided a unipolar signal to simulate control signals from the MABXII. An oscilloscope was connected to each side to measure the high voltage outputs given each input signal. Table 4.1 lists the outputs.

The design called for up to +1000V, although for F-16 system power limitations, +700V was considered to be the maximum practical [22]. Additionally, the MFC patches were limited to -500V. From the data in Table 4.1, the positive side was lacking voltage, while the negative side exceeded the -500V patch limit. This limit was enforced in the

Table 4.1: BAMF modified amplifier output

| Channel | Max Voltage |
|---------|-------------|
| 1L | -703 |
| 1R | +570 |
| 2L | -706 |
| 2R | +590 |
| 3L | -709 |
| 3R | +557 |
| 4L | -728 |
| 4R | +563 |

software. It may be worthwhile to swap the sides of each channel for more optimal voltage output. The actual control authority was reduced by approximately 19% from the designed because of the average +570V capability of the amplifier.

4.2 SARL Testing

The overall test objective was to observe the characteristics of the ventral fin when subjected to realistic aerodynamic loads, investigate the effects of varying VSFs and strengths, and determine the damping effectiveness of the both the hardware and the software of the BAMF system.

4.2.1 HW Flow Field Analysis.

AFRL conducted hot wire (HW) experiments to gain high fidelity data on the vortices shed by all four pods (Figure 4.3). Due to scheduling constraints, the HW experiments were not conducted until about two weeks after the BAMF tests. On the runs above $0.2M$, regardless of pod diameter, strong frequency content was detected that did not correlate to any known VSF. Based on tunnel engineers visual observations, it was concluded that this

may have been caused by the HW apparatus itself vibrating in the flow field. When the

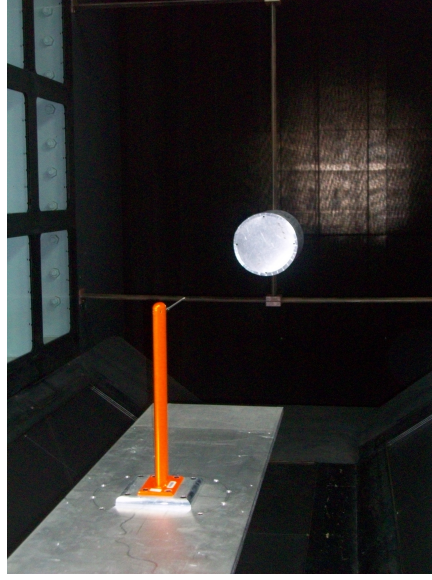


Figure 4.3: HW setup in SARL with pod installed

HW data was compared to the fin accelerometer and fin sensor, both fin sensors also picked up the same frequencies at the same M numbers, independent of which pod was installed. It was determined that the frequency content was the blade pass frequency (BPF). The fan at the back of the wind tunnel caused an acoustic wave that traveled upstream into the test section at the BPF. The BPF (f_{BP}) in Hz is calculated in Equation (4.1) from the fan speed ω_{fan} in revolutions per minute (RPM) multiplied by the number of blades n .

$$f_{BP} = \frac{\omega_{fan} * n}{60} \quad (4.1)$$

Using Equation (4.1), Table 4.2 was created.

There were two sources of vibration in the SARL: one from the vortices shedding off the pod and the other from the acoustics of the fan. The sub-plate mounted on the

pedestal was the only common piece of hardware between the BAMF and HW test, so it was probably vibrating due to the BPF and transferring this vibration to the fin and HW.

Table 4.2: SARL BPF (Hz)

| Mach | Motor RPM | Fan RPM | BPF |
|------|-----------|---------|-------|
| 0.1 | 93.7 | 185.4 | 55.6 |
| 0.15 | 137.5 | 272.3 | 81.7 |
| 0.2 | 179.9 | 356.2 | 106.6 |
| 0.25 | 219.8 | 435.2 | 130.6 |
| 0.3 | 262.3 | 519.4 | 155.8 |
| 0.35 | 301.4 | 596.8 | 179.0 |
| 0.4 | 338.7 | 670.6 | 201.2 |
| 0.45 | 374.0 | 740.4 | 222.1 |
| 0.5 | 408.8 | 809.3 | 242.8 |

Figure 4.4 shows the HW PSD at $0.25M$ with the 12 in pod. The peak at 70 Hz that gradually rises and falls was the VSF from the pod. The sharp spike at 130 Hz was the BPF vibrating the HW apparatus itself. Figure 4.5 shows the fin PSD at $0.25M$ with the 12 in pod installed. The vortex shedding frequency was about 74 Hz, and the BPF spike can be seen at 131 Hz. The BPF vibrations had a narrower frequency bandwidth and were more powerful than the pod vortices, especially when coincident with a mode.

From the HW tests, the St was also found experimentally. This generally matched other work such as [31], where the St was found to be constant for $Re > 2.5 \times 10^4$. The lowest Re of 3.4×10^5 was at $0.1M$ with the 6 in pod. The highest Re of 2.6×10^6 was at $0.4M$ with the 12 in pod. The St as a function of M and pod diameter are shown in Figure 4.6, and the averages in Table 4.3.

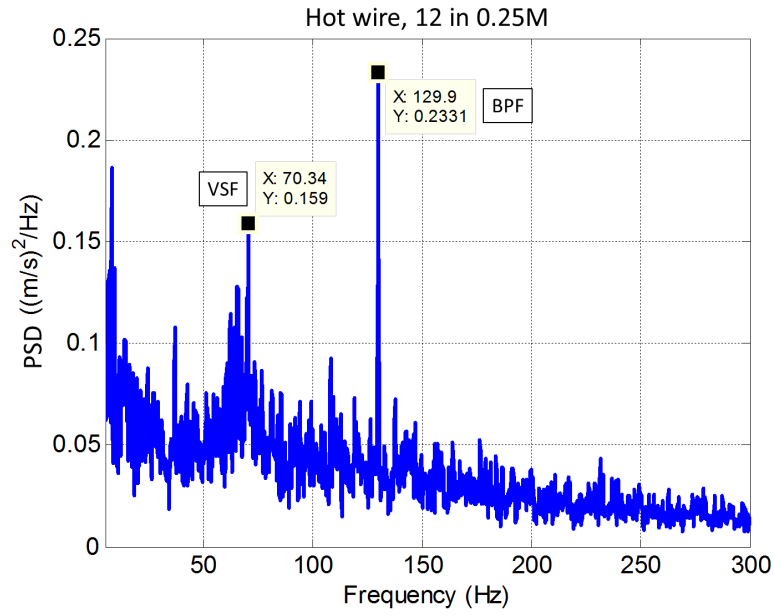


Figure 4.4: HW VSF at 70 Hz and BPF at 130 Hz

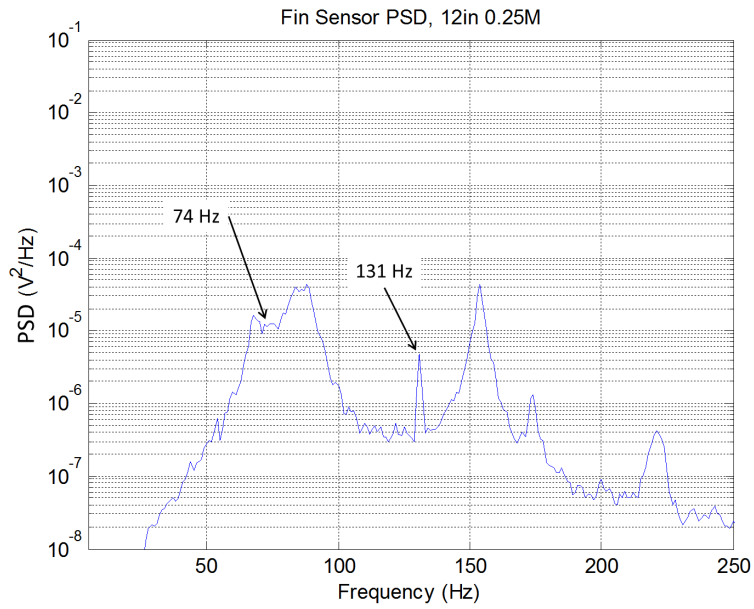


Figure 4.5: Fin sensor VSF at 74 Hz and BPF at 131 Hz

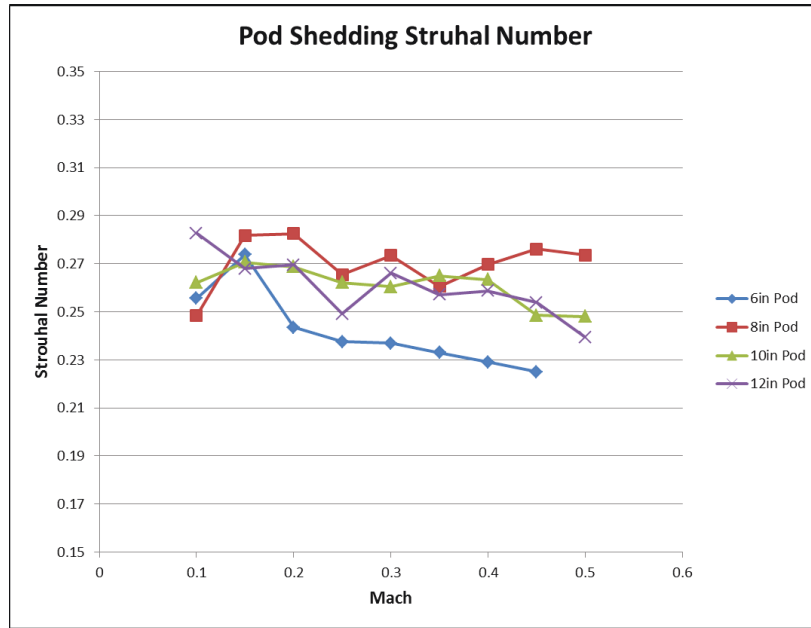


Figure 4.6: Strouhal number as a function of M for each pod

Table 4.3: Strouhal number averages for each pod

| | 12 in Pod | 10 in Pod | 8 in Pod | 6 in Pod |
|--------------|-----------|-----------|----------|----------|
| St Average | 0.26 | 0.26 | 0.27 | 0.24 |

The St calculations for the 6 in pod seem to deviate from the other three pods. It averages lower and seems to be decreasing compared to the other three pods. However, the BPFs closely matched the VSFs of the 6 in pod as M was increased, so the physical vibration of the HW may have induced errors into the 6 in pod St calculations. Overall, the trends show generally flat lines for the St which indicate it was insensitive to M and Re increases.

4.2.2 Test Conditions.

Conditions for BAMF testing varied from 2033-2056 ft PA, 72-81 degrees F, and up to 303.9 lbs per sq ft dynamic pressure at $0.5M$. Table 4.4 compared the VSF predictions

with the test day calculations. There was no direct method applied to specifically measure the VSFs. The numbers in bold were close to a mode of the fin.

Table 4.4: Predicted verses actual VSF (Hz)

| Mach | $V_{\infty}(ft/sec)$ | 12 in Pod Predicted | 12 in Actual | 6 in Pod Predicted | 6 in Actual |
|------|----------------------|---------------------|--------------|--------------------|-------------|
| 0.1 | 117 | 28 | 30 | 56 | 63 |
| 0.15 | 172 | 42 | 45 | 83 | 93 |
| 0.2 | 227 | 56 | 60 | 111 | 123 |
| 0.25 | 283 | 70 | 75 | 139 | 153 |
| 0.3 | 338 | 83 | 90 | 167 | 184 |
| 0.35 | 394 | 97 | 105 | 195 | 214 |
| 0.4 | 449 | 111 | 120 | 223 | 247 |
| 0.45 | 500 | 125 | N/A | 250 | 276 |
| 0.5 | 554 | 139 | N/A | 278 | 307 |

The difference between the predicted and actual was from the actual St being slightly higher than predicted and from test day conditions being warmer and having nearly double the pressure altitude of the assumed standard day at 1000 ft. The baseline vibration open-loop PSD level for $0.0M$ was $7 \times 10^{-10} V^2/Hz$. For tunnel installation, the accelerometer, MFC sensor, and actuator wiring was bundled together and run through a hole in the center of the base plate, through the pedestal, and under the wind tunnel to the BAMF control room next to the test section, requiring a length about 25 ft. Figure 4.7 shows the layout of the control room, with the simulated aircraft supply out of view to the left of the transformer.

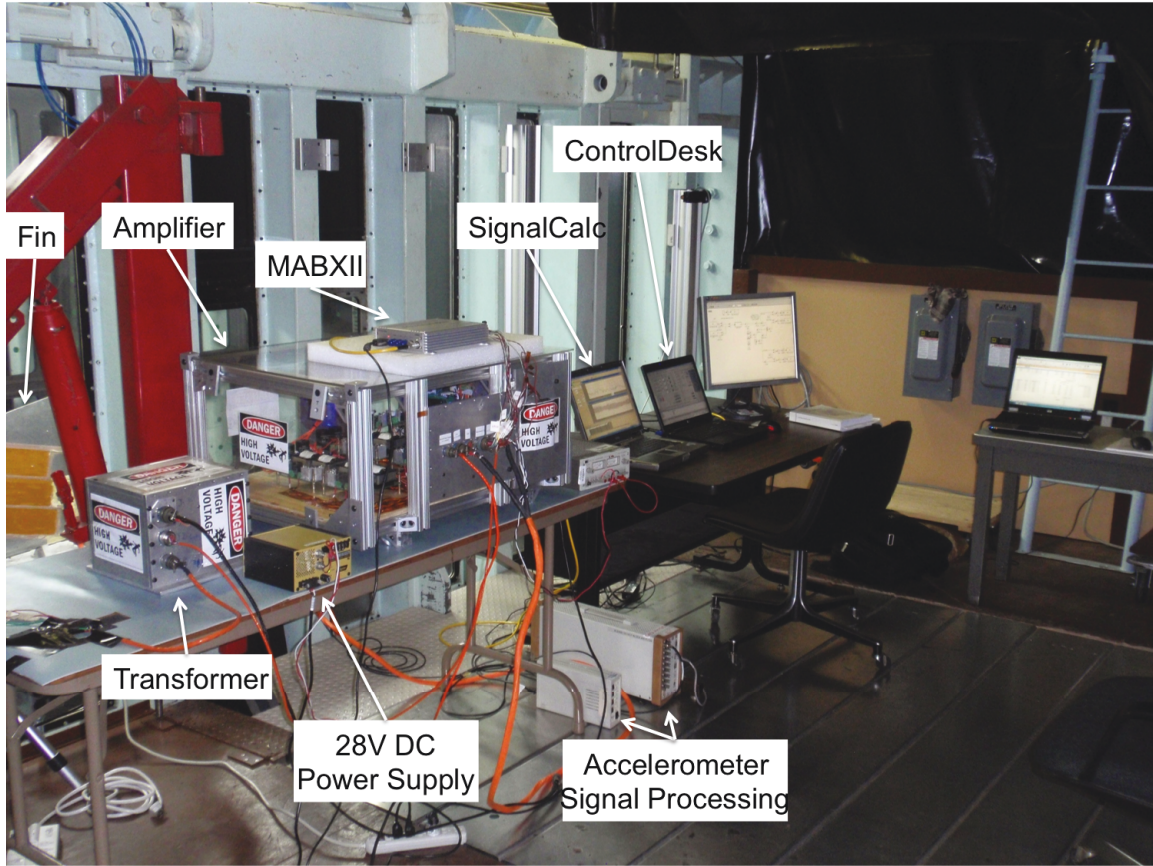


Figure 4.7: BAMF test setup at the SARL

4.2.3 *Vibration Characteristics.*

Baseline open-loop sensor data was taken with no pod, but with the aerostrut structure still installed, and compared to the 12 in and 6 in pod sensor data. Figure 4.8 compares the PSDs of the baseline, 12 in pod, and 6 in pod at 0.3M. The greater peak at mode two with the 12 in pod corresponded to the VSF at 90 Hz. The BPF was shown as the sharp spike at 155 Hz. The VSF of the 6 in pod was only about 28 Hz higher than the BPF, and contributed to the increased peak at mode three. The mode one shift with the 6 in pod was conspicuously 5 Hz greater than the baseline.

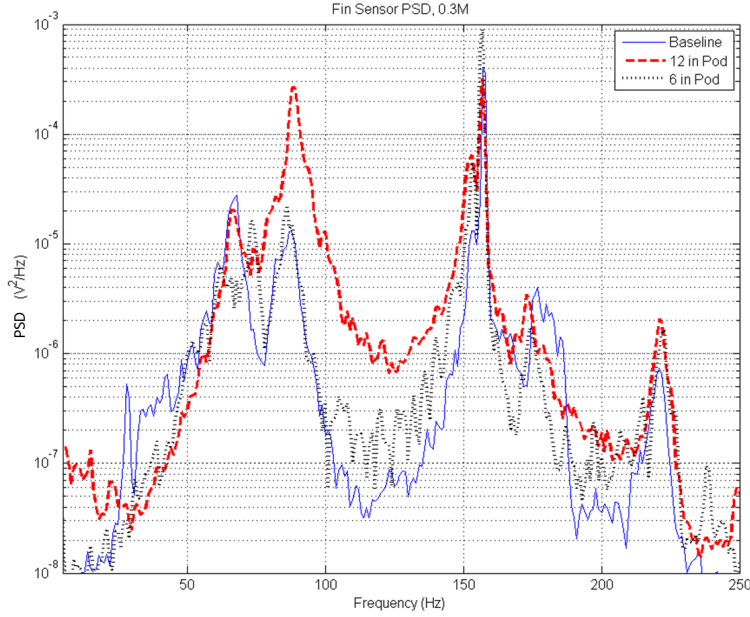


Figure 4.8: Open-loop PSDs of the baseline, 12 in, and 6 in pods at $0.3M$

The unipolar input into the MABXII set the limit for saturation. Figure 4.9 shows the maximum sensor input data values as percent of saturation. The baseline had a steady increase in vibration until $0.3M$ when the vibrations almost doubled. This was also seen to a greater extent in the 6 in pod, and was due to the BPF aligning with the third mode of the fin (~ 155 Hz) and coupled with the VSF of the 6 in pod. As the BPF increased at $0.35M$, the vibration decreased (6 in Pod) or leveled off (baseline). The vibration then increased, peaking at $0.45M$ as the BPF aligned with the fourth mode (~ 222 Hz), and then vibration decreased at $0.5M$. It was curious to note that the 12 in pod had less vibration than the 6 in pod at low speed. From Table 4.4, the 6 in pod is shedding vortices around the first and second modes (~ 69 and 88 Hz) at 0.1 - $0.15M$, while the 12 in pod is shedding from 30 - 45 Hz. As velocity increased from 0.2 - $0.3M$, the 12 in pod vortices begin to excite the first two modes, and vibration levels increase dramatically until the sensor input saturated at $0.35M$.

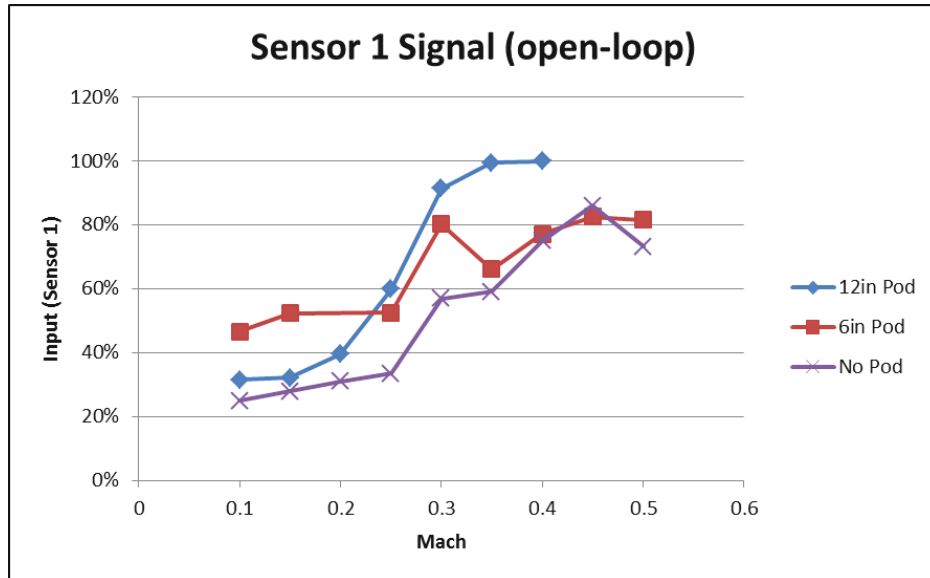


Figure 4.9: Fin sensor 1 signal magnitude as a function of M

Sensor input saturation is never desirable. When Ono encountered this with PPF controllers, the controller signals also saturated and caused the fin to lose stability and enter an limit cycle oscillation (LCO) condition [22]. With BAMF this did not happen, partly because of an input gain block just after the bipolar signal conversion that reduced the input signal into the controller. Sensor input saturation is a physical problem, and the input signal voltage from the amplifier to the MABXII should be reduced to provide proper signal input levels at expected conditions. It should also be noted that the sensor input was saturated for every data point from 0.1-0.5 M , regardless of the pod, when the loop was closed. From estimating the width of the signal input saturation and the slope of the line prior to saturation, it is estimated that signals up to approximately 3.5 would have been seen, when the input is limited to one. Adjusting the input gain block allowed the controller to continue to function, though at a reduced level. Even with the sensor input saturation, the PSD was still effective at detecting the appropriate frequencies. Figure 4.10 compares the fin sensor and the accelerometer. Under these closed-loop test conditions at 0.25 M with

the 6 in pod, the fin sensor input was saturated, but the signal content was still accurate. Note that the peak frequencies should be the same, but the shape of the PSDs may not be since the sensors were located on different parts of the fin (see Figure 3.3).

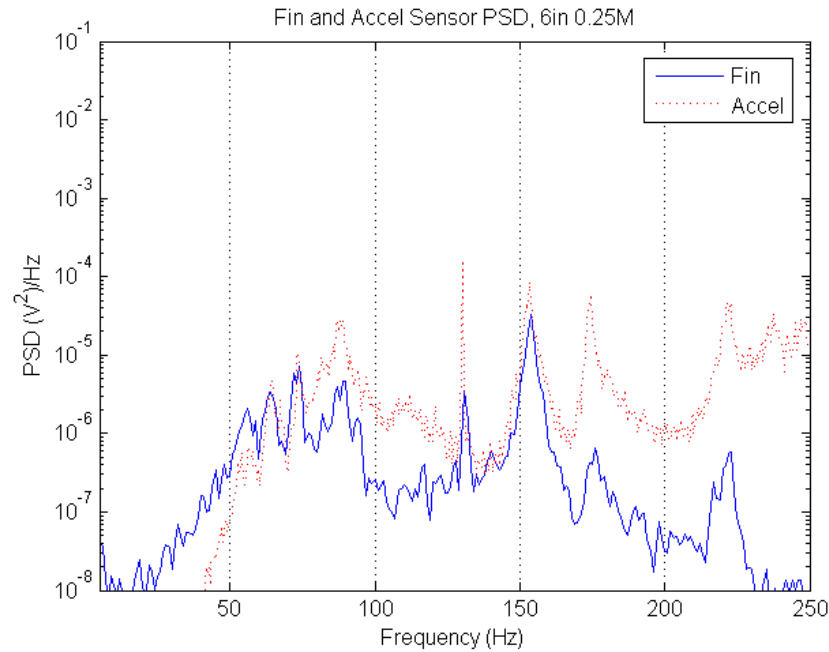


Figure 4.10: Comparison of accelerometer and fin sensor signal saturated PSDs

Figure 4.11 through Figure 4.14 show the PSD peaks for the first four modes of the fin, respectively. For mode one with the 12 in pod, vibrations increased at $0.2M$ as the VSF aligned with the modal frequency. As M increased, the peak remained relatively constant. For the 6 in pod, the mode one peak magnitude increased dramatically from $0.3M$ until peaking at $0.45M$. This was probably due to more vibration in the fin in general as the BPF aligned with modes three and four and airflow over the fin increased. In general for all modes, PSD peak magnitudes decreased as tunnel airflow approached $0.5M$. The BPF was the most energetic excitation of the fin, and the peak reduction was probably due to the BPF exceeding the first four modes of the fin and thus the vibration of the fin decreased.

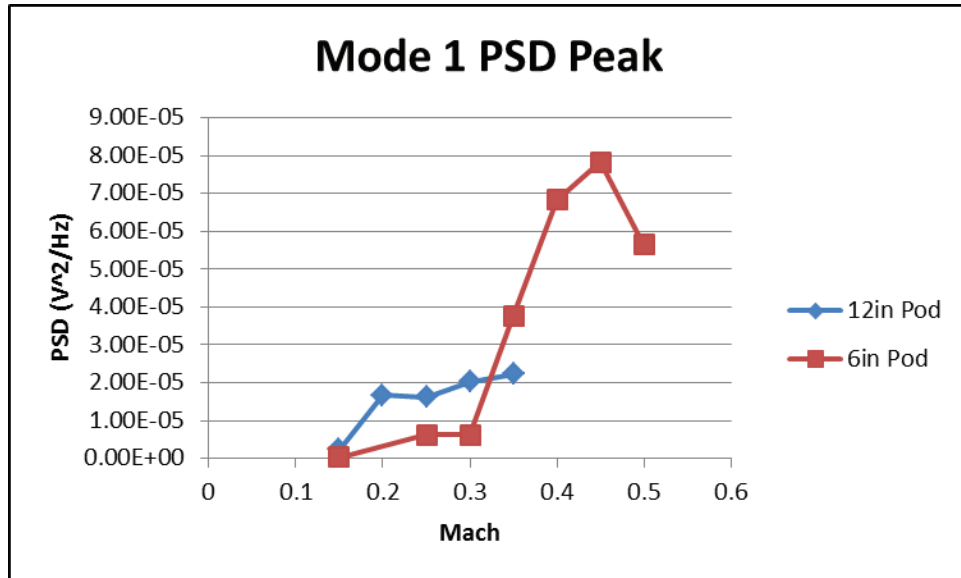


Figure 4.11: Mode 1 (~69 Hz) fin sensor PSD peak as a function of M

For mode two with the 12 in pod, vibrations increased dramatically at $0.3M$ as the VSF aligned with the modal frequency. As M and the VSF increased, the peak magnitude decreased. For the 6 in pod, the mode two peak was higher at $0.15M$ as both the VSF and BPF were imparting energy and then decreased at $0.2M$. Again, the peak was at $0.45M$ when the BPF energized mode four and increased the overall vibration of the fin.

Mode three with the 12 in pod had vibrations that increased dramatically at $0.3M$ as the BPF aligned with the modal frequency, and decreasing at $0.35M$. If wind tunnel power had been available, the VSF would have reached ~ 150 Hz at $0.5M$. For the 6 in pod, the BPF at $0.3M$ energized the fin even more than with the 12 in pod, with the peak decreasing at $0.35M$. The VSF of the 6 in pod was only about 15 Hz greater than the BPF at $0.3M$ and contributed to this increase.

Mode four with the 12 in pod had steady increases in vibration as M increased, but had low peak magnitudes compared to the other modes up to $0.35M$. For the 6 in pod, the

BPF at $0.45M$ dramatically energized the fin to the highest peak seen of any mode, with the magnitude decreasing at $0.5M$ to about twice that of $0.4M$.

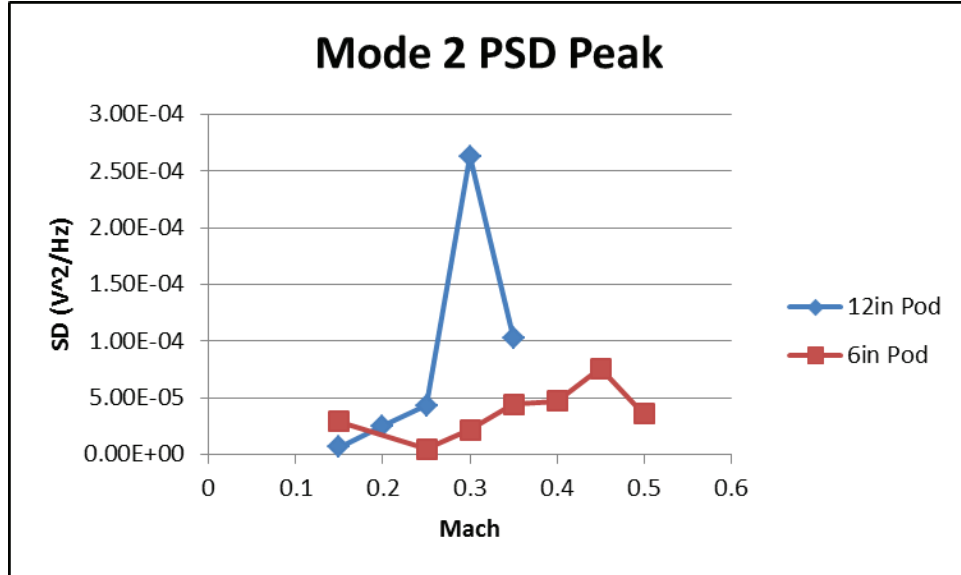


Figure 4.12: Mode 2 (~ 88 Hz) fin sensor PSD peak as a function of M

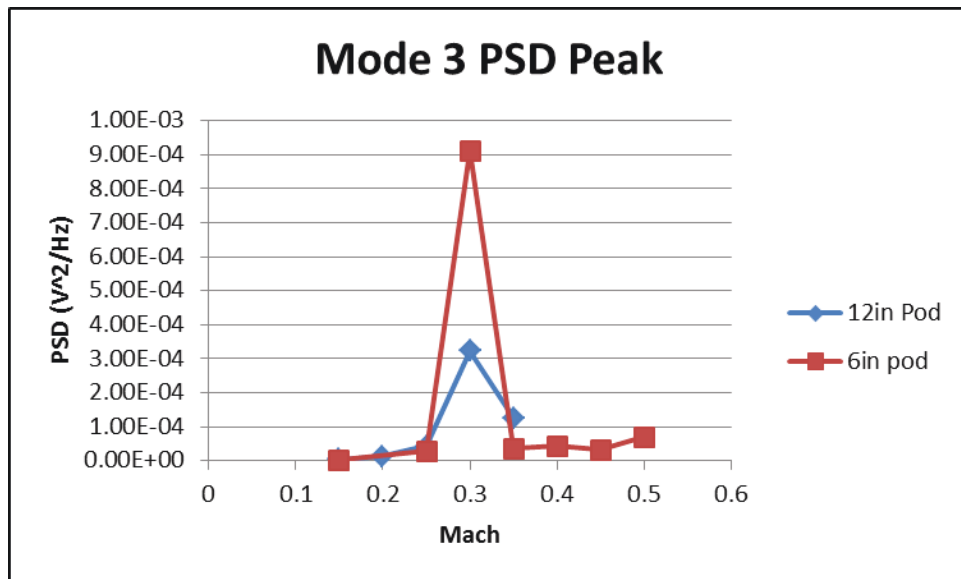


Figure 4.13: Mode 3 (~ 155 Hz) fin sensor PSD peak as a function of M

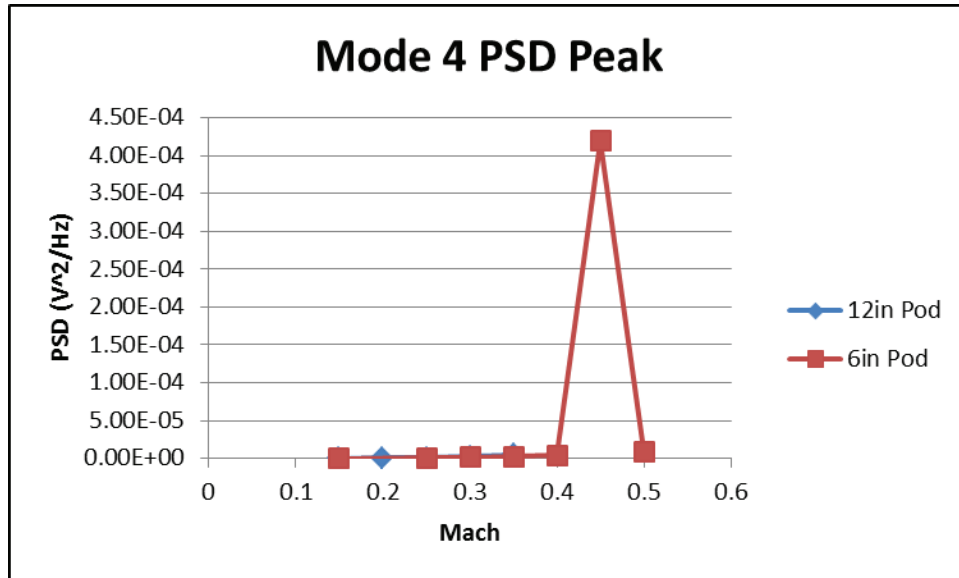


Figure 4.14: Mode 4 (~ 222 Hz) fin sensor PSD peak as a function of M

4.2.4 Peak Identification.

Frequency shifts in the magnitude of the PSDs were noted, but perhaps the most significant argument for adaptive control was the role played by the BPFs. Especially noted at $0.3M$ (Figure 4.8), the BPF was on the slope leading to the peak of mode three, but was about five Hz greater. Even though it was not exactly aligned with mode three, it was boosted by the response of the fin and was the dominant frequency. BAMF simply recognized it as the dominant frequency in a frequency region of interest (snapshot) and built a controller to damp it. This was just one example of the modal frequency shifts noted during wind tunnel testing (Table 4.5).

Table 4.5: Modal frequency shifts during SARL testing (Hz)

| | Mode 1 | Mode 2 | Mode 3 | Mode 4 |
|-------------|--------|--------|---------|---------|
| Frequencies | 68-76 | 86-92 | 151-157 | 218-223 |
| Delta | 8 | 6 | 6 | 5 |

Figure 4.15 through Figure 4.18 show the open-loop peak frequencies of each mode for the 12 in and 6 in pod as M number changes. For mode one, there was a slight decreasing frequency trend with the 12 in pod as M increased. While the frequency was relatively constant with the 6 in pod, the modal frequency was about five Hz higher than with the 12 in pod.

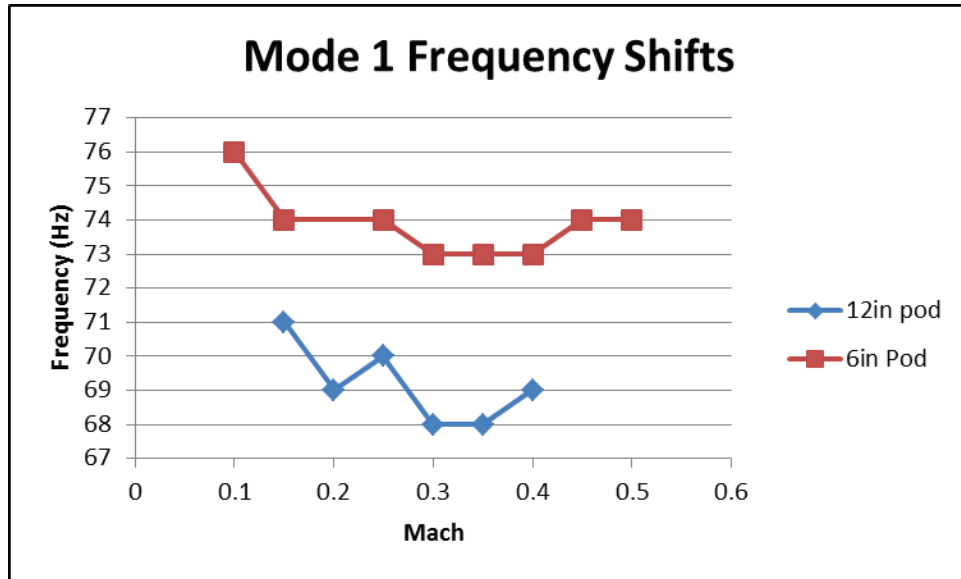


Figure 4.15: Mode 1 (~69 Hz) fin sensor PSD frequency shift as a function of M

Mode two frequencies were similar between the 12 in and 6 in pod, with a decreasing trend as M increased. Mode three frequencies also showed a decreasing trend as M increased, with the 12 in pod showing a slightly lower frequency. Mode four frequencies with the 12 in pod showed a decreasing trend as M increased, and were lower than with the 6 in pod. The modal frequency with the 6 in pod was relatively constant until a five Hz shift at $0.5M$.

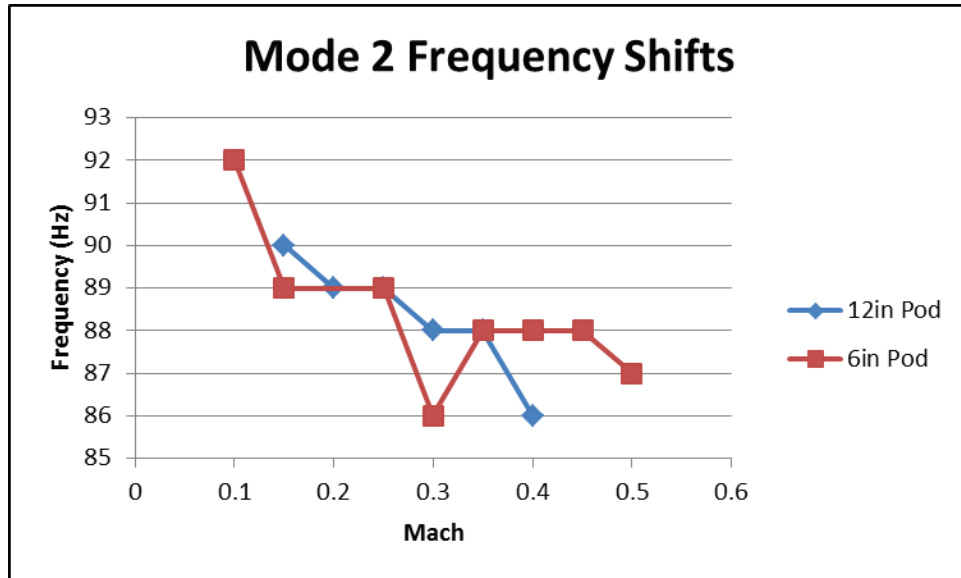


Figure 4.16: Mode 2 (~88 Hz) fin sensor PSD frequency shift as a function of M

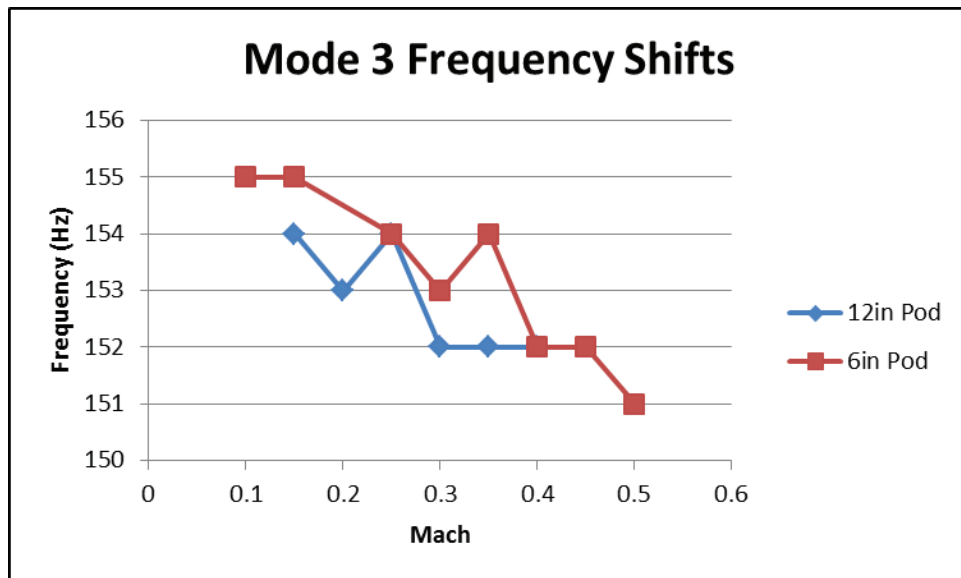


Figure 4.17: Mode 3 (~155 Hz) fin sensor PSD frequency shift as a function of M

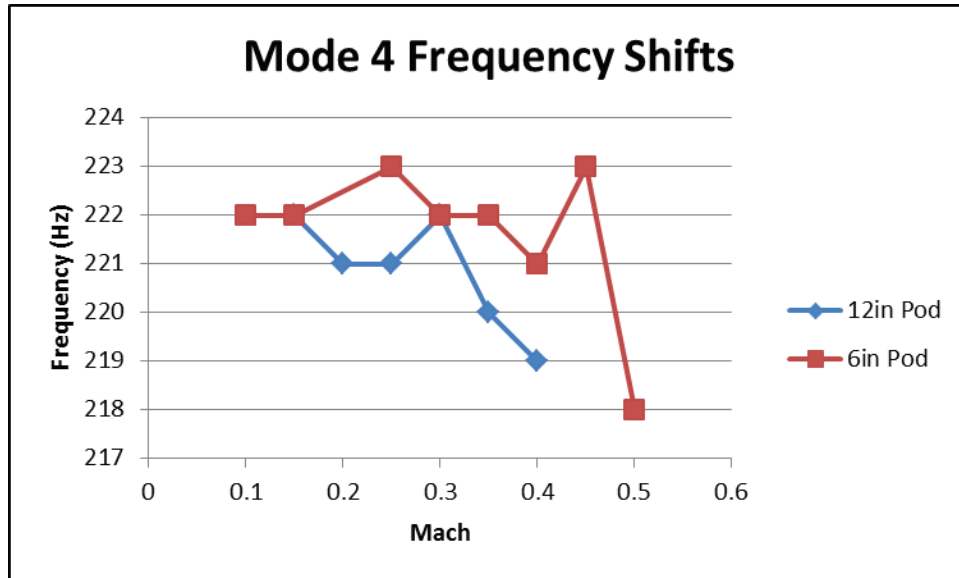


Figure 4.18: Mode 4 (~222 Hz) fin sensor PSD frequency shift as a function of M

Figure 4.19, Figure 4.22, Figure 4.25, and Figure 4.28 show the snapshots over a 19 second test period with the 6 in pod at $0.35M$ as a function of time, both open and closed-loop, of what dominant frequency was detected. From inside BAMFs software, the controllers were rebuilt every second if a different dominant frequency was detected based on the PSD. The time traces reveal the variability of the one second PSD dominant frequency when the loop was closed. When a mode was significantly damped, the dominant frequency was pushed down closer to the noise floor. This would result in greater variability of the one second PSD as it tried to identify the actual dominant frequency over the noise. The precise nature of PPF chased each peak, yet was still able to effectively damp over the snapshot range of frequencies for the mode. Modes one open-loop varied from 70-75 Hz, but when the loop was closed varied from 63-77 Hz. Mode two also had significant peak reduction, with the open-loop PSD varying from 82-89 Hz, and varying from 77-92 Hz when closed-loop. Mode three maintained its identity even when damped, and mode four was affected by instabilities.

The 19 second averaged PSD for the 6 in pod at $0.35M$ was shown in Figure 4.37. The PSD snapshots below show each one second PSD over 19 seconds for both open and closed-loop. The circled peaks are the top peak and its associated frequency for each second that a controller was built to damp. Note the differences in PSD peak magnitude indicated on the y-axis between the open-loop (left) and the closed-loop (right). A closed-loop instability was apparent above the mode four PSDs, and drew the controller to the upper edge of the mode four snapshot.

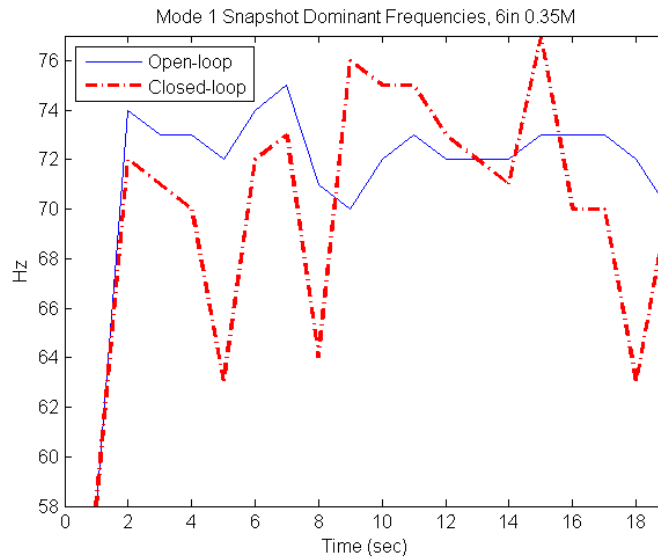


Figure 4.19: Mode 1 (~69 Hz) fin sensor PSD frequency shift as a function of time

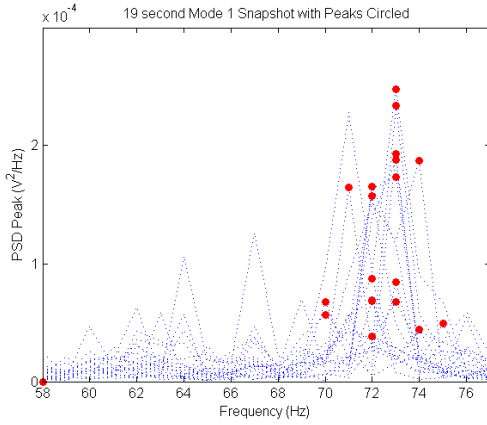


Figure 4.20: Open-loop mode 1 PSD snapshot

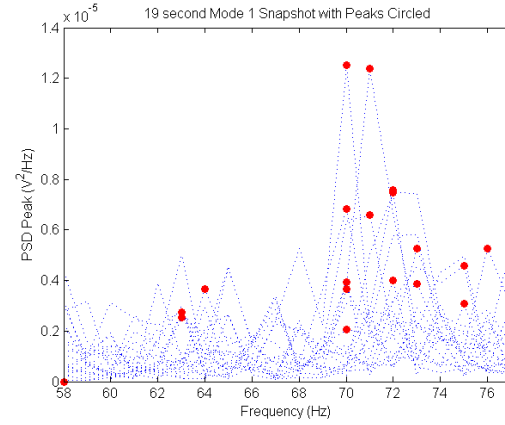


Figure 4.21: Closed-loop mode 1 PSD snapshot

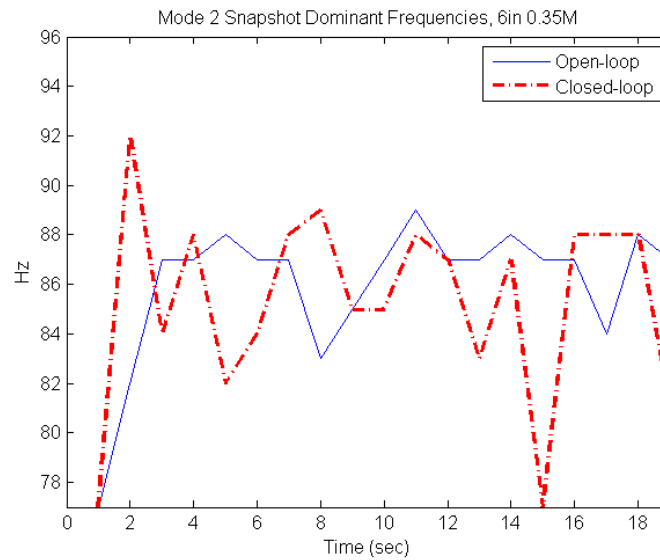


Figure 4.22: Mode 2 (~88 Hz) fin sensor PSD frequency shift as a function of time

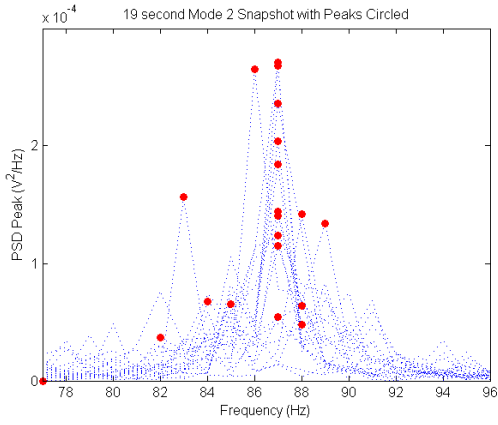


Figure 4.23: Open-loop mode 2 PSD snapshot

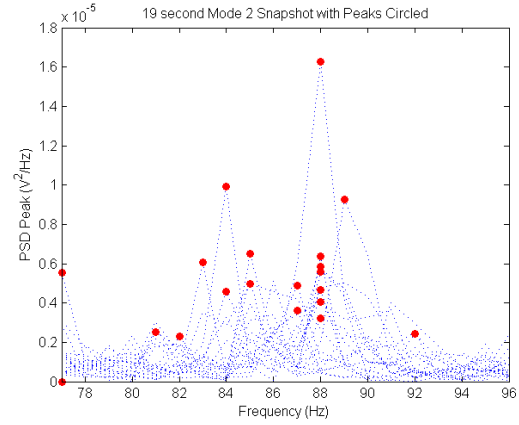


Figure 4.24: Closed-loop mode 2 PSD snapshot

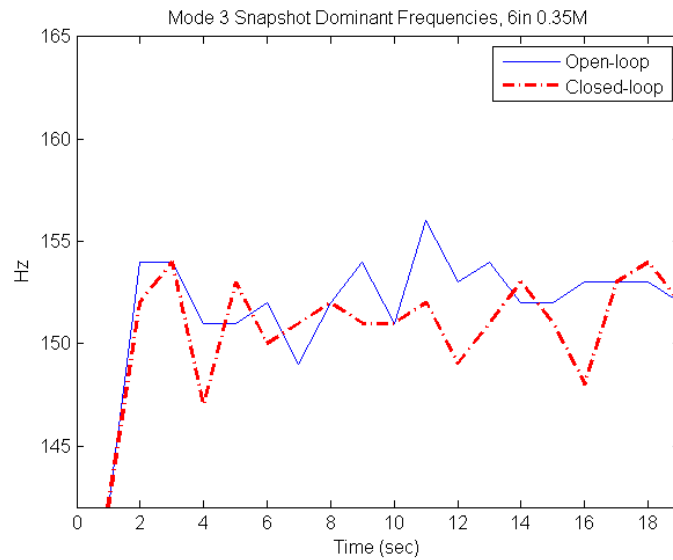


Figure 4.25: Mode 3 (~155 Hz) fin sensor PSD frequency shift as a function of time

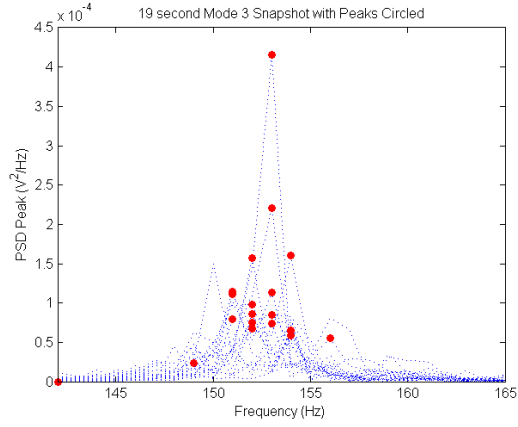


Figure 4.26: Open-loop mode 3 PSD snapshot

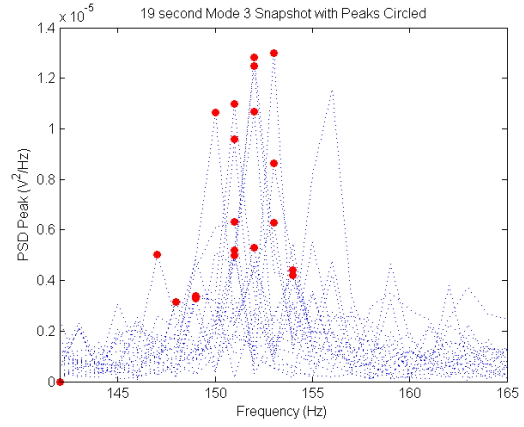


Figure 4.27: Closed-loop mode 3 PSD snapshot

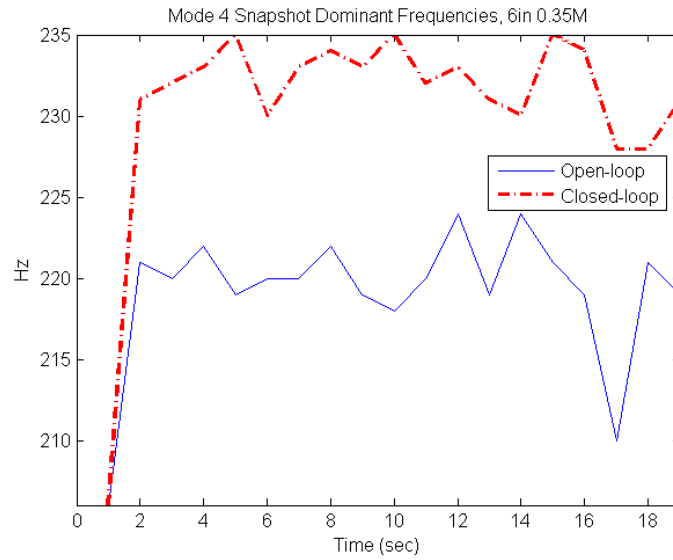


Figure 4.28: Mode 4 (~222 Hz) fin sensor PSD frequency shift as a function of time

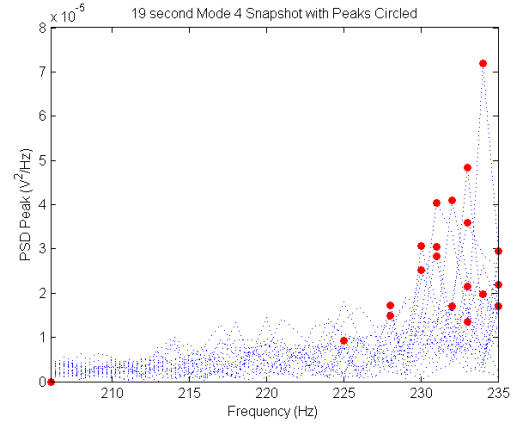
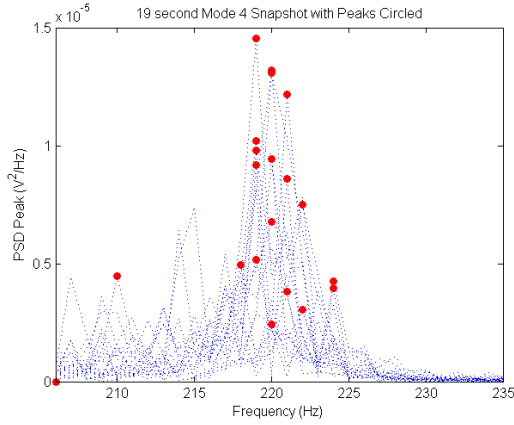


Figure 4.29: Open-loop mode 4 PSD snap- shot
Figure 4.30: Closed-loop mode 4 PSD snap- shot

4.2.5 Control Selection.

Gains were originally going to be adjusted when the tunnel was running, looking to find both optimal damping and when stability would begin to be compromised. The limited time that became available in the wind tunnel resulted in nominal gains (1, 1, 1, 1) used for the 12 in pod tests. Limited study was conducted to optimize the gains the next test morning while waiting for favorable weather conditions. Because the fin was already installed in the wind tunnel, data collection methods had to be improvised. Four signal generators built into the software were activated and the signals sent through one group of MFC patches. The accelerometer was the only frequency domain feedback available real-time; the reduction of PSD peaks was used to measure whether a gain adjustment was benefitting damping or not. Due to time constraints, only integer numbers were varied for the gains. The initial set of gains for the 6 in pod was 0, 3, 3, 1. If a gain was greater than zero for the first mode, it seemed to reduce the damping to the other modes, especially mode two. This was probably due to both modes being so close to each other and mode two being more dominant, and so the controller was wasting unnecessary control power on mode one. Periodically, gains were adjusted as the tunnel was running to gather more data. From 0.35M-0.5M with the 6

in pod, the gains were increased to 0, 5, 7, 1. This lead to brief periods when the controllers saturated. Figure 4.31 shows the control signal limit from 0 to 1, and the saturated signal as brief flat amplitudes.

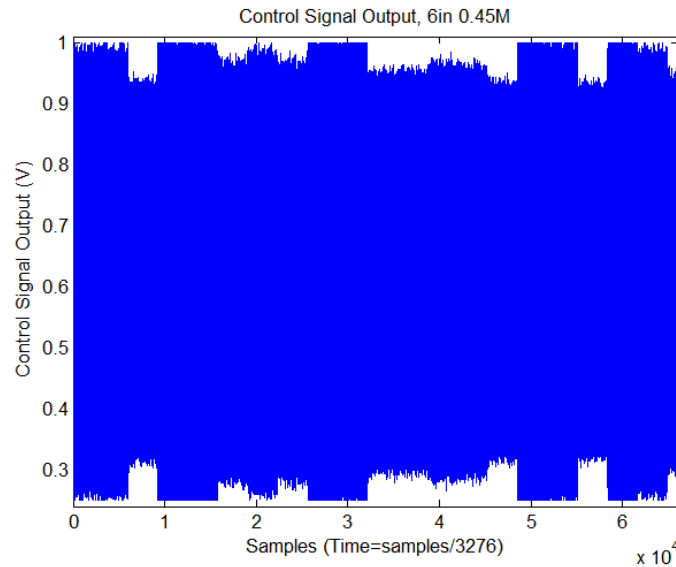


Figure 4.31: Control signal saturation

The system maintained stability and recovered to continue to control. From PSD analysis (Figure 4.32), the controller seemed to maintain effectiveness. This revealed increased robustness of the controller over previous work, when a LCO condition was experienced with controller saturation that could only be rectified by shutting down the controller and restarting the system. At the far right of Figure 4.32, an instability can be seen that is discussed in greater detail in section 4.2.6. This was consistent whenever the controller was turned on across various M numbers.

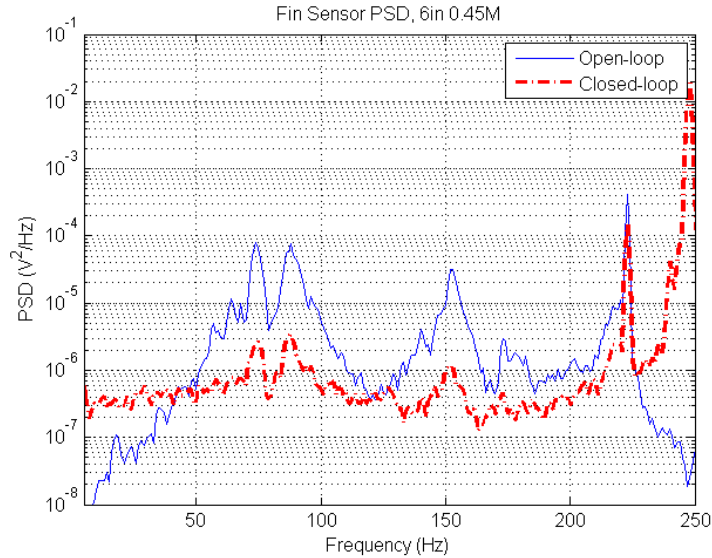


Figure 4.32: Comparison of PSDs with control signal saturation

4.2.6 Damping Determination.

Because the highest mode of interest of the fin was at 222 Hz, a chirp input signal was used from 0.1 Hz to 300 Hz to characterize the BAMF system. It was distributed over 15 sec to try to slow the frequency rate of change, but it still covered about 17 Hz per sec. A chirp is a well-known way of identifying the FRF of a system, but in hindsight it may not have been best for this application. Many controllers are fixed, and the FRF can be generated by a chirp input signal. But because BAMF moves the controllers to respond to changing frequencies, and has an inherent lag in identifying the change due to the PSD, the controller would always be chasing this chirp signal and never be on parameters for optimal damping. In essence, the chirp signal was an unrealistic way of determining the damping of BAMF. BAMF was designed to damp in the real world flight test environment; from Browning's flight data, there were no flight conditions/maneuvers that caused a modal frequency shift as quickly as 17 Hz per sec. It would have been more accurate to use an impulse input instead. Because of this, the actual damping performance of BAMF was probably better

than what the FRFs reveal. Additionally, the input of the chirp was too large relative to the vibration levels. In the fin sensors, the PSDs looked like a series of one-sided sine waves, because each second of data had a large spike from the chirp. However, since the chirp went to 300 Hz, there were a few seconds when it was not in the window of interest from 50-250 Hz. Additionally, data was recorded with the chirp off, both open and closed-loop, so clean PSD data were gathered from these conditions. Even so, there were some identifiable FRF damping successes. The highest levels of vibration occurred at 0.3M when the BPF aligned with the third mode at 155 Hz. With the 12 in pod, the VSF was around 90 Hz, close to mode two. There was a -1.5 dB reduction for mode two, and -6.2 dB reduction for mode three (Figure 4.33). While modes one and four were actually amplified and the general noise floor was increased, Figure 4.34 shows a decrease in frequency amplitude for almost all frequencies below 200 Hz. Table 4.6 summarizes the PSD peak reductions.

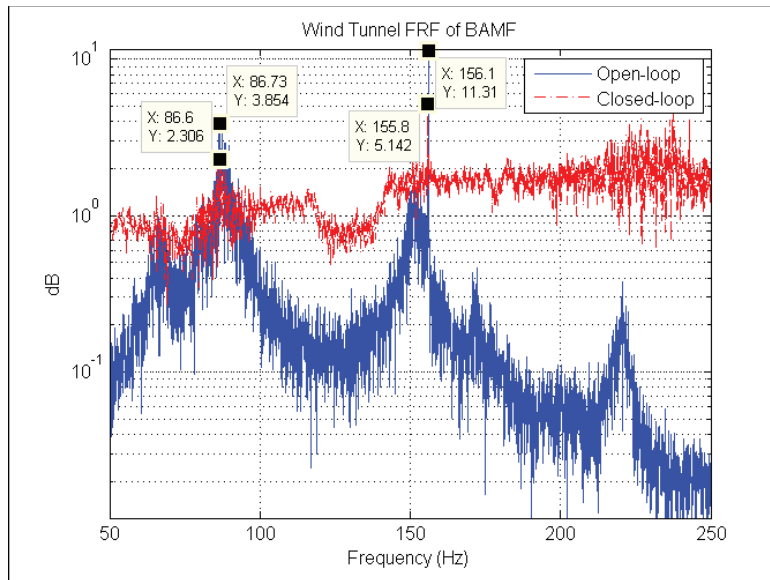


Figure 4.33: Comparison of open and closed-loop PSDs for 12 in pod at 0.3M

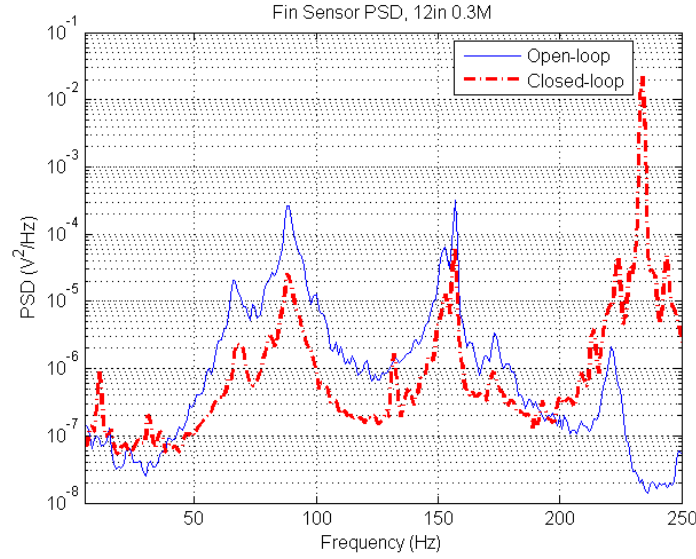


Figure 4.34: Comparison of open and closed-loop PSDs for 12 in pod at 0.3M

Table 4.6: PSD peak reduction for 12 in pod at 0.3M

| | Mode 1 | Mode 2 | Mode 3 | Mode 4 |
|----------|---------|----------|---------|--------|
| PSD Peak | -9.5 dB | -10.1 dB | -7.3 dB | 6.2 dB |

As noted earlier, the magnitude of the FRF probably shows less damping than actual because of the input signal used, but the noise floor was also increased partly due to the digital controller. The physical implementation of a digital controller adds noise to the control signal, and so does the amplifier boosting control signals with high voltage. The baseline noise level caused by these factors was not established.

Note that different gains were used between the 12 in pod and the 6 in pod; this was described in greater detail in section 4.2.5. With the 6 in pod at 0.3M, the VSF was around 183 Hz, between mode three and four. There was a -12.5 dB reduction for mode three. Again, the FRF shows mode one, two and four were actually amplified and the general

noise floor was increased, yet the PSD shows a decrease in frequency amplitude for almost all frequencies below 200 Hz and even some attenuation for mode four. Both Figure 4.34 and Figure 4.36 were taken from open and closed-loop data without the chirp signal, so they represent the pure frequency content of the fin without any additional inputs. Table 4.7 summarizes the PSD peak reductions.

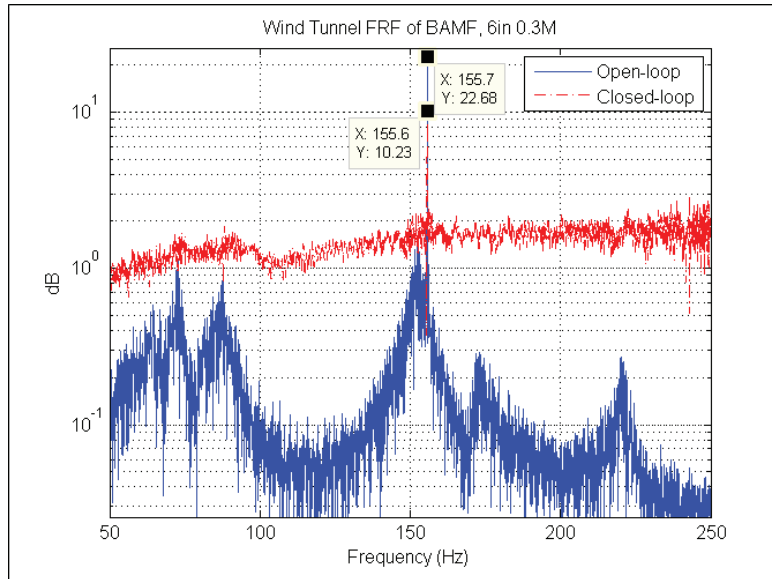


Figure 4.35: Comparison of open and closed-loop FRFs for 6 in pod at $0.3M$

Table 4.7: PSD peak reduction for 6 in pod at $0.3M$

| | Mode 1 | Mode 2 | Mode 3 | Mode 4 |
|----------|---------|----------|---------|---------|
| PSD Peak | -8.7 dB | -12.3 dB | -9.6 dB | -3.3 dB |

With the known limitations of the FRFs, the PSDs provided the most accurate information on the effects of the controllers.

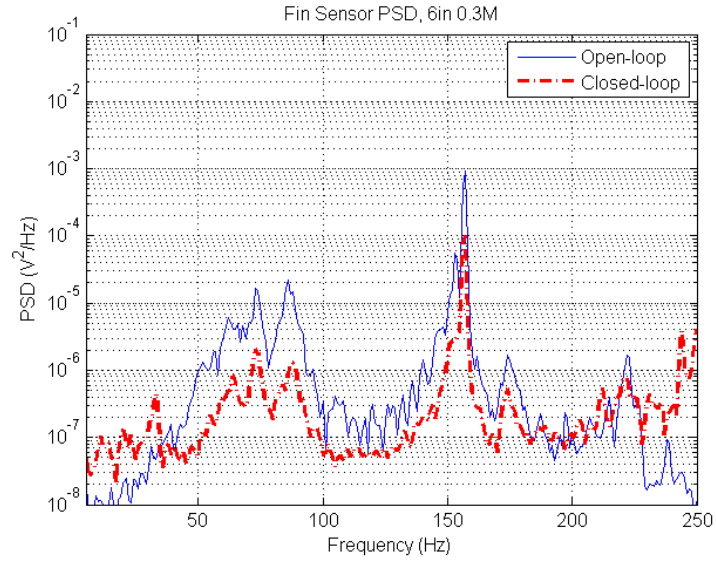


Figure 4.36: Comparison of open and closed-loop PSDs for 6 in pod at 0.3M

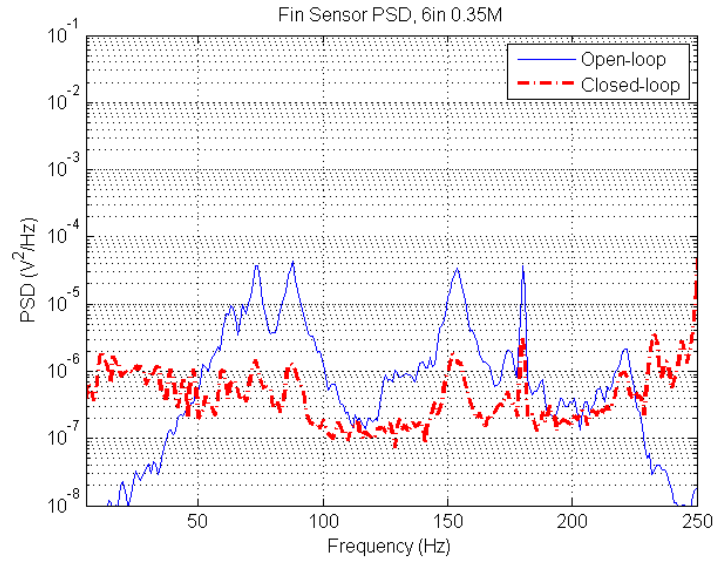


Figure 4.37: Comparison of open and closed-loop PSDs for 6 in pod at 0.35M

Figure 4.37 shows significant peak reductions in all four modal frequencies with the 6 in pod at 0.35M.

Table 4.8: PSD peak reduction for 6 in pod at $0.35M$

| | Mode 1 | Mode 2 | Mode 3 | Mode 4 |
|----------|----------|----------|----------|---------|
| PSD Peak | -14.1 dB | -15.3 dB | -12.7 dB | -3.5 dB |

Figure 4.38-Figure 4.41 show the PSD peak reductions with both the 12 in and 6 in pods for the first four modes of the fin. Note that higher gains were used with the 6 in pod, and the gains were increased again for velocities above $0.3M$.

For mode one with the 12 in pod, the greatest peak reduction was at $0.2M$, when the VSF was near mode one. The PSD peak levels increased overall as M increased, so the peak reductions with the current gains were less effective at higher M . For the 6 in pod, it was intuitive that if there were not significant vibrations seen, the controller did not reduce the vibration by much. Mode one became more pronounced as M increased, so peak reduction was greater as the first mode peak began to grow above the noise floor. Significant decreases in peaks were seen when the gains were increased at greater than $0.3M$.

Mode two with the 12 in pod showed the same general trends as mode one, with the best peak reduction at 0.15 - $0.2M$, where the BPF was the primary excitation. The peak reduction decreased as overall vibration levels increased with increasing M . For the 6 in pod, the large peak reduction at $0.15M$ corresponded to the BPF and VSF exciting the mode. Reduction was not as profound at $0.25M$ because mode two was not as well defined. There was a decrease in the peak magnitude by about -3 dB when the gains were increased at $0.35M$. Peak reductions continued to be significant up to $0.5M$. This mode was specifically targeted by the orientation of the MFC patches.

Mode three with the 12 in pod showed the same general trends as mode one, with the greatest peak reduction at $0.2M$. For the 6 in pod, peak reductions slightly increased up

to $0.3M$, but greater reductions were seen when the gains were increased at $0.35M$. This mode also was specifically targeted by the orientation of the MFC patches.

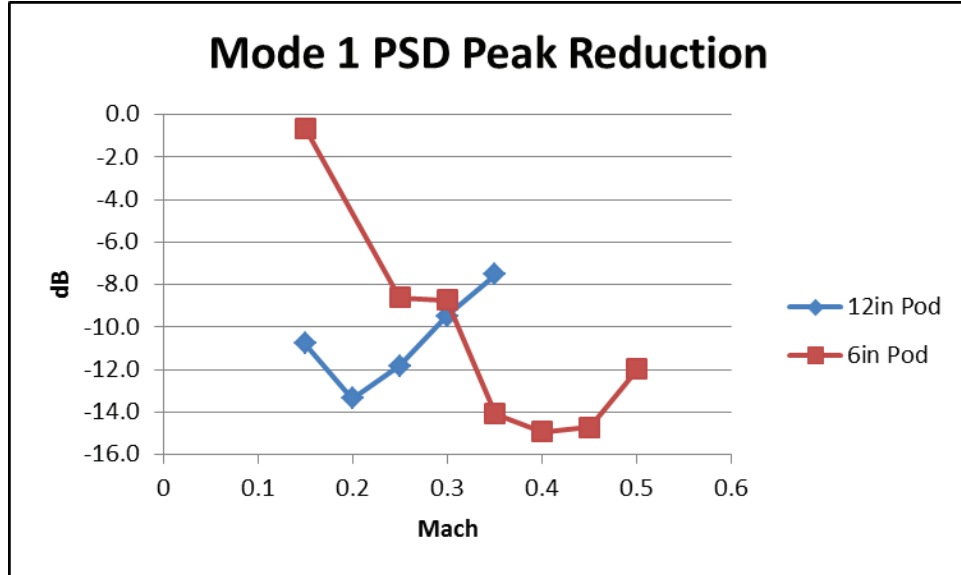


Figure 4.38: Mode 1 (~ 69 Hz) fin sensor PSD peak reduction as a function of M

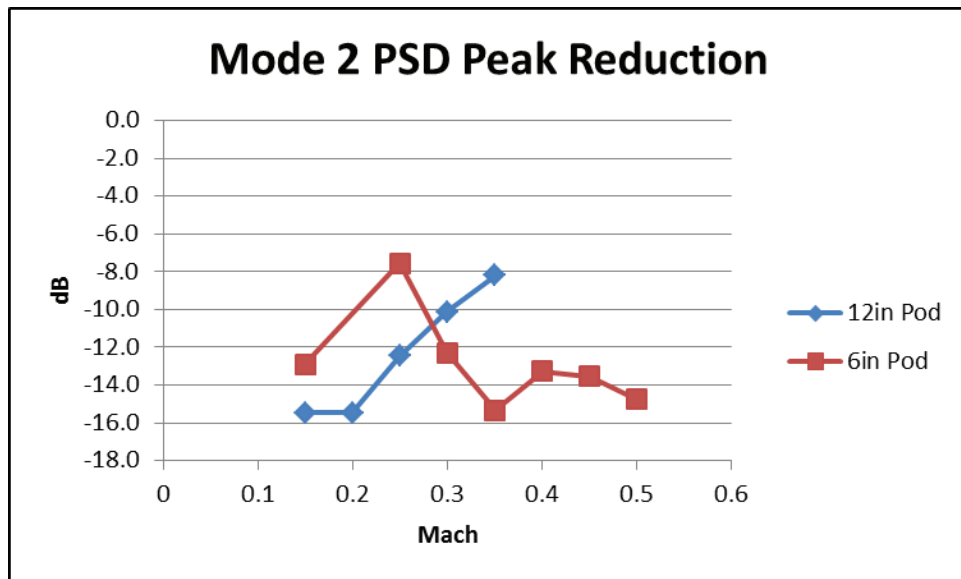


Figure 4.39: Mode 2 (~ 88 Hz) fin sensor PSD peak reduction as a function of M

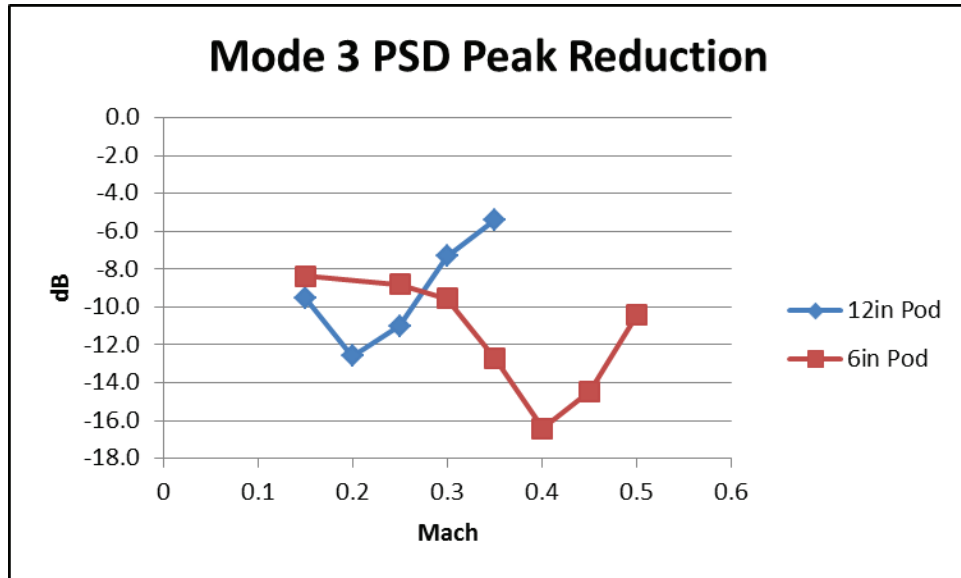


Figure 4.40: Mode 3 (~155 Hz) fin sensor PSD peak reduction as a function of M

Mode four with the 12 in pod was affected significantly by a frequency spike at around 234 Hz whenever the controller was turned on. This was probably an instability due to high gains as phase margin decreased at higher frequencies. This instability was also seen at higher frequencies around 255 Hz with the 6 in pod. Testing with the 6 in pod used different gains than the 12 in pod, which accounts for the difference in the instabilities. Unfortunately, stability analysis was unable to be performed due to the time schedule. For the 6 in pod, an poorly defined mode four at lower M resulted in no reductions. However, low reductions of about -3 to -4 dB were noted as the mode was excited by the VSF at $0.35M$ and the BPF at $0.45M$. The MFC patches were not at an optimum orientation to detect and control mode four, and it may be desirable to eliminate future attempts to control mode four with this MFC orientation.

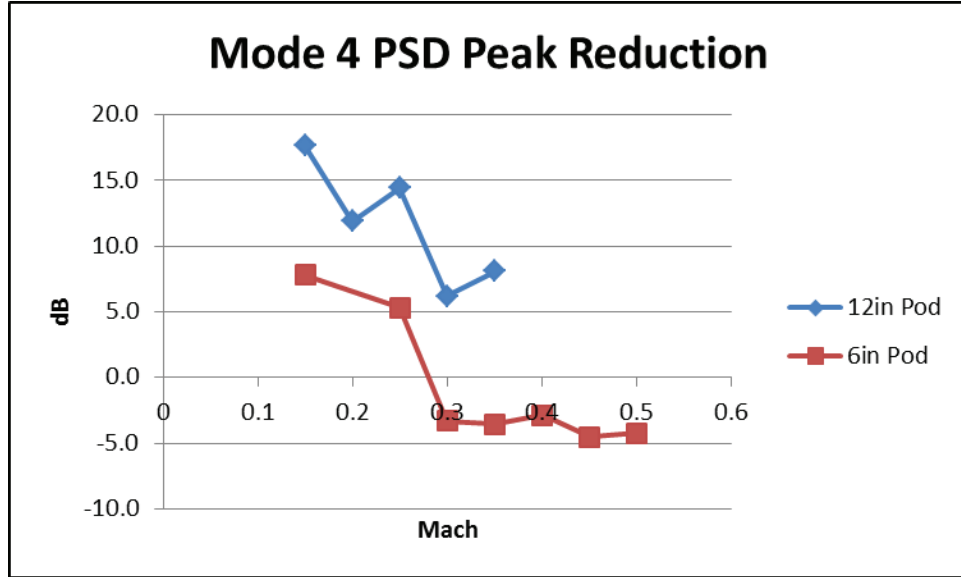


Figure 4.41: Mode 4 (~ 222 Hz) fin sensor PSD peak reduction as a function of M

4.3 Summary

The ability of the control software to identify and adapt to changing modal frequencies was proven in the laboratory. Additionally, the amplifier output did not meet the design specifications, so software fixes were implemented to protect the MFC patches from excessive voltage. During wind tunnel testing, the St proved to be constant and both VSFs and BPFs shifted the modal frequencies of the fin. The BAMF system successfully identified the shifts and reduced the vibrations significantly. Even with the sensor input signal and controller output signal saturated, the system maintained stability and control effectiveness. The next chapter summarizes this thesis and provides recommendations for future research.

V. Conclusions

5.1 Summary

In an airborne environment, the focus of this and previous research has centered on the primary excitations on the fin being caused by buffet from the LANTIRN TGP. As was seen in wind tunnel testing, additional external influences on the vibration of the fin, such as acoustic or shock wave interactions, may be difficult to model or even predict. These can change the plant model significantly, especially as M changes and in conjunction with various external stores configurations, such as the presence or absence of a centerline ALQ-131 electronic countermeasures pod. This increased number of complex variables, with the potential of unknown factors, reveal the greatest need for adaptive control.

The BAMF adaptive software could be applied to a wide array of control hardware. The primary limitation of the universality of the BAMF software was the dependence on the proper positioning of the sensors and actuators. If a sensor was located on a node, then that mode of vibration would not be detected nor properly controlled. While the software could be used with any numbers or types of sensors and actuators, the placement of these sensors/actuators would be unique to each structure. It was essential to properly align the piezoelectric fibers with the targeted modal principal strain directions. BAMF's MFC patches were primarily aligned with modes two and three, but reductions were seen in modes one and four as well.

5.1.1 Hardware.

The transformer, amplifier box, and fin had been modified into a reliable functioning, easily transportable system with robust connections. The amplifier maximum negative voltage of $-728V$ exceeded the $-500V$ MFC patch limitation, so the output signal was limited by the software to protect the patches. Additionally, the maximum positive was only $+570V$, which was lower than the designed voltage of $+700V$. The easiest way to

improve the voltage output would be to just reverse the polarity. The modifications of the fin for wind tunnel testing allowed the system to function up to the wind tunnel maximum velocity of $0.5M$ without any issues. The fin sensor signal input saturated with the 12 in pod at $0.35M$ and whenever the loop was closed, so the voltage incoming to the MABXII should be reduced to prevent this from reoccurring. Even with the primary sensor saturated, the PSD was still accurate as verified by the independent accelerometer sensor.

5.1.2 Software.

PPF control proved to be effective and very adaptable when coupled with a PSD of the plant. Limited testing did not allow optimized gains. The chirp signal was not ideal for generating an accurate FRF; a impulse signal should be used. Even with less than accurate data from the FRFs, a -12.5 dB reduction was seen in mode three. PSD peak reductions presented a more accurate picture of the effectiveness of the controller, with maximum modal peak reductions of -14.1, -15.3, -12.7, and -3.5 dB respectively, with the 6 in pod at $0.35M$. Gains were increased until the controller saturated. The system remained stable and maintained effective damping, proving an increased robustness over previous designs.

5.1.3 Wind Tunnel.

From PSD analysis, the vortex shedding strength was greater with the larger diameter pod and created greater vibration in the fin. However, the sharp BPF created the highest PSD peaks when aligned with the modes of the fin. The St proved to continue to be constant at about 0.26 as Re increased up to 2.6×10^6 . This allowed real time calculation of the VSF. Wind tunnel testing did reveal the desired modal frequency shifts to exercise the adaptive software. Modal shifts were 8, 6, 6, and 5 Hz, respectively, with modal frequencies tending to decrease as M increased.

5.2 Recommendations

These recommendations are in order of importance before future testing is attempted, given enough time to do them. Generally, the hardware fixes should be made first, then the

system noise characterized and stability determined. Afterwards, software enhancements can be investigated before more experimental testing.

1. Reduce the sensor signal input to prevent saturation.
2. Increase the positive voltage output of the amplifier.
3. Characterize the ability of the amplifier to process input and output signals and their magnitudes, including the effects of noise.
4. Conduct stability analysis on the system.
5. Investigate gain optimal tuning, perhaps an automatic tuning system to update the gains based on the environment.
6. Fenik et al. notes that several authors suggest that PPF is more effective if the control frequency is shifted to 1.3-1.45 times the natural frequency of the mode desired to be damped. This should be investigated to see if it can have tangible benefits for BAMF [10].
7. Increase BAMF's responsiveness to shifting frequencies.
8. Investigate adding additional sensor signals in the frequency domain.
9. Re-examine the damping by using an impact input signal instead of a swept signal.

VI. Appendix A

Figure 6.1-Figure 6.18 show the HW data for the 12 in and 6 in pods. The VSF and the BPF are marked.

Figure 6.19-Figure 6.27 compare the baseline with no pods but aerostrut structure installed, the 12 in pod, and the 6 in pod uncontrolled PSDs.

Figure 6.28-Figure 6.40 compare the uncontrolled and controlled PSDs of the 12 in pod and 6 in pod at various M numbers.

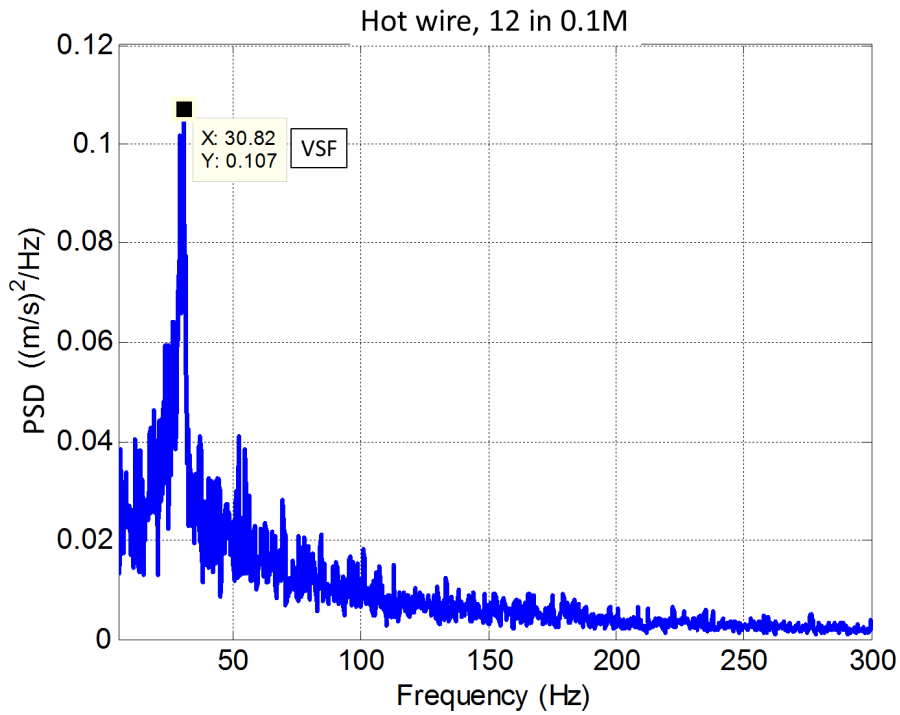


Figure 6.1: HW PSD with the 12 in pod

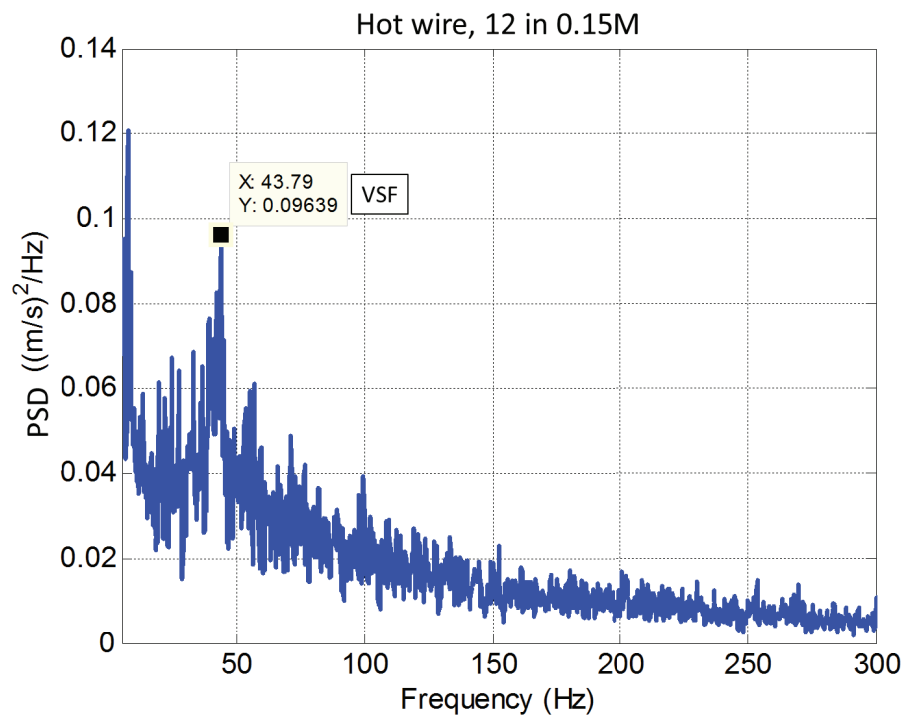


Figure 6.2: HW PSD with the 12 in pod

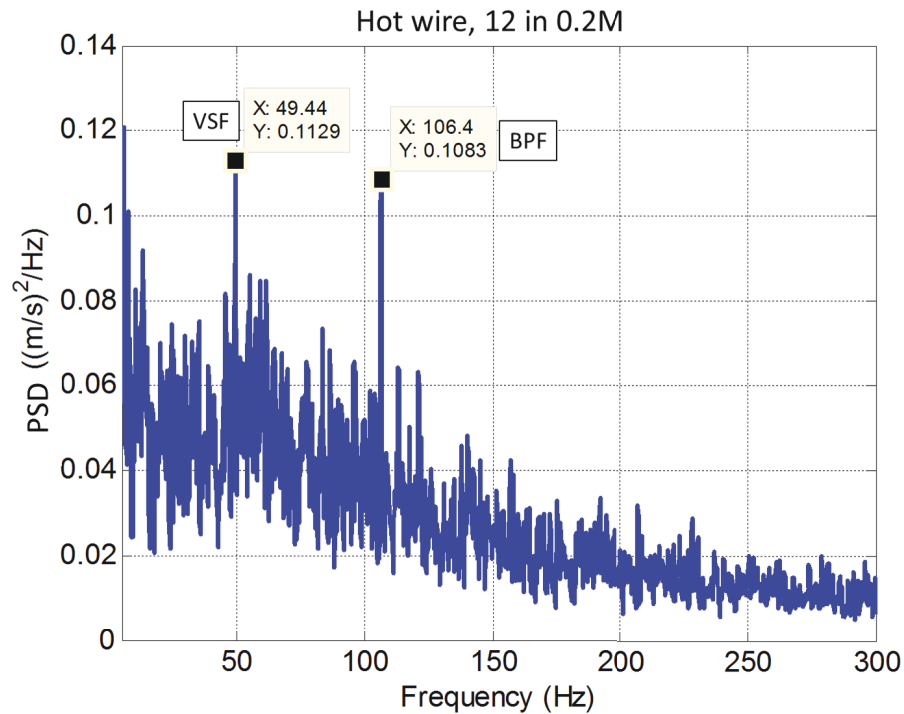


Figure 6.3: HW PSD with the 12 in pod

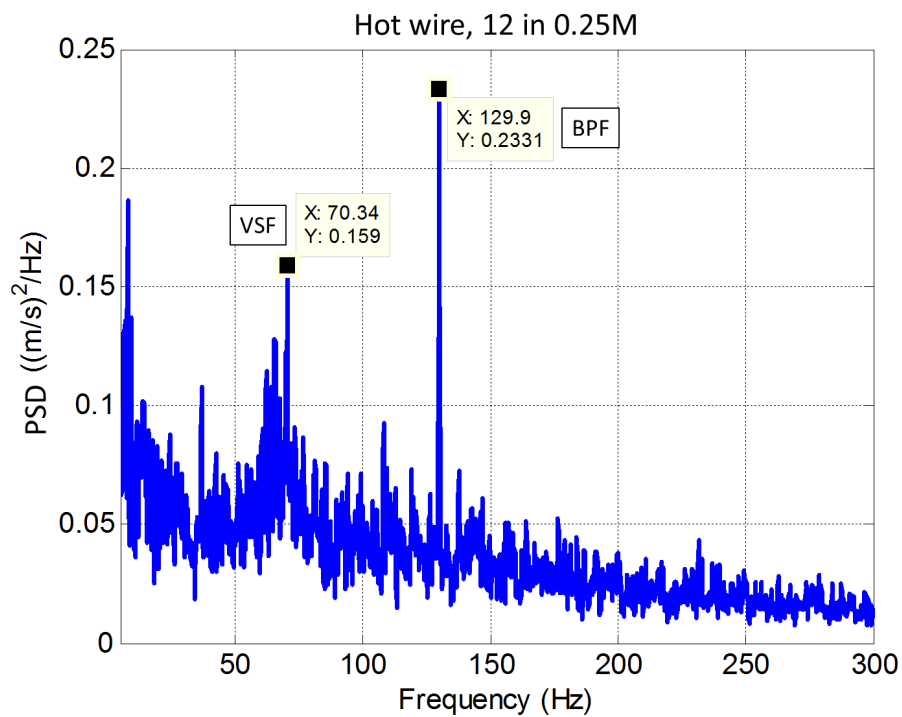


Figure 6.4: HW PSD with the 12 in pod

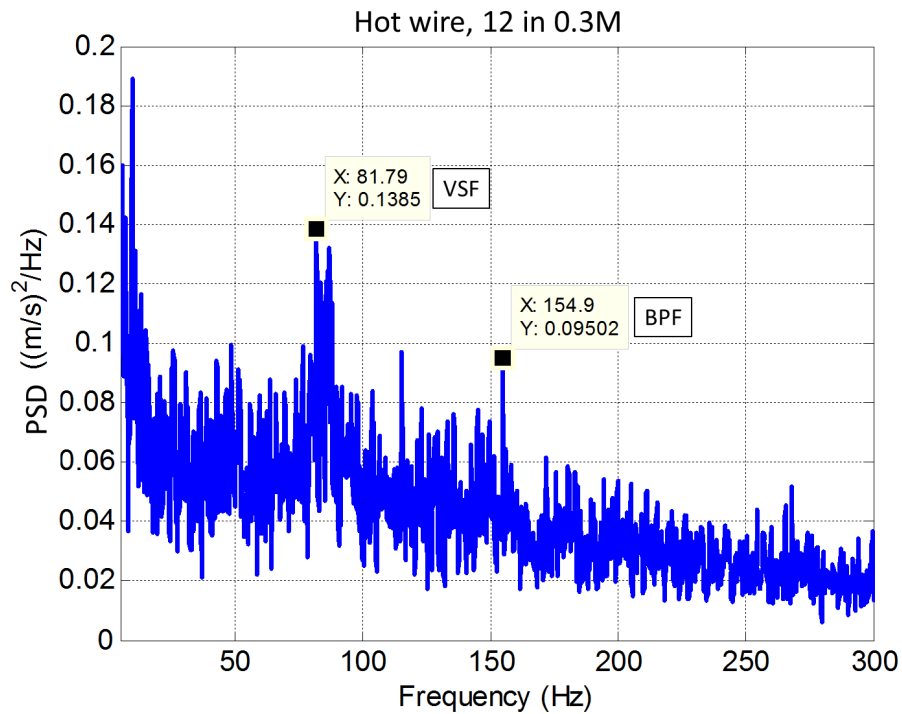


Figure 6.5: HW PSD with the 12 in pod

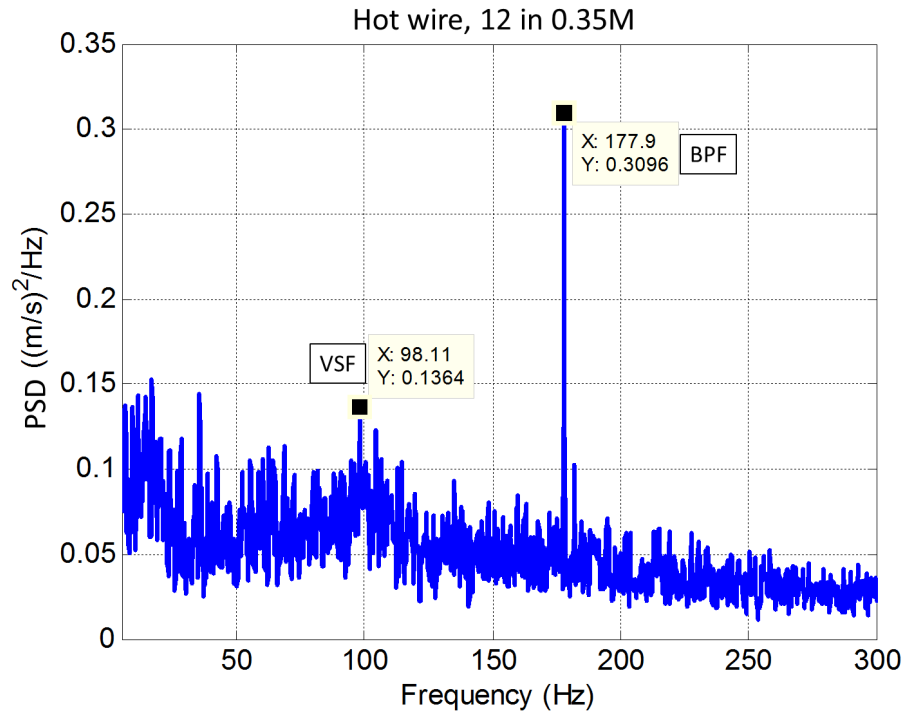


Figure 6.6: HW PSD with the 12 in pod

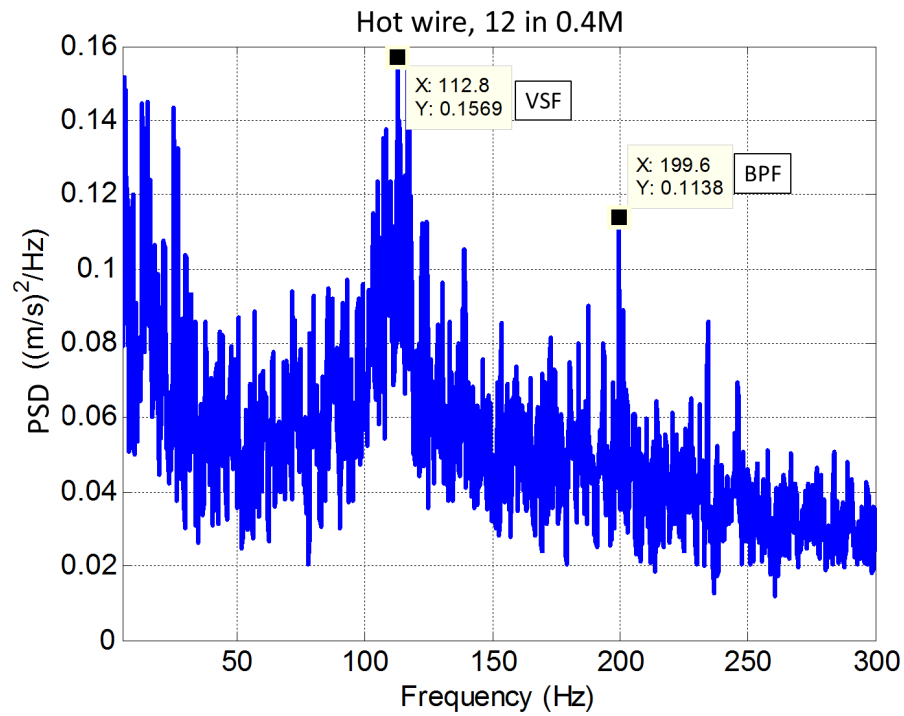


Figure 6.7: HW PSD with the 12 in pod

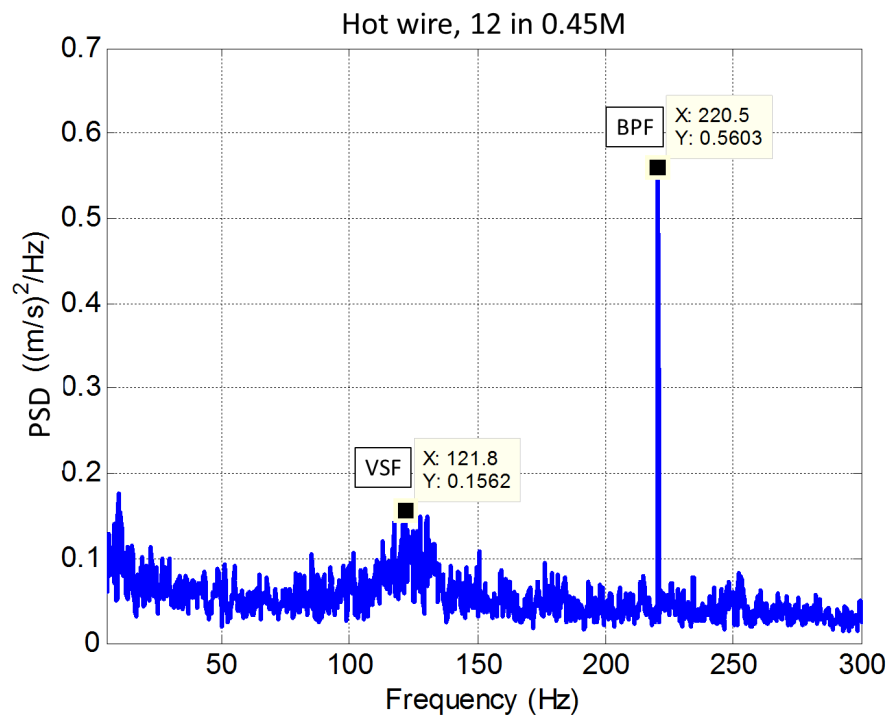


Figure 6.8: HW PSD with the 12 in pod

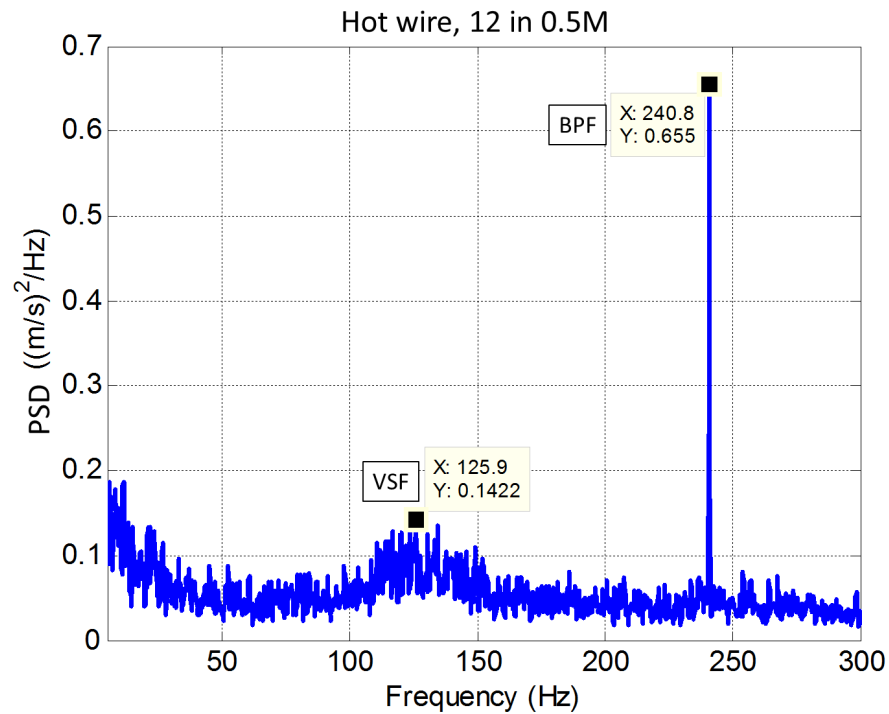


Figure 6.9: HW PSD with the 12 in pod

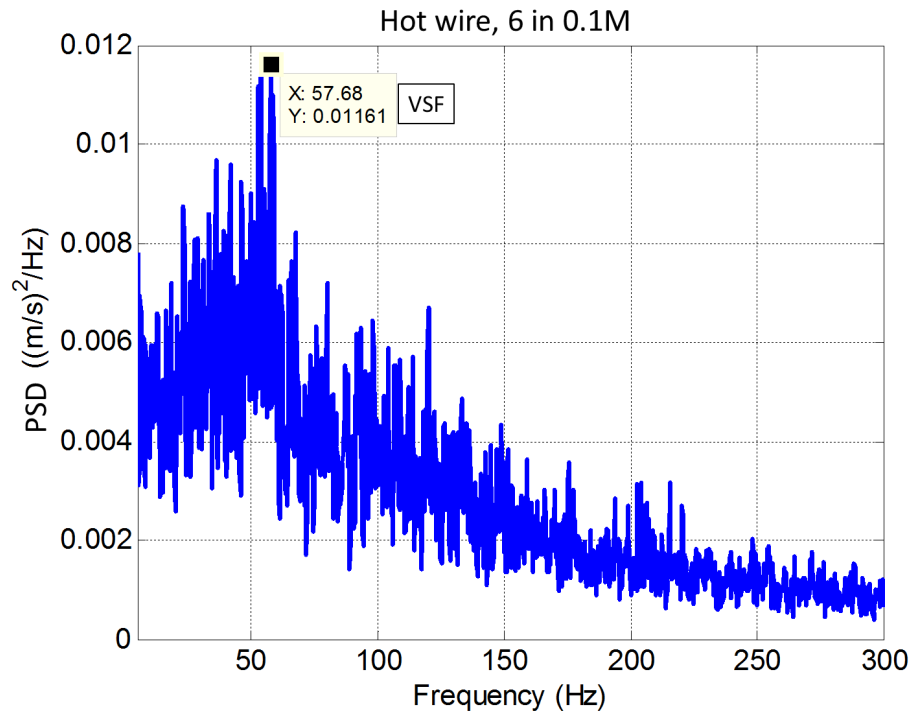


Figure 6.10: HW PSD with the 6 in pod

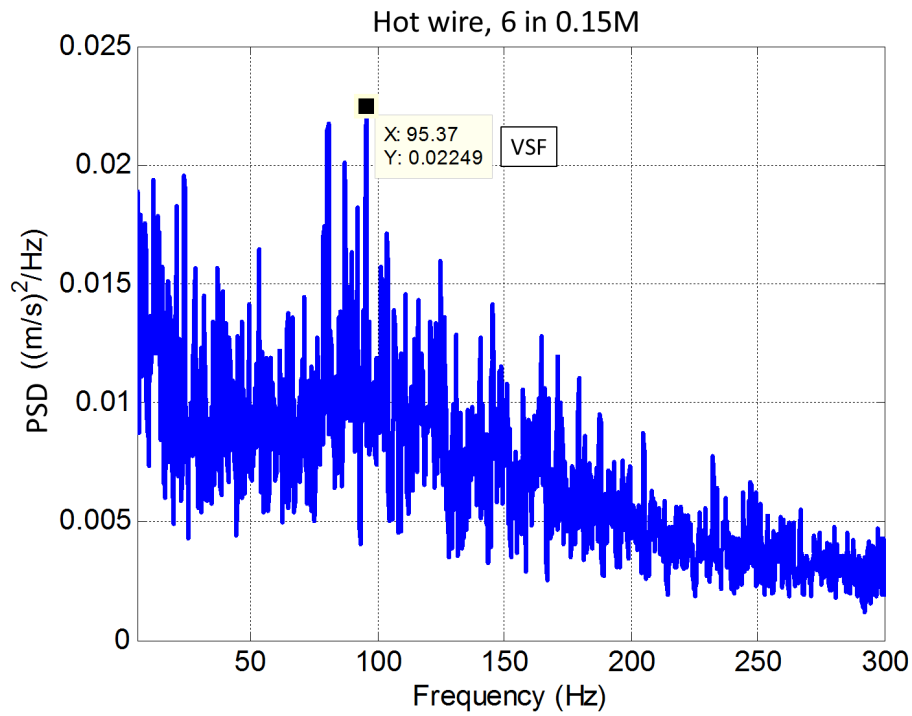


Figure 6.11: HW PSD with the 6 in pod

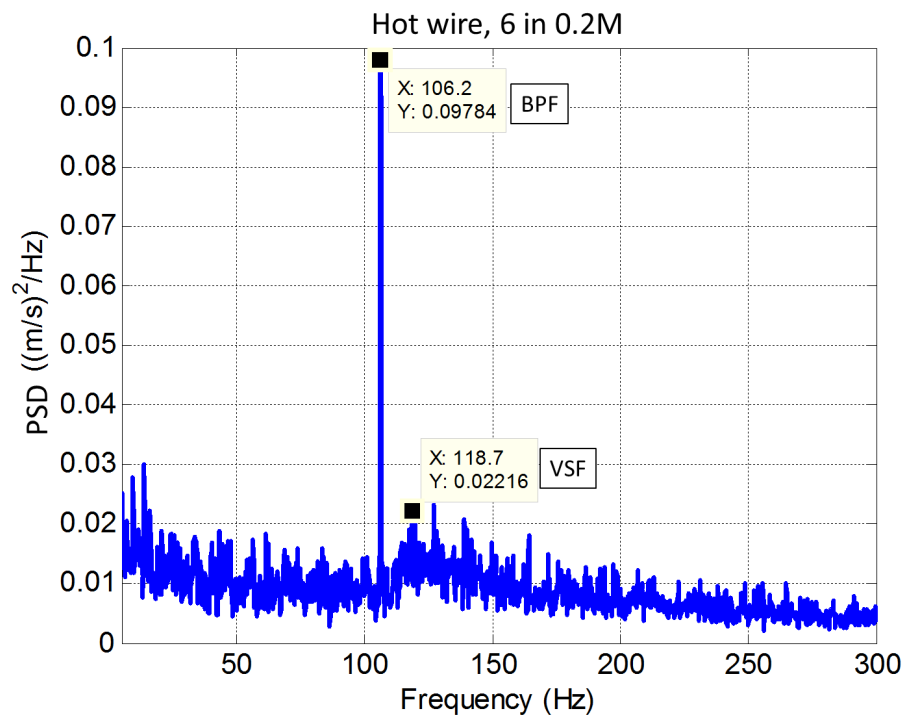


Figure 6.12: HW PSD with the 6 in pod

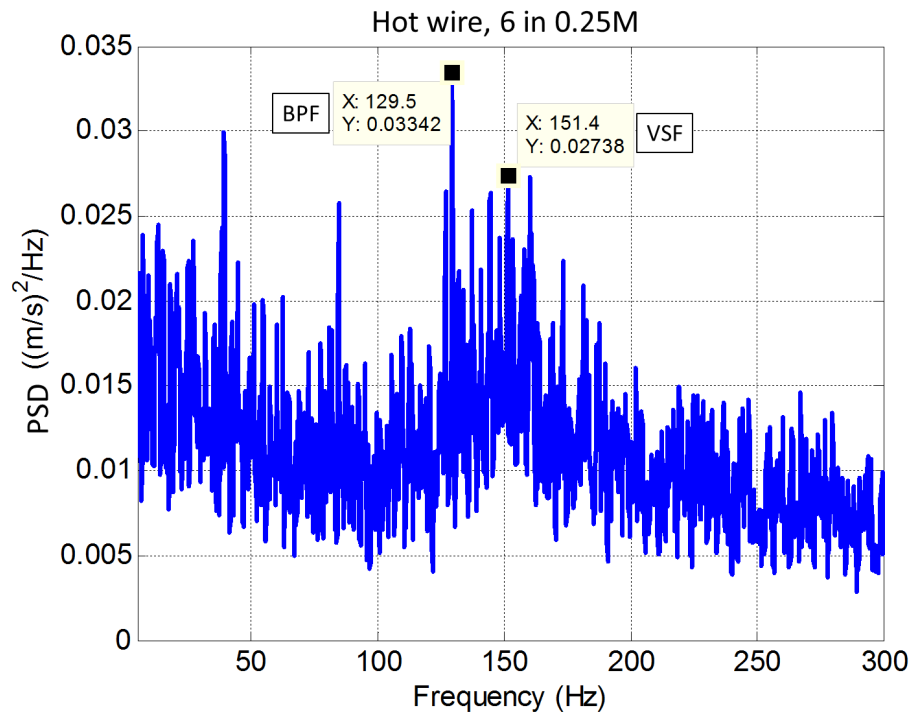


Figure 6.13: HW PSD with the 6 in pod

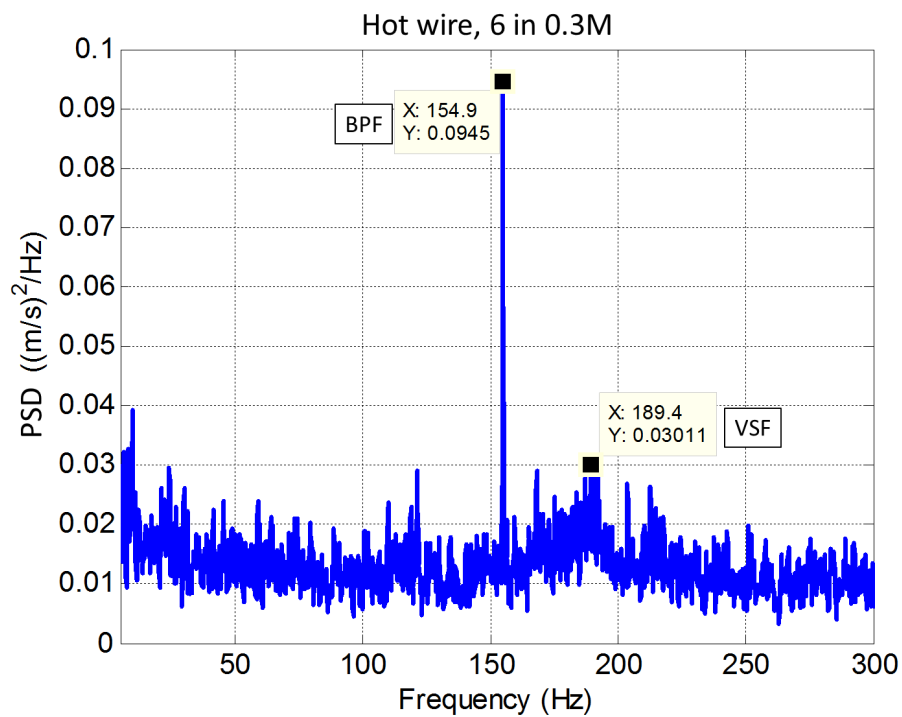


Figure 6.14: HW PSD with the 6 in pod

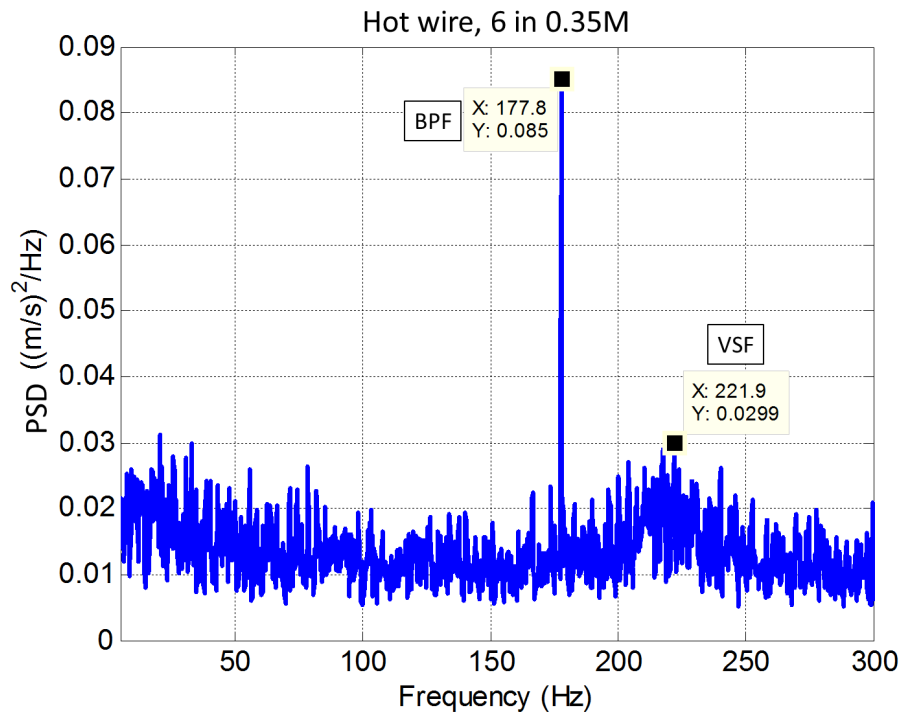


Figure 6.15: HW PSD with the 6 in pod

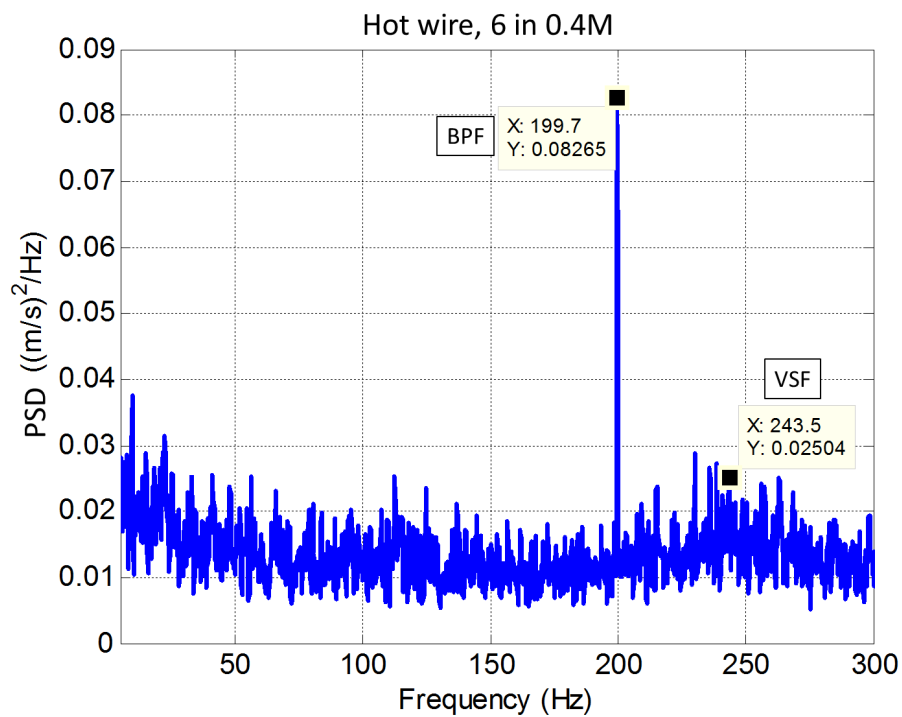


Figure 6.16: HW PSD with the 6 in pod

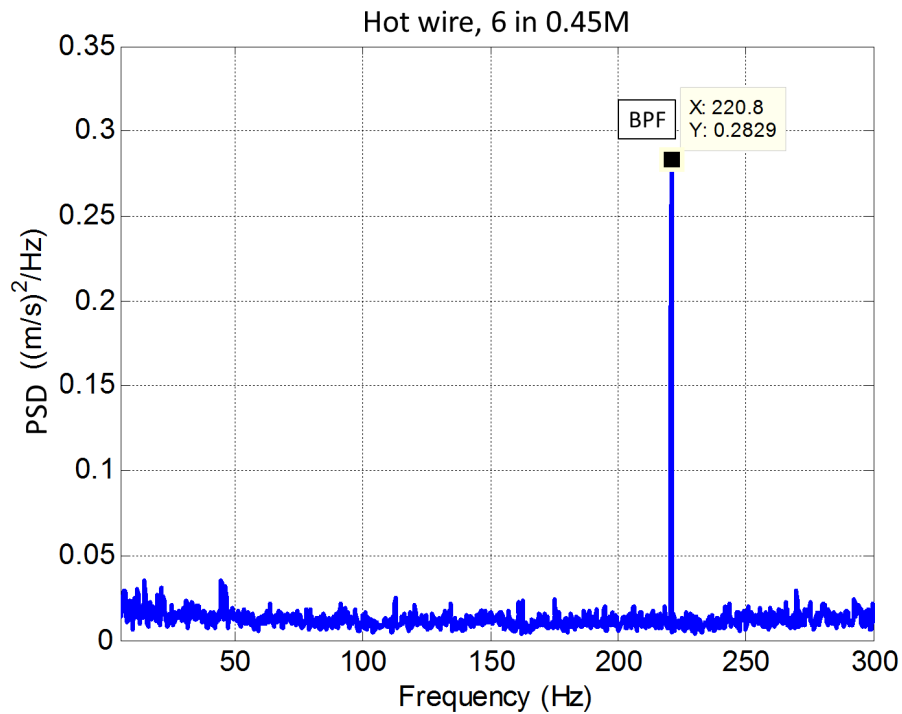


Figure 6.17: HW PSD with the 6 in pod

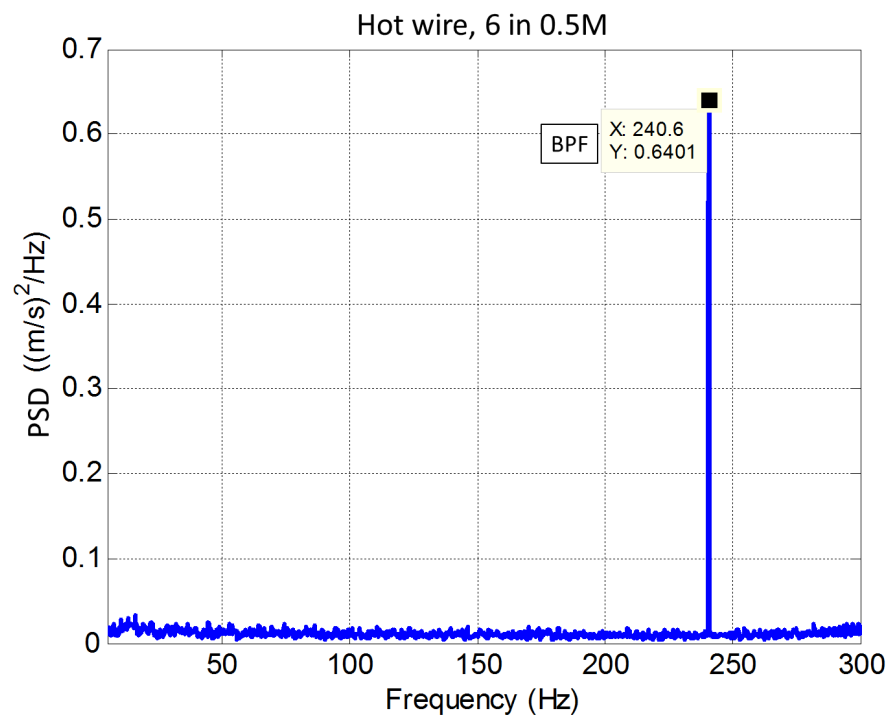


Figure 6.18: HW PSD with the 6 in pod

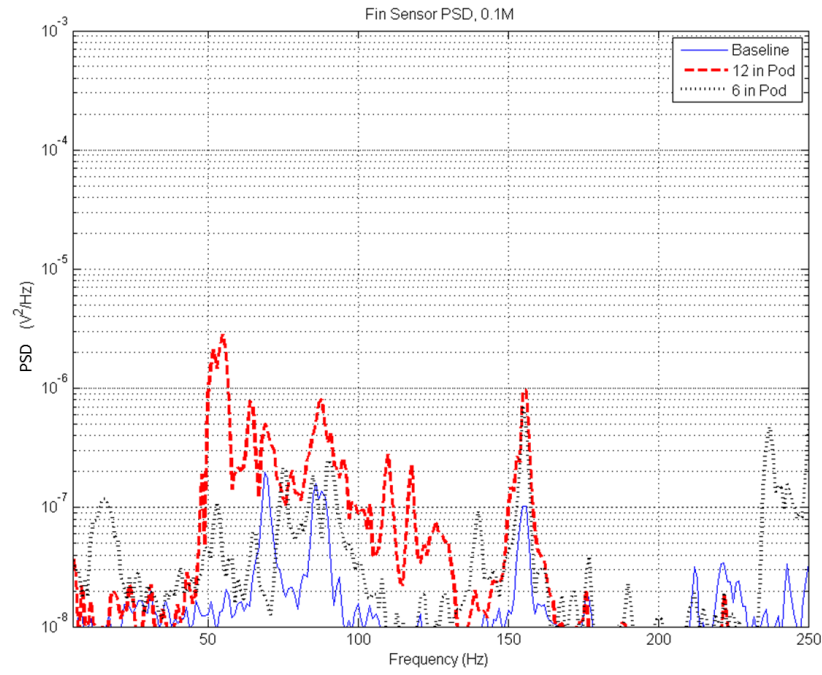


Figure 6.19: Baseline, 12 in pod, and 6 in pod uncontrolled PSD comparisons at 0.1M

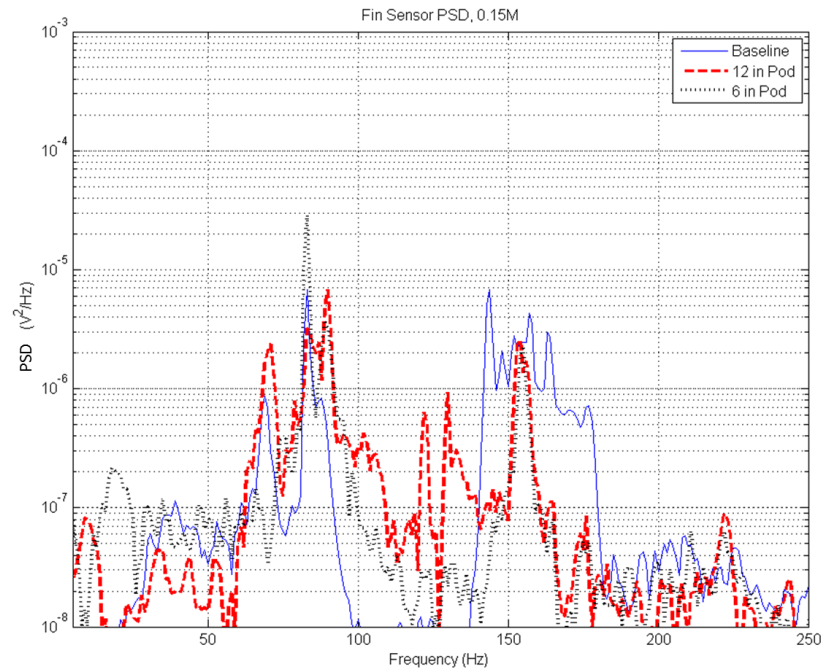


Figure 6.20: Baseline, 12 in pod, and 6 in pod uncontrolled PSD comparisons at 0.15M

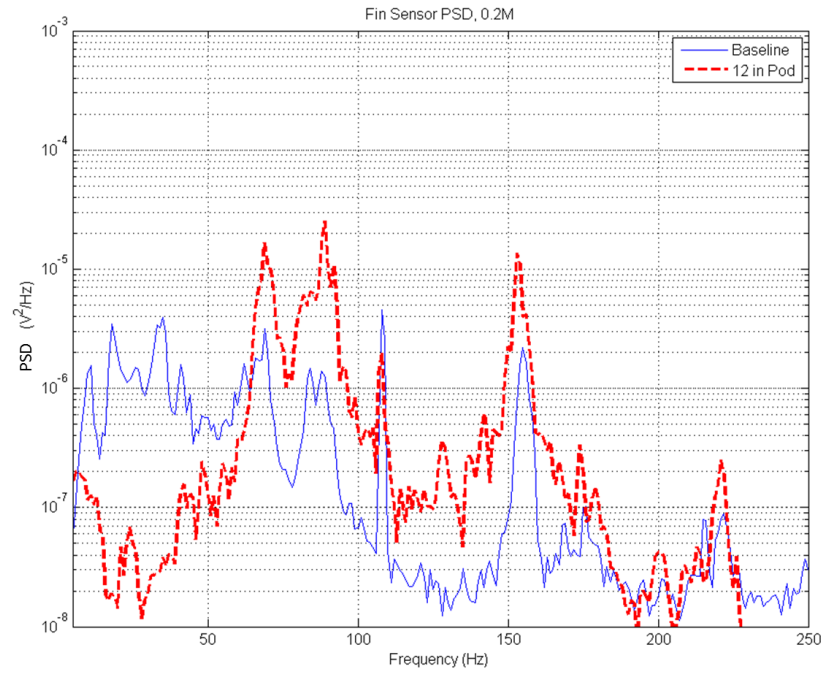


Figure 6.21: Baseline, 12 in pod, and 6 in pod uncontrolled PSD comparisons at 0.2M

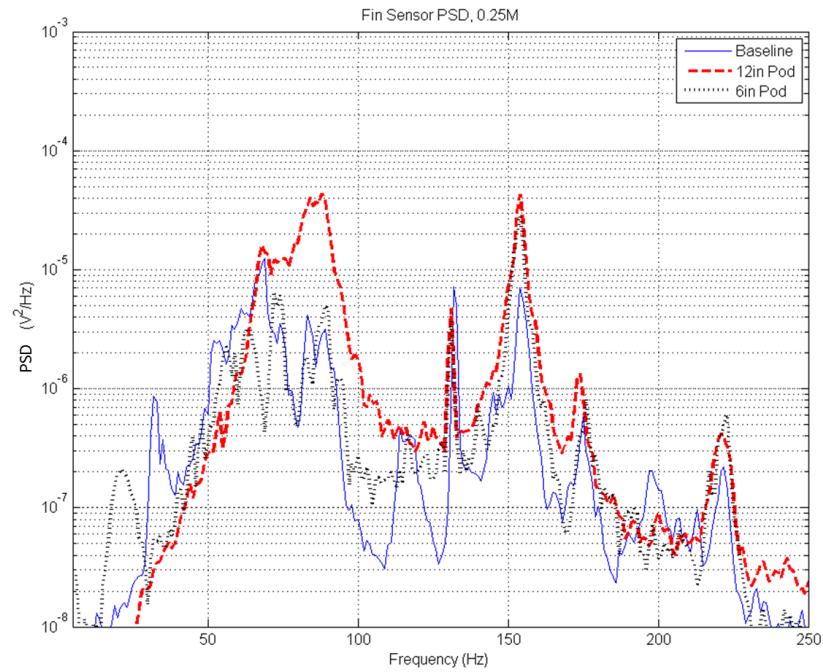


Figure 6.22: Baseline, 12 in pod, and 6 in pod uncontrolled PSD comparisons at 0.25M

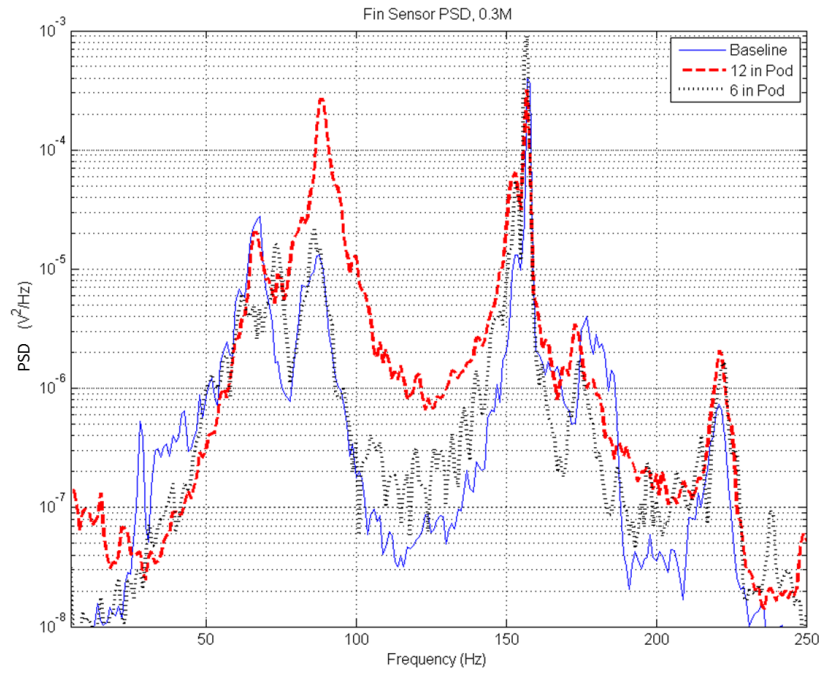


Figure 6.23: Baseline, 12 in pod, and 6 in pod uncontrolled PSD comparisons at 0.3M

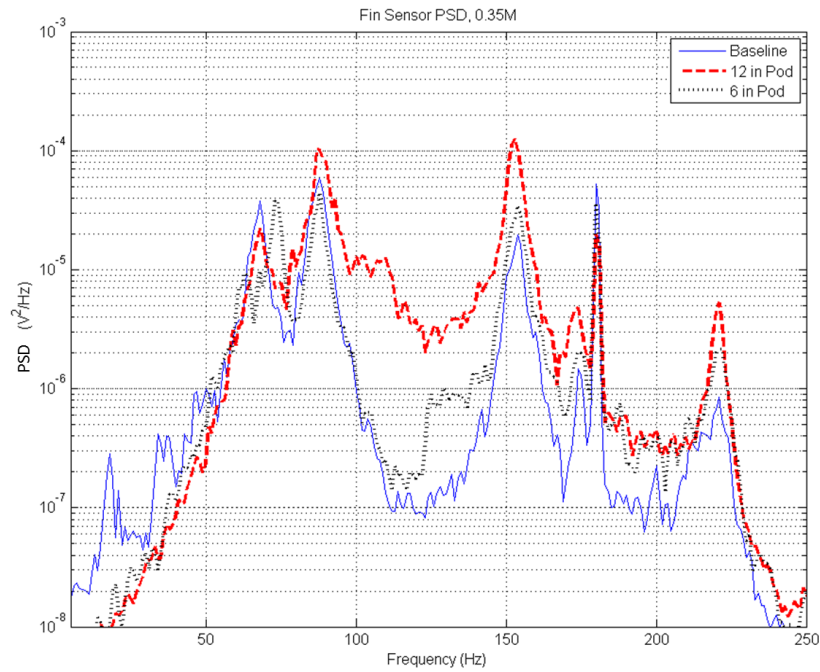


Figure 6.24: Baseline, 12 in pod, and 6 in pod uncontrolled PSD comparisons at 0.35M

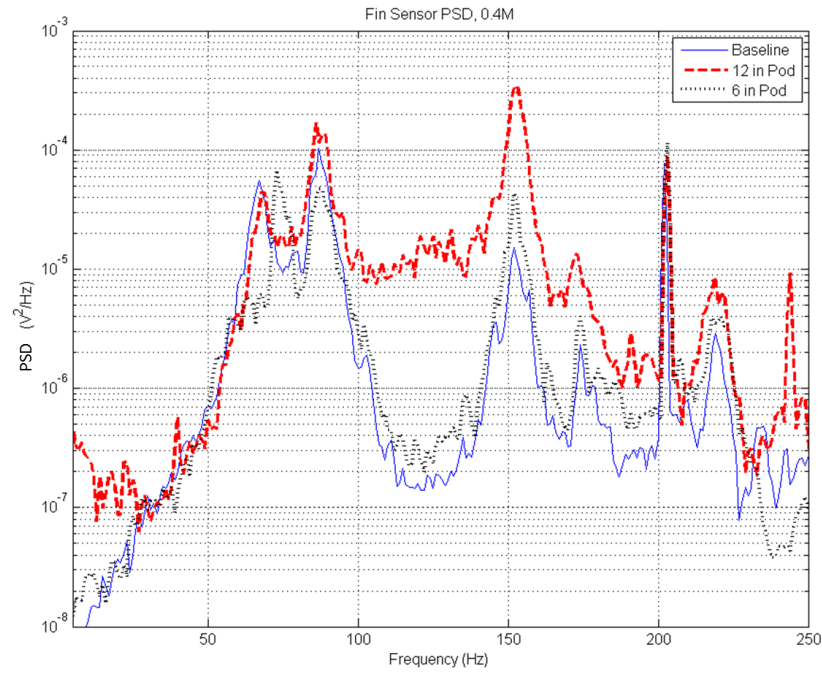


Figure 6.25: Baseline, 12 in pod, and 6 in pod uncontrolled PSD comparisons at 0.4M

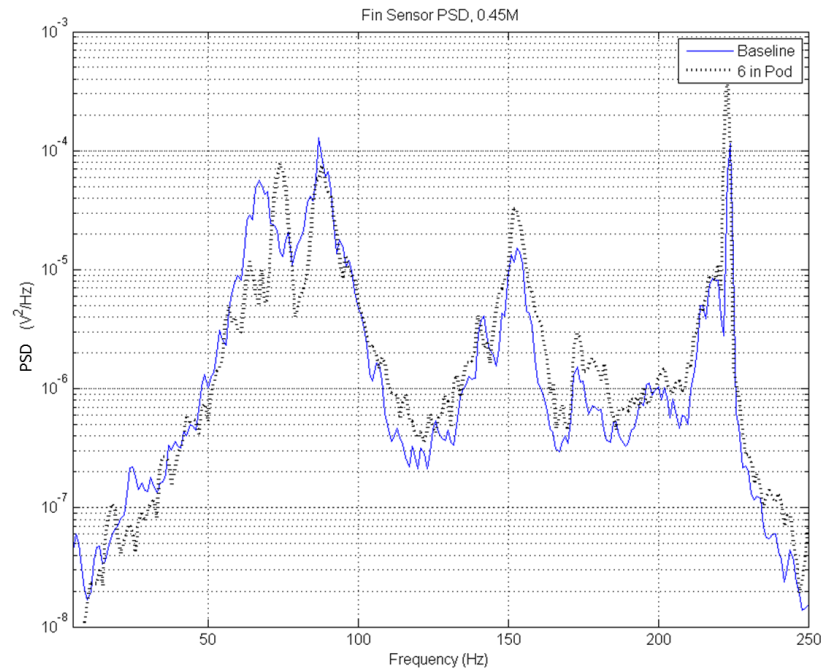


Figure 6.26: Baseline, 12 in pod, and 6 in pod uncontrolled PSD comparisons at 0.45M

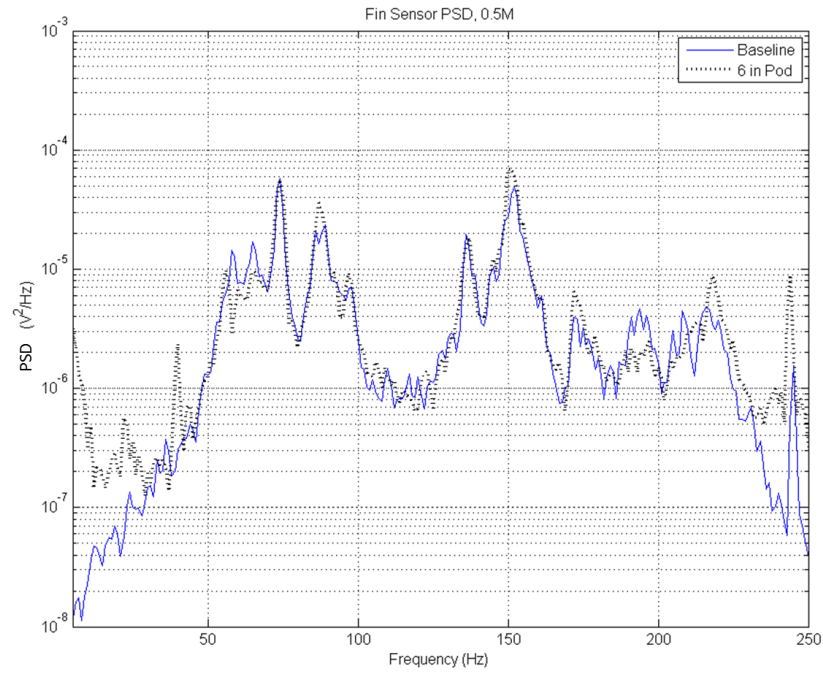


Figure 6.27: Baseline, 12 in pod, and 6 in pod uncontrolled PSD comparisons at 0.5M

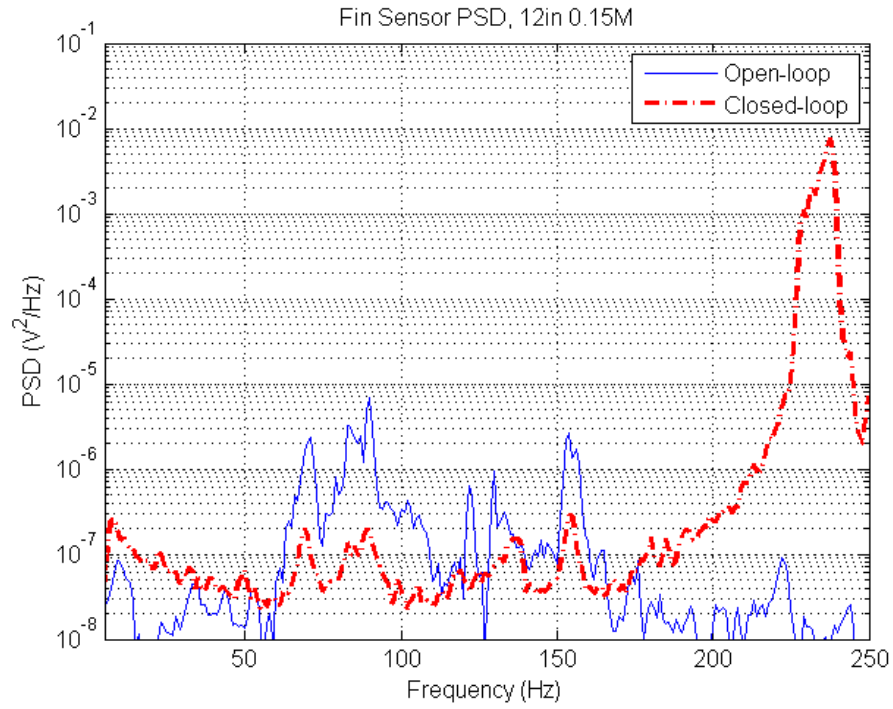


Figure 6.28: Comparison of uncontrolled and controlled PSDs with the 12 in pod at 0.15M

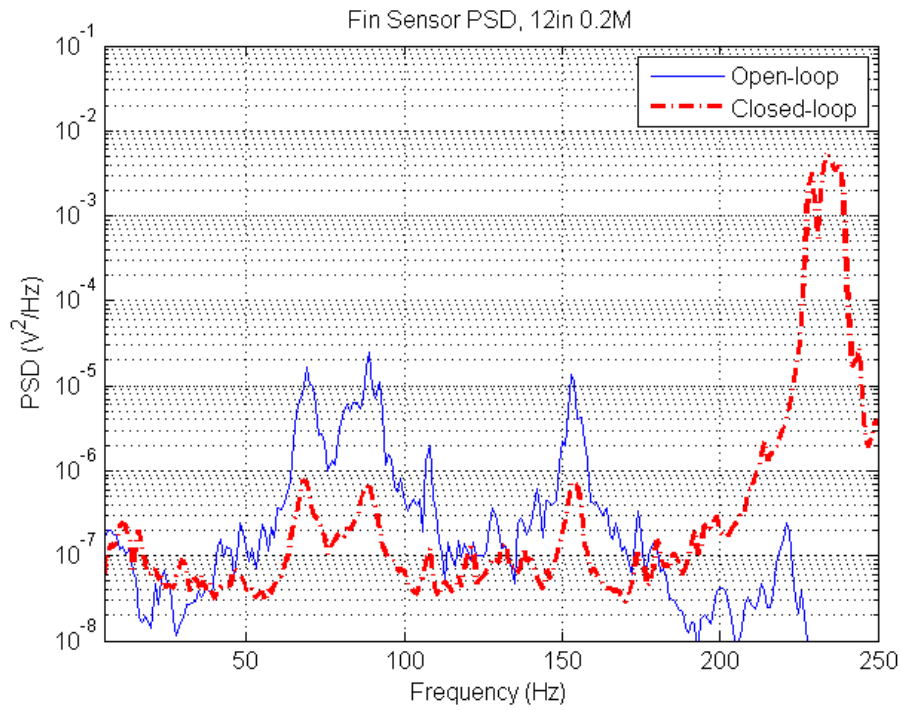


Figure 6.29: Comparison of uncontrolled and controlled PSDs with the 12 in pod at 0.2M

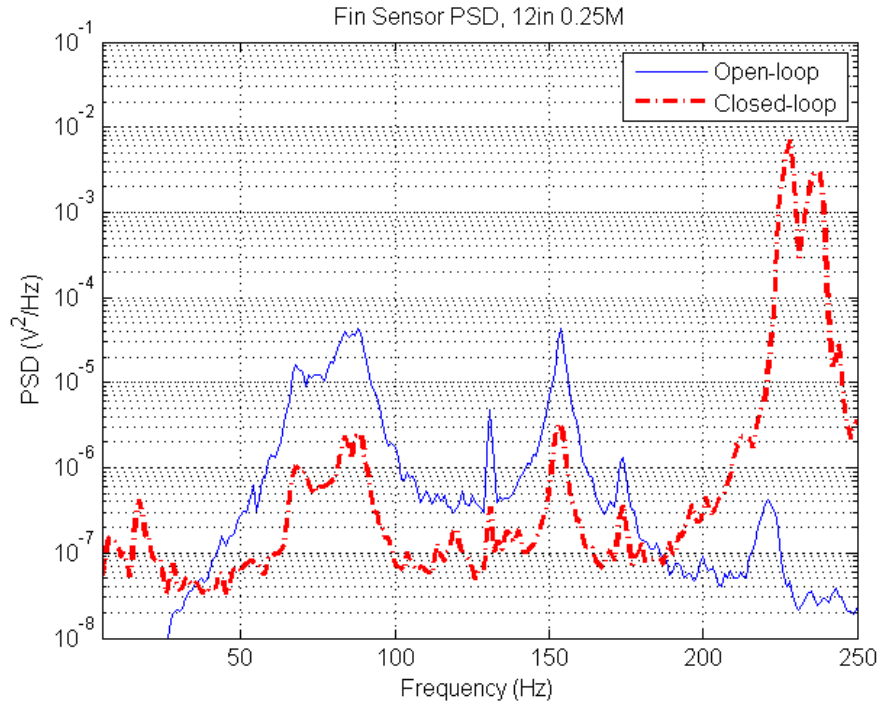


Figure 6.30: Comparison of uncontrolled and controlled PSDs with the 12 in pod at $0.25M$

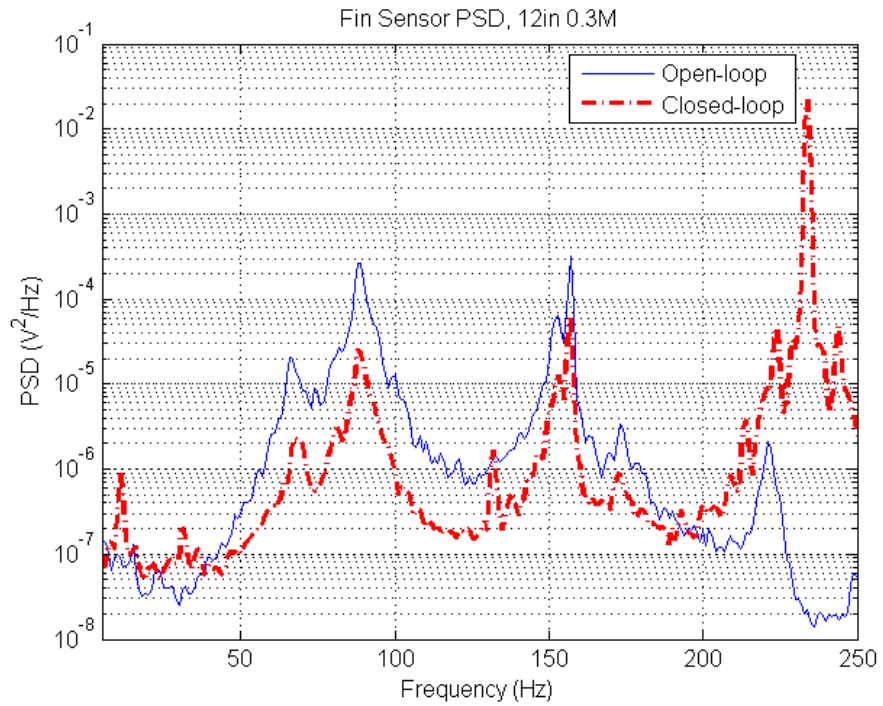


Figure 6.31: Comparison of uncontrolled and controlled PSDs with the 12 in pod at $0.3M$

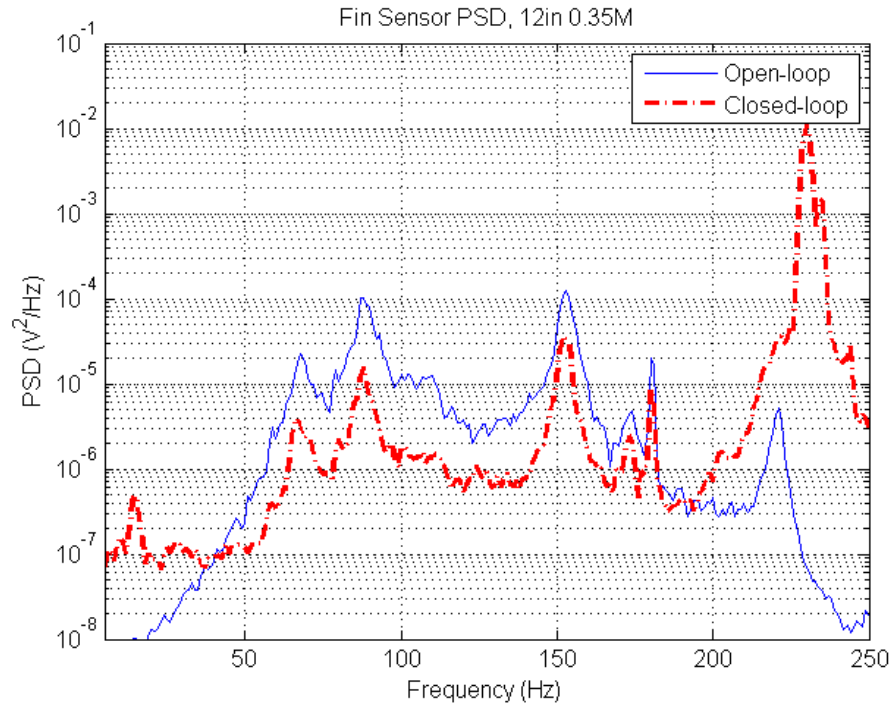


Figure 6.32: Comparison of uncontrolled and controlled PSDs with the 12 in pod at 0.35M

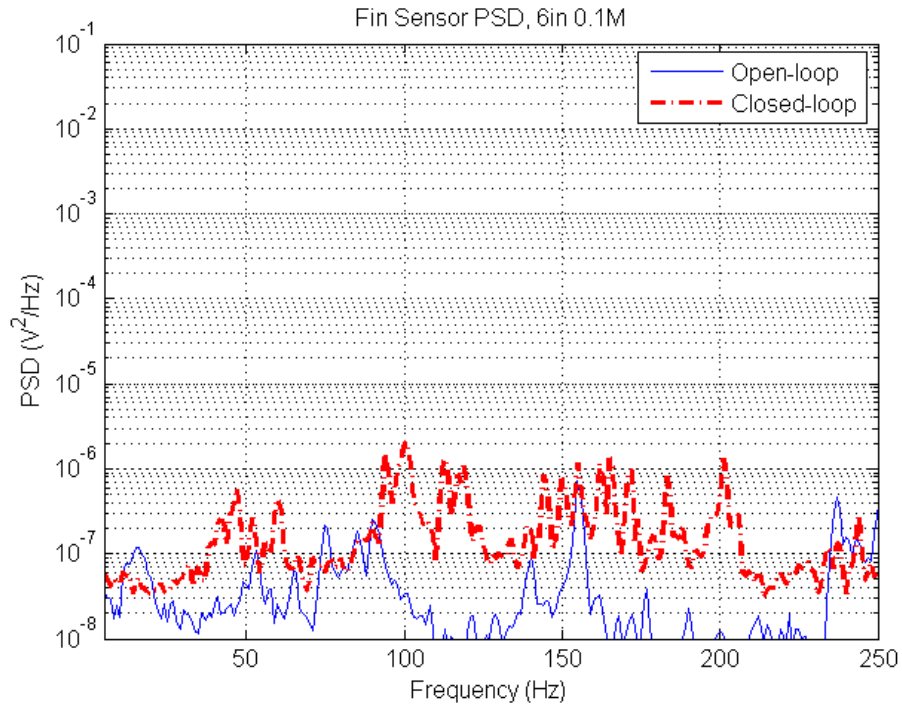


Figure 6.33: Comparison of uncontrolled and controlled PSDs with the 6 in pod at 0.1M

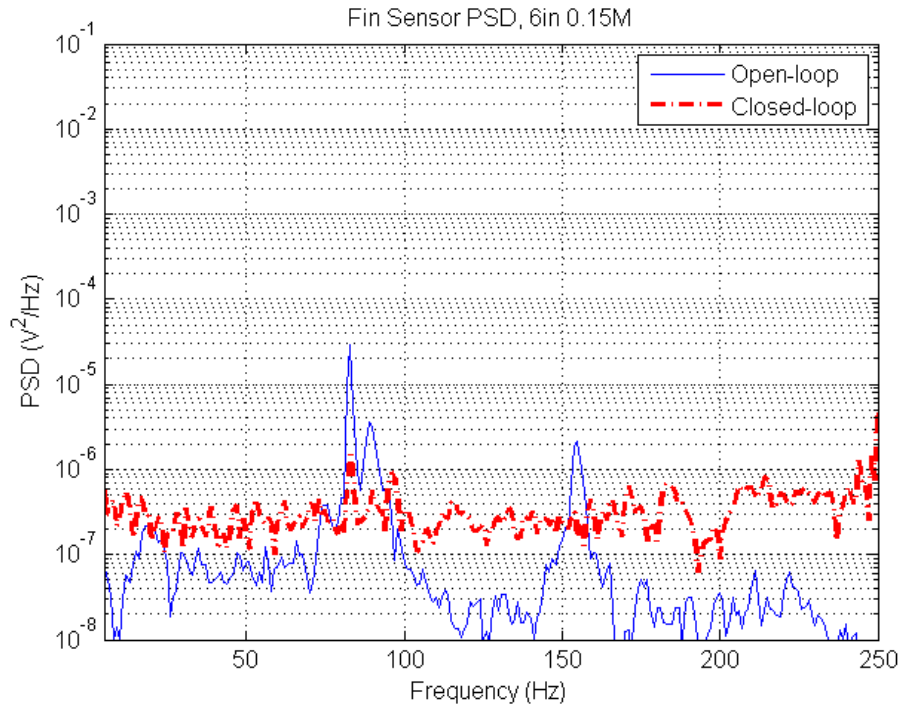


Figure 6.34: Comparison of uncontrolled and controlled PSDs with the 6 in pod at 0.15M

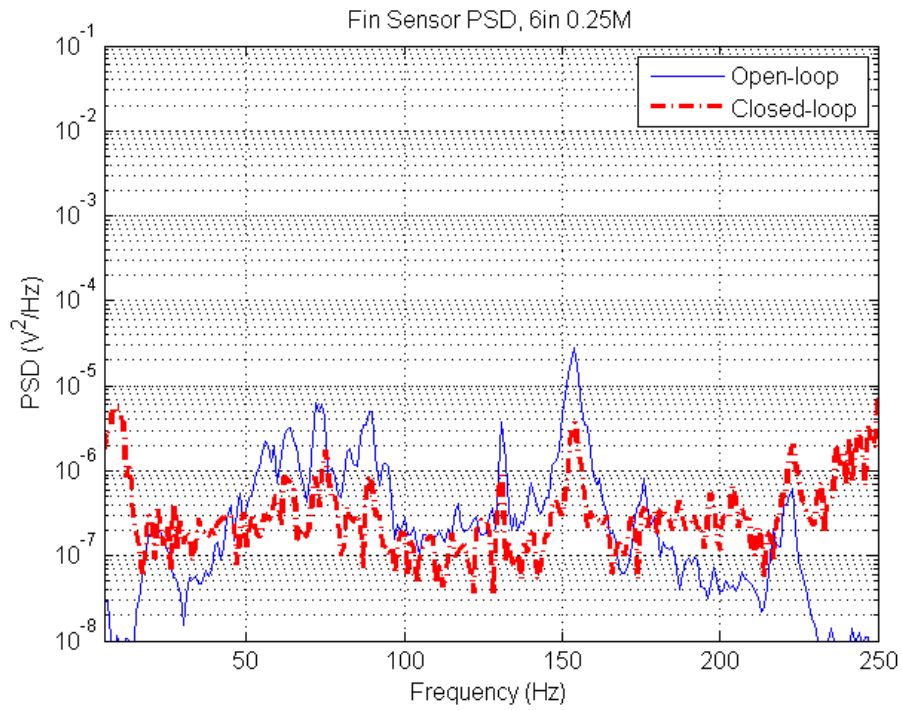


Figure 6.35: Comparison of uncontrolled and controlled PSDs with the 6 in pod at 0.25M

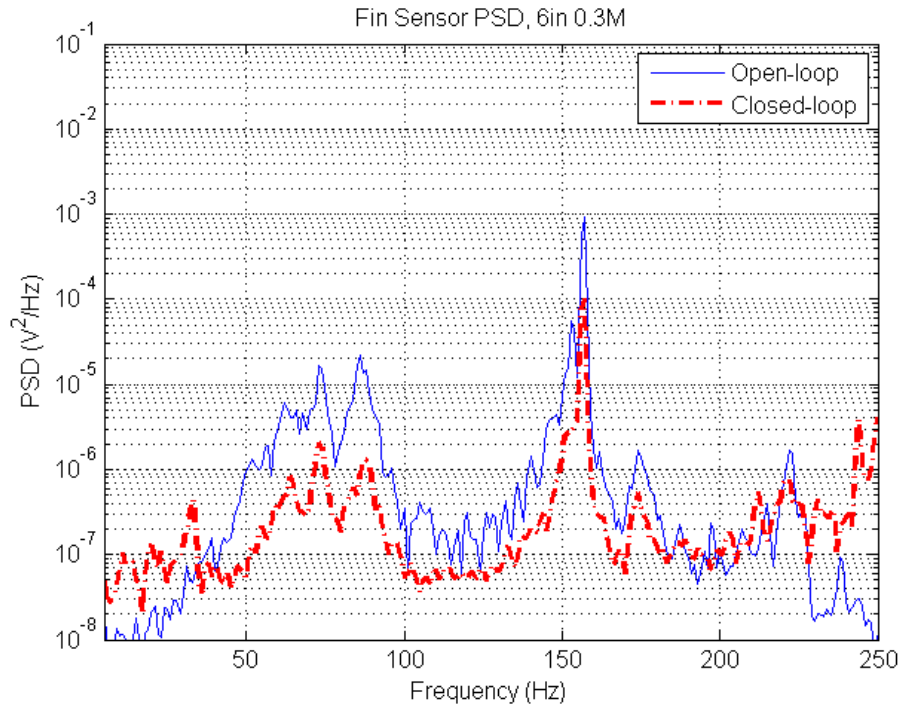


Figure 6.36: Comparison of uncontrolled and controlled PSDs with the 6 in pod at $0.3M$

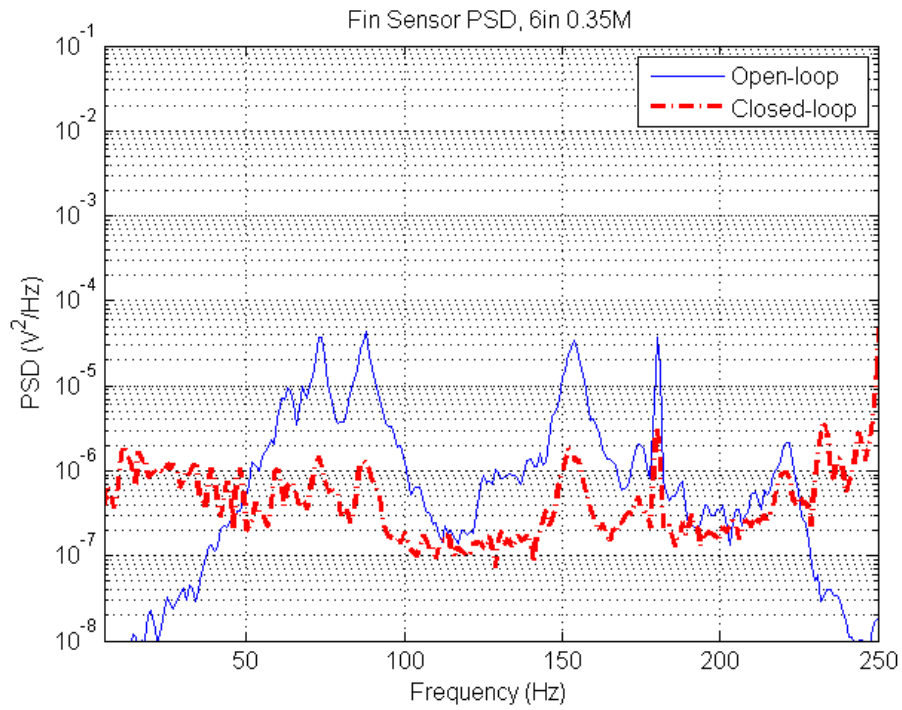


Figure 6.37: Comparison of uncontrolled and controlled PSDs with the 6 in pod at $0.35M$

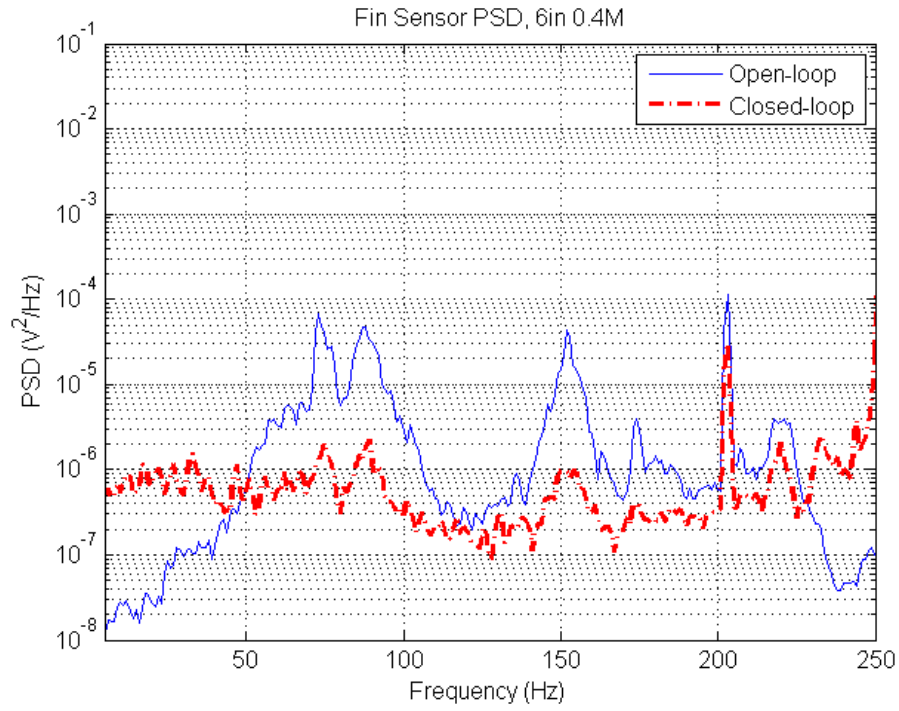


Figure 6.38: Comparison of uncontrolled and controlled PSDs with the 6 in pod at 0.4M

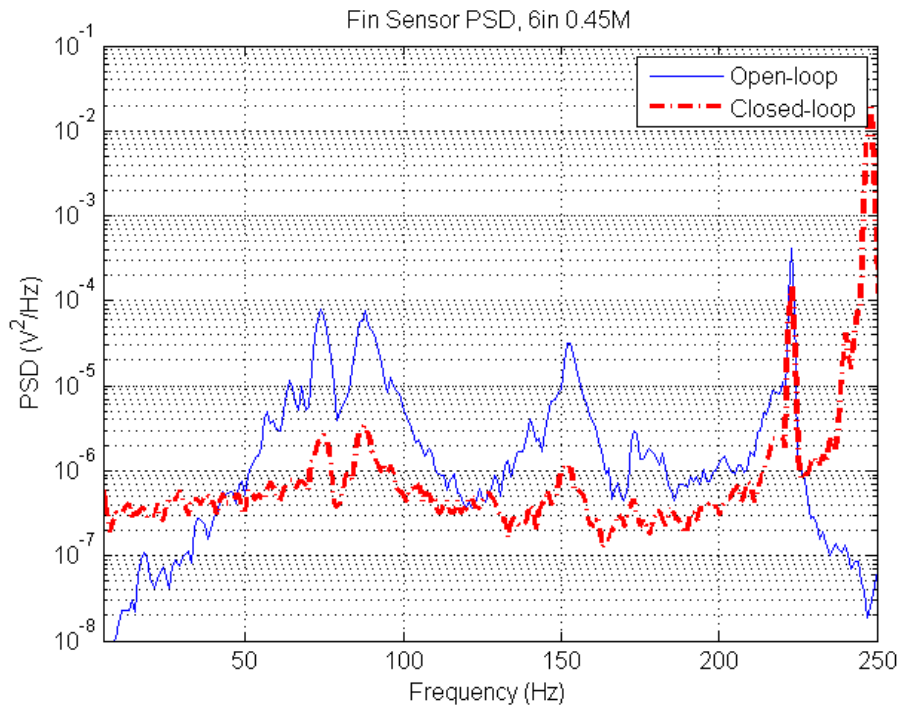


Figure 6.39: Comparison of uncontrolled and controlled PSDs with the 6 in pod at 0.45M

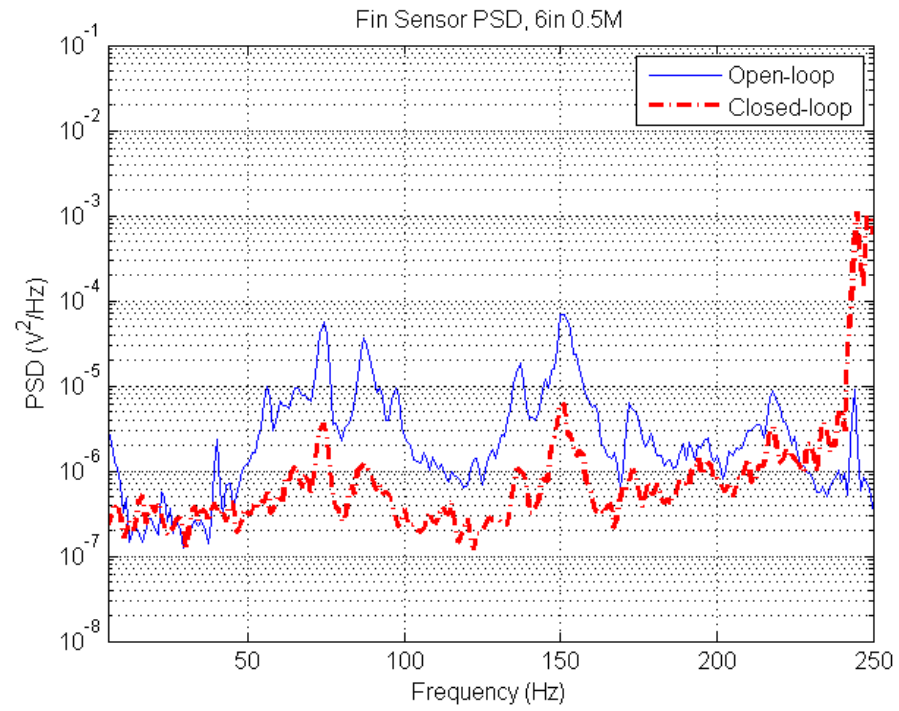


Figure 6.40: Comparison of uncontrolled and controlled PSDs with the 6 in pod at 0.5M

Bibliography

- [1] National Aeronautics and Space Administration. “F/A-18 High Alpha Research Vehicle”. <http://www.nasa.gov/centers/dryden/multimedia/imagegallery/F-18HARV/index.html#lowerAccordion-set1-slide10>, April 1989. 18 February 2014.
- [2] John D. Anderson. *Fundamentals of Aerodynamics*. McGraw-Hill, New York, 5th edition, 2011.
- [3] ApexAero. “F-18 lex vortex”. <http://www.rcgroups.com/forums/attachment.php?attachmentid=3649699>, December 2010. 18 February 2014.
- [4] Joseph S. Browning. “F-16 Ventral Fin Buffet Alleviation Using Piezoelectric Actuators”. Master’s thesis, School of Engineering and Management, Air Force Institute of Technology (AU), Wright-Patterson AFB OH, 2009.
- [5] T. K. Caughey and C. J. Goh. “On the Stability Problem Caused by Finite Actuator Dynamics in the Control of Large Space Structures”. *International Journal of Control*, 41(3):787–802, 1985.
- [6] Richard G. Cobb. Lecture Notes, MECH 719, Vibration Damping and Control. School of Engineering and Management, Air Force Institute of Technology, Wright-Patterson AFB OH, September 2012.
- [7] National Research Council. *Aging of U.S. Air Force Aircraft*. Number NMAB-488-2. National Academy Press, Washington, DC, 1997.
- [8] J. L. Fanson and T. K. Caughey. “Positive Possition Feedback Control for Large Space Structures”. *AIAA Journal*, 28(4):717–724, 1990.
- [9] Federation of American Scientists, Military Analysis Network. “LANTIRN”. <https://www.fas.org/man/dod-101/sys/smart/lantirn.htm>, April 2000. 18 February 2014.
- [10] Stefan Fenik and Ladislav Starek. “Optimal PPF Controller For Multimodal Vibration Suppression”. *Engineering Mechanics*, 15(3):153–173, 2008.
- [11] United States Air Force. “Countering MiGs: Air-to-Air Combat over North Vietnam”. <http://www.nationalmuseum.af.mil/factsheets/factsheet.asp?id=18112>, March 2011.
- [12] Sathyanaraya Hanagud. “F-15 Tail Buffet Alleviation: A Smart Structure Approach”. Technical report, Georgia Institute of Technology, Atlanta, GA, 1998.
- [13] Thomas Hegewald. “Vibration Suppression Using Smart Materials in the Presence of Temperature Changes”. Master’s thesis, Virginia Polytechnic Institute and State University, Blacksburg VA, 2000.

- [14] Michael H. Love and Antonio P. De La Garza III. “The Impact of Unsteady Aerodynamics on the Loading of Flight Vehicles”. Technical report, Lockheed Martin Aeronautics Company, 2005.
- [15] S. Nima Mahmoodi, Mehdi Ahmandian, and Daniel J. Inman. “Adaptive Modified Positive Position Feedback for Active Vibration Control of Structures”. *Journal of Intelligent Material Systems and Structures*, 21(6):571–580, 2010.
- [16] J. Marra, P.J.P Goncalves, and L.C.S Goes. “A Multichannel Active-Adaptive Vibration Control System applied to an Aeronautical Structure”. Technical report, 2010.
- [17] Shawn D. Morgenstern. “Alleviation of Buffet-Induced Vibration Using Piezoelectric Actuators”. Master’s thesis, School of Engineering and Management, Air Force Institute of Technology (AU), Wright-Patterson AFB OH, 2006.
- [18] Shawn D. Morgenstern, Heather C. Giebner, Dick Wong, Aaron A. Atucker, and Aniello Violetti. *Limited Characterization of Dual Bimorph Synthetic Jet Actuators: Aeroelastic Load Control-Phase 1: Project HAVE PUFF*. Air Force Flight Test Center, Edwards AFB, CA, 2005.
- [19] Robert W. Moses. “Active Vertical Tail Buffeting Alleviation on an F/A-18 Model in a Wind Tunnel”. Technical report, Aeroelasticity Branch, NASA Langley Research Center, Hampton, VA, 1999.
- [20] Nhan Nguyen, Kalmanje Krishnakumar, John Kaneshige, and Pascal Nespeca. “Dynamics and Adaptive Control for Stability Recovery of Damaged Asymmetric Aircraft”. Technical report, NASA Ames Research Center, Moffett Field CA, 2006.
- [21] F-16 System Program Office. “Closure Package to Waiver 6W0034 Ventral Fin Service Life Deficiency”. Technical report, USAF, 1992.
- [22] Tomoyuki D. Ono. “Application of Multi-Input Multi-Output Feedback Control for F-16 Ventral Fin Buffet Alleviation Using Piezoelectric Actuators”. Master’s thesis, School of Engineering and Management, Air Force Institute of Technology (AU), Wright-Patterson AFB OH, 2012.
- [23] Pacific Coast Air Museum. “F-16N Viper”. <http://pacificcoastairmuseum.org/aircraft/F16NViper.asp>, (n.d). 18 February 2014.
- [24] Tina Reynolds. *Subsonic Aerodynamic Research Laboratory (SARL) Centerline Turbulence Examination*. Air Force Research Laboratory, Wright-Patterson AFB, OH, 2012.
- [25] Matthew Roffe. “Pulling G’s”. <http://www.dphotographer.co.uk/users/221/thm1024/f16g.jpg>, (n.d.). 18 February 2014.

- [26] E. Sanmiguel-Rojas, A. Sevilla, C. Martinez-Braza, and J.-M. Chomaz. “Global mode analysis of axisymmetric bluff-body wakes: Stabilization by base bleed”. *Physics of Fluids*, 21(11):114102–1–114102–13, 2009.
- [27] A. Sevilla and C. Martinez-Bazan. “Vortex shedding in high Reynolds number axisymmetric bluff-body wakes: Local linear instability and global bleed control”. *Physics of Fluids*, 16(9):3460–3469, 2004.
- [28] Vinod K. Sharma. *Laser Doppler Vibrometer for Efficient Structural Health Monitoring*. PhD thesis, Georgia Institute of Technology, Atlanta, GA, 2008.
- [29] USAF.com. “F-15 Eagle”. <http://www.usaf.com/aircraft/f15.htm>, October 1992. 18 February 2014.
- [30] Ton van den Boom. Lecture Notes, SC4090, Discrete-time systems analysis. Delft Center for Systems and Control, Delft University of Technology, The Netherlands, October 2006.
- [31] Ansgar Weickgenannt and Peter A. Monkewitz. “Control of vortex shedding in an axisymmetric bluff body wake”. *European Journal of Mechanics B/Fluids*, 19:789–812, 2000.

Vita

Captain Jared M. Rupp graduated from Air Academy High School in Colorado Springs, Colorado. He attended the University of Colorado, Colorado Springs while completing a four year Reserve Officer Training Corps program at the University of Colorado, Boulder. After graduating with a Bachelor of Science degree in Mechanical Engineering, he commissioned into the USAF as a Second Lieutenant in December 2006.

Captain Rupp was assigned to the 40th Flight Test Squadron, Eglin AFB, FL, as a UH-1 Flight Test Engineer (FTE), where he conducted numerous experimental test and training missions in UH-1N, F-16D, and F-15D/E aircraft. He was then assigned as an FTE to the 28th Test & Evaluation Squadron to conduct operational test on F-16 operational flight programs.

In early 2011, he was selected for the combined Air Force Institute of Technology (AFIT)/Test Pilot School (TPS) program, attending AFIT to work on a Master of Science degree in Aeronautical Engineering. After 15 months, he moved to CA and attended the yearlong USAF TPS as part of Class 13A and graduated with a Master of Science degree in Flight Test Engineering. Following completion of his AFIT degree, Captain Rupp will be assigned to the 413th Flight Test Squadron, Hurlburt Field, FL, as a CV-22 FTE.

| REPORT DOCUMENTATION PAGE | | | | | <i>Form Approved</i> OMB No. 0704-0188 | |
|---|-------------|--|---|--|--|--|
| The public reporting burden for this collection of information is estimated to average 1 hour per response, including the time for reviewing instructions, searching existing data sources, gathering and maintaining the data needed, and completing and reviewing the collection of information. Send comments regarding this burden estimate or any other aspect of this collection of information, including suggestions for reducing this burden to Department of Defense, Washington Headquarters Services, Directorate for Information Operations and Reports (0704-0188), 1215 Jefferson Davis Highway, Suite 1204, Arlington, VA 22202-4302. Respondents should be aware that notwithstanding any other provision of law, no person shall be subject to any penalty for failing to comply with a collection of information if it does not display a currently valid OMB control number. PLEASE DO NOT RETURN YOUR FORM TO THE ABOVE ADDRESS. | | | | | | |
| 1. REPORT DATE (DD-MM-YYYY) 27-03-2014 | | 2. REPORT TYPE Master's Thesis | | 3. DATES COVERED (From — To) Oct 2011–Mar 2014 | | |
| 4. TITLE AND SUBTITLE Adaptive Positive Position Feedback Control of Flexible Aircraft Structures Using Piezoelectric Actuators | | | | 5a. CONTRACT NUMBER | | |
| | | | | 5b. GRANT NUMBER | | |
| | | | | 5c. PROGRAM ELEMENT NUMBER | | |
| 6. AUTHOR(S) Rupp, Jared M., Captain, USAF | | | | 5d. PROJECT NUMBER | | |
| | | | | 5e. TASK NUMBER | | |
| | | | | 5f. WORK UNIT NUMBER | | |
| 7. PERFORMING ORGANIZATION NAME(S) AND ADDRESS(ES) Air Force Institute of Technology Graduate School of Engineering and Management (AFIT/EN) 2950 Hobson Way WPAFB, OH 45433-7765 | | | | 8. PERFORMING ORGANIZATION REPORT NUMBER AFIT-ENY-14-M-42 | | |
| 9. SPONSORING / MONITORING AGENCY NAME(S) AND ADDRESS(ES) Glenn Ballentine (661) 277-3000 USAF Test Pilot School 220 South Wolfe Av Edwards AFB, CA 93524 | | | | 10. SPONSOR/MONITOR'S ACRONYM(S) USAF TPS | | |
| | | | | 11. SPONSOR/MONITOR'S REPORT NUMBER(S) | | |
| 12. DISTRIBUTION / AVAILABILITY STATEMENT DISTRIBUTION STATEMENT A: APPROVED FOR PUBLIC RELEASE; DISTRIBUTION UNLIMITED | | | | | | |
| 13. SUPPLEMENTARY NOTES This material is declared a work of the U.S. Government and is not subject to copyright protection in the United States. | | | | | | |
| 14. ABSTRACT Buffet Adaptively Managed Fin (BAMF) focused on vibrations due to the interaction of aerodynamic forces with aircraft structure. Past failures of F-16 ventral fins due to vibrations provided grounds for control research. The fin used had piezoelectric patches as collocated sensors/actuators. A custom amplifier and transformer were restructured into a system that could safely and reliably run, and adaptive software was created to address issues of system plant changes. Generating a PSD from the fin sensors, the highest peaks were assumed to represent the low damped vibration modes. A PPF controller for each mode was designed and control signals were sent to the fin actuators. Limited data were collected in a wind tunnel behind a custom system that caused buffet by varying vortex strength/shedding frequencies from pods upstream of the fin. While minimal testing was accomplished to optimize gains, the system showed significant PSD peak reductions for the first three modes of the fin up to -14.9, -15.3, and -16.4 dB, respectively. The system maintained stability and effective control even when both sensor input and controller output were saturated. | | | | | | |
| 15. SUBJECT TERMS adaptive control, positive position feedback control, flexible aircraft structures, piezoelectric vibration control | | | | | | |
| 16. SECURITY CLASSIFICATION OF: | | | 17. LIMITATION OF ABSTRACT UU | | 18. NUMBER OF PAGES 124 | |
| a. REPORT | b. ABSTRACT | c. THIS PAGE | | | | |
| U | U | U | 19a. NAME OF RESPONSIBLE PERSON Dr. Richard G. Cobb, AFIT/ENY | | | |
| | | | | 19b. TELEPHONE NUMBER (include area code) (937) 255-3636 x4559 richard.cobb@afit.edu | | |